WASHINGTON UNIVERSITY IN ST. LOUIS
DEPARTMENT OF PHYSICS

Dissertation Examination Committee:
Kater Murch, Chair
Alexander Seidel
Chong Zu
Saori Pastore
Kade Head-Marsden

Quantum Information Processing via Dissipation Engineering in Superconducting Circuit Platform

by
Yunzhao Wang

A dissertation presented to
The Graduate School
of Washington University in
partial fullfillment of the
requirements for the degree
of Doctor of Philosophy

St. Louis, Missouri
August, 2023

Contents

List of Figures

List of Tables

Acknowledgements

As I arrive at the culmination of this academic expedition, I am profoundly grateful to the incredible individuals whose unwavering support and contributions have paved the way for the completion of this doctoral thesis.

At the forefront of this journey stands Professor Kater Murch, my esteemed advisor. Your dedication, mentorship, and unyielding belief in my potential have been nothing short of transformative. Your keen insights, boundless patience, and remarkable ability to nurture curiosity have not only guided the direction of my research but have also played a pivotal role in shaping me into the scientist I am today. I am deeply indebted to your profound impact on every aspect of this journey.

A special tribute is reserved for the esteemed members of my thesis committee-Professors Alexander Seidel, Kade Head-Marsden, Chong Zu, and Saori Pastore. Your rigorous evaluations, thoughtful critiques, and invaluable guidance have critically enriched the depth and scholarly rigor of this work. Your collective wisdom has been instrumental in refining the contours of this endeavor.

Collaborations have been a cornerstone of my academic growth, and I am privileged to have worked with luminaries such as Professor Yuval Gefen, Dr. Kyrylo Snizhko, and Dr. Alessandro Romito. Your expertise, shared insights, and collaborative spirit have not only expanded the horizons of my research but have also brought invaluable dimensions to this journey.

The vibrant intellectual ecosystem of the Murchlab has been an extraordinary source of inspiration. To the lab members-Dr. Weijian Chen, Dr. Xiayu Linpeng, Dr. Daria Kowsari, Xingrui Song, Chandrashekhar Gaikwad, Dr. Maryam Abbasi, Kaiwen Zheng, Serra Erdamar, Dr. Mahdi Naghiloo, Alexandria Udenkwo, Dr. Dian Tan, and Dr. Patrick Harrington-your camaraderie, shared aspirations, and collective pursuit of excellence have created an environment where academic growth thrives.

In the realm of friendship and companionship, I am profoundly grateful for the enduring bonds with Cong Wang and Yilin Ma. Your unwavering encouragement, shared laughter, and moments of respite have been a cherished support system throughout this academic expedition.

To my family-my mother and sister-words cannot capture the depth of my gratitude for your unwavering belief in my abilities and the constant encouragement you have provided. Your unwavering support has been a constant source of strength, driving me forward even in the face of challenges.

As I reflect upon the conclusion of this chapter, I recognize that the collective contributions of these extraordinary individuals have been instrumental in shaping this academic achievement. With heartfelt gratitude, I extend my deepest thanks to each person who has walked this journey with me.

Yunzhao Wang

Washington University in St. Louis
August, 2023

ABSTRACT OF THE DISSERTATION

Quantum Information Processing via Dissipation Engineering in Superconducting Circuit Platform

by

Yunzhao Wang

Doctor of Philosophy in Physics

Washington University in St.Louis, 2023

Kater Murch (Chair)

This thesis discusses the application of dissipative processes in quantum information processing. Conventionally, dissipative processes bring noises into quantum circuits and hinder the ability of computation. Here we explore several ways to engineer and utilize dissipative processes, as a novel approach for quantum information processing. In a single superconducting qutrit, we observe the topological behaviour of the geometric phase under the existence of dephasing. In a manybody superconducting qutrit processor, we design the preparation and stabilization of the AKLT state. By the above examples, we demonstrate the the power of dissipative processes as a novel and promising approach for quantum information processing.

1

Shut up and calculate.

—David Mermin

Chapter 1

Superconducting cQED

This chapter first introduces the Josephson junction, which is an important component in the engineering of superconducting circuits. We then describe the structure of a superconducting transmon and its interaction with the light field confined in a linear microwave cavity.

1.1 The Josephson Junction

Tunneling devices are ubiquitous in application as important components of electric circuits. Josephson discovered that in addition to electrons, Cooper pairs formed in superconductors can also have tunneling behaviors [1]. The Josephson effect happens when the system consists two or more superconductors coupled by a weak link, e.g. a thin insulating barrier or a section of normal metal. Here we consider the simplest situation, where two superconductors with

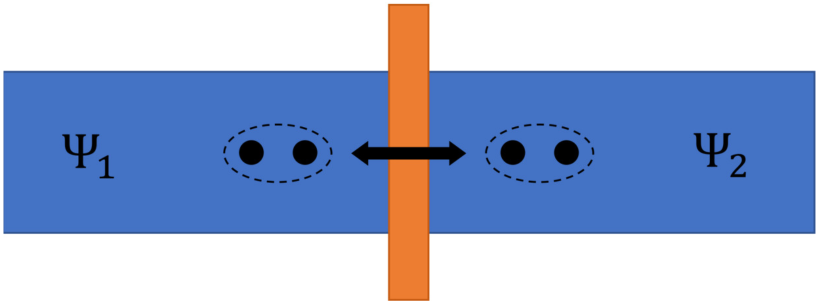

Fig. 1.1: Diagram of an example of the Josephson junction A Josephson junction formed by two pieces of same-material superconductors (blue) separated by a thin insulating layer (orange).

the same material are separated by a thin layer of insulator. For superconductors, we can assume a common wave function for all the Cooper pairs as $\Psi_1 = \sqrt{n_1}e^{i\phi_1}$ on one side and $\Psi_2 = \sqrt{n_2}e^{i\phi_2}$ on the other, as is shown in Fig. 1.1. Here $n_{1(2)}$ are the number density of the Cooper pairs and $\phi_{1(2)}$ are the phases on the two sides of superconductors. Considering the tunneling process, we have relation between the two wave functions

$$\begin{cases} i\hbar\dfrac{\partial\Psi_1}{\partial t} = eV\Psi_1 + K\Psi_2 \\ i\hbar\dfrac{\partial\Psi_2}{\partial t} = -eV\Psi_2 + K\Psi_1 \end{cases}, \tag{1.1}$$

when a voltage V is applied through the junction. Here the energy difference caused by one Cooper pair is $2eV$, and we set the middle point as the zero energy point. The parameter K features the characteristic of the junction for the tunneling event. Putting $\Psi_1 = \sqrt{n_1}e^{i\phi_1}$ and $\Psi_2 = \sqrt{n_2}e^{i\phi_2}$ into Equation 1.1, we get the relation between the phases and the number densities such that

$$\begin{cases} \dot{n}_1 = +\dfrac{2}{\hbar}K\sqrt{n_2 n_1}\sin\phi \\ \dot{n}_2 = -\dfrac{2}{\hbar}K\sqrt{n_2 n_1}\sin\phi \\ \dot{\phi}_1 = -\dfrac{K}{\hbar}\sqrt{\dfrac{n_2}{n_1}}\cos\phi - \dfrac{eV}{\hbar} \\ \dot{\phi}_2 = -\dfrac{K}{\hbar}\sqrt{\dfrac{n_1}{n_2}}\cos\phi + \dfrac{eV}{\hbar} \end{cases}. \tag{1.2}$$

Here we note that $\phi_2 - \phi_1 = \phi$. Although the number density of Cooper pairs varies through time, we should notice here that the imbalance of carriers is much smaller compared to the total number of carriers in the superconducting islands. This can be seen with a simple estimation for a typical Josephson junction in use, e.g. the ones used for Transmon qubits, which we will discuss later. Such restrictions on the particle number difference is put by the constraint that the chemical potential difference must be less than the quasiparticle gap. Thus, here for the case of superconducting Josephson junction, we are just working within the small imbalance limit of the model. To access a larger range of parameters for this model, e.g. the regime of "self-trapping", we have to make observations in the so-called Bose Josephson junction system [2]. Anyways, back to Equation 1.2 with this important new approximation we just got, $n_1 \approx n_2 \approx n_0$, where n_0 is the normal density of carriers in the superconducting material, the voltage-current relation could be obtained that

$$\begin{cases} J = 2e\dot{n}_1 = \dfrac{4eK}{\hbar} n_0 \sin\phi = J_0 \sin\phi \\ V = \dfrac{\hbar}{2e}\dot{\phi} = \dfrac{\Phi_0}{2\pi}\dot{\phi} \end{cases}. \tag{1.3}$$

Notice here that the inductance of the Josephson junction is thus

$$L = \frac{V}{\dot{J}} = \frac{\hbar\dot{\phi}}{2eJ_0\cos\phi\dot{\phi}} = \frac{\hbar}{2eJ_0}\frac{1}{\cos\phi} = \frac{L_0}{\cos\phi} = \frac{L_0}{\sqrt{1-\left(\frac{J}{J_0}\right)^2}} = L(J), \tag{1.4}$$

where the inductance depends on the value of current and thus brings on nonlinear effects. Such nonlinear response makes the Josephson junction a perfect and simple choice for a nonlinear circuit element when no dissipation is desired.

Now we explore the relation between the two variables capturing the Josephson junction, the Cooper pair tunneling through, n, and the phase difference, ϕ. Since the energy for the Josephson junction part, U, has the time derivative $dU/dt = JV = (J_0\hbar/2e)(\sin\phi)\dot{\phi}$, then it should be $U = -E_J\cos\phi$ up to a constant, which is not important. We obtain the total Hamiltonian in this situation,

$$H = -E_J\cos\phi - 2eVn \tag{1.5}$$

where $E_J = J_0\hbar/2e$. From Equation 1.3 we already have

$$\begin{cases} \dot{n} = \dfrac{J_0}{2e}\sin\phi = \dfrac{E_J}{\hbar}\sin\phi = \dfrac{1}{\hbar}\dfrac{\partial H}{\partial\phi} \\ \dot{\phi} = \dfrac{2eV}{\hbar} = -\dfrac{1}{\hbar}\dfrac{\partial H}{\partial n} \end{cases}, \tag{1.6}$$

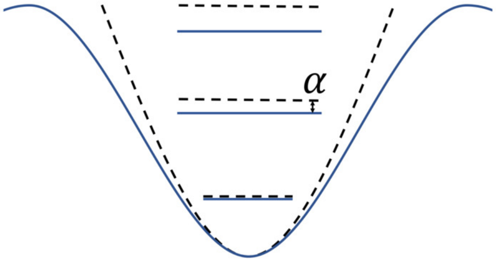

Fig. 1.2: Diagram of harmonic and anhamonic energy levels The black dashed lines features the quadratic potential and equally spaced energy levels of a harmonic oscillator. The blue lines features the potential beyond quadratic terms, and the unequally spaced energy levels with an anharmonicity, $-\alpha$.

so it is natural to observe that n and ϕ are conjugate variables. For example, for a typical pair of conjugate variables x and p, we have that $\dot{x} = \partial H/\partial p$, $\dot{p} = -\partial H/\partial x$, which results in relation $[\hat{x}, \hat{p}] = i\hbar$ when migrating to the quantum descriptions. By a similar process, we can obtain that $[\hat{n}, \hbar\hat{\phi}] = i\hbar$ and thus $[\hat{n}, \hat{\phi}] = i$ in quantum descriptions.

1.2 Superconducting Transmon

Making qubit/qudit requires such nonlinear elements without dissipation as we mentioned in the previous section. If the circuit is totally constructed by linear elements, e.g. by linear capacitance and inductance, it will form a harmonic oscillator, where the spacings between adjacent energy levels are identical. In that case, when a coherent drive is applied to the ground state of the oscillator, we can only get coherent states, which is basically classical. Only by introducing nonlinear elements, can the anharmonicity be realized, where the energy spacings are unequal and thus they could be addressed independently (Fig. 1.2). By applying coherent drives with certain corresponding frequencies, drives can be only applied between the ground state and the excited state, forming a two-level system as a qubit. Considering more energy levels and apply control between them separately, we could obtain a qudit system.

Applying the Josephson junction as the source of nonlinearity, we hereby introduce a workhorse qubit/qudit in recent researches, the superconducting Transmon [3]. We consider the Josephson junction shunted by a large capacitor resulting in total capacitance C for the entire circuit. This brings an additional term to the Hamiltonian,

$$\hat{H} = 4E_C(\hat{n} - n_g)^2 - E_J \cos\hat{\phi}. \tag{1.7}$$

Here $E_C = e^2/2C$, and n_g is the offset charge determined by the gate voltage as well as the related environmental degree of freedom. In the Transmon regime, different from the conventional Cooper pair box, we work in the limit that $E_J/E_C \to \infty$. This Hamiltonian is exactly solvable with Mathieu functions [4]. But we can also find the energy levels perturbatively assuming that ϕ varies in a small range around a point e.g. $\phi = 0$. Viewing Equation 1.7 as a rotor moving in the cosine potential, it is easy to see that the small ϕ limit corresponds to large E_J/E_C and lower energy levels. Thus, we can find the lower levels of the Transmon eigenenergy approximating the cosine term to the fourth order,

$$-E_J \cos\phi \simeq -E_J + \frac{E_J}{2}\phi^2 - \frac{E_J}{24}\phi^4. \tag{1.8}$$

With such approximation the eigenenergies could be written as

$$E_m \simeq -E_J + \sqrt{8E_C E_J}\left(m + \frac{1}{2}\right) - \frac{E_C}{12}(6m^2 + 6m + 3), \tag{1.9}$$

where the first several energy spacings are $E_{01} = E_1 - E_0 = \sqrt{8E_J E_C} - E_C$, $E_{12} = E_2 - E_1 = \sqrt{8E_J E_C} - 2E_C$, $E_{23} = E_2 - E_1 = \sqrt{8E_J E_C} - 3E_C$, $E_{34} = E_2 - E_1 = \sqrt{8E_J E_C} - 4E_C$,.... The anharmonicity, $\alpha = -E_C$, here gives us independent control between each energy level, forming a fully controllable multi-level system as the qudit, and also the qubit when we reduce to the two-level case.

The above calculations are for the simplified model with only one single Josephson junction in the circuit. Now we consider the case with two Josephson junctions connected in parallel, which brings us a flux degree of control [5]. The energy across the two Josephson junctions, which could also be asymmetric, here becomes

$$-E_J \cos\hat{\phi} \rightarrow -E_{J1}\cos\hat{\phi}_1 - E_{J2}\cos\hat{\phi}_2. \tag{1.10}$$

When we consider the superconducting ring under a magnetic field, we generally replace the operator $(\hbar/i)\Delta$ with $(\hbar/i)\Delta - 2eA$. Thus, assuming that the carrier density varies negligibly, for the wave function, e.g. $\sqrt{n_1(\vec{r})}e^{i\phi_1(\vec{r})}$, we have the current

$$\vec{J} = \frac{\hbar}{m}\left(\vec{\nabla}\phi_1(\vec{r}) - \frac{2e}{\hbar}\vec{A}\right) n_1(\vec{r}), \tag{1.11}$$

where m is the mass and $\vec{A}$ is the vector potential. Also assuming that the current density in the superconducting body is zero, we have

$$\oint \vec{\nabla}\phi_1(\vec{r})\cdot d\vec{s} = \frac{2e}{\hbar}\oint \vec{A}\cdot d\vec{s} = \frac{2\pi\Phi}{\Phi_0}, \tag{1.12}$$

where $\Phi = \oint \vec{A}\cdot d\vec{s}$ is the magnetic flux across the ring. Then we have the relation between the two phase changes across the two Josephson junctions,

$$\phi_1 - \phi_2 = 2\pi n + \frac{2\pi\Phi}{\Phi_0}. \tag{1.13}$$

Then the Hamiltonian can be written as $\hat{H}_J(\Phi) = -E'_J(\Phi)\cos(\hat{\phi} - \phi_0)$, where

$$E'_J(\Phi) = E_{J\Sigma}\cos\left(\frac{\pi\Phi}{\Phi_0}\right)\sqrt{1 + d^2\tan^2\left(\frac{\pi\Phi}{\Phi_0}\right)}, \quad \tan\phi_0 = d\tan\left(\frac{\pi\Phi}{\Phi_0}\right). \tag{1.14}$$

Here $E_{J\Sigma} = E_{J1} + E_{J2}$ and $d = (\alpha - 1)/(\alpha + 1)$, where $\alpha = E_{J1}/E_{J2}$ assuming that $E_{J1} > E_{J2}$. Obviously, the tunability increases as the difference in junction energies decreases. Such qubit with flux-tunable frequencies are the basis for the implementation discussed in Section 5.3.2.

With either fixed or flux-tuable qudit/qubit in an equivalent form, we can check its interaction with the electromagnetic field confined in a superconducting resonator. Considering the voltage felt by the Transmon, we have [3, 6]

$$\hat{H} = 4E_C(\hat{n} - n_g)^2 - E_J \cos\hat{\phi} + \hbar\omega_r \hat{a}^\dagger \hat{a} + V_0 \hat{n}(\hat{a} + \hat{a}^\dagger). \tag{1.15}$$

Here V_0 is a parameter determined by the root-mean-square voltage of the local oscillator as well as the capacitance for the structure of the circuit. $\omega_r/2\pi$ is the resonance frequency of the resonator and $\hat{a}^\dagger(\hat{a})$ is the creation (annihilation) operator of the photons in the resonator. Writing the Cooper pair number operator in the basis of the Transmon eigenstates, we find that

$$\hat{n} = \sum_{i,j} n_{ij} |i\rangle\langle j|, \quad n_{ij} = \langle i|\hat{n}|j\rangle. \tag{1.16}$$

From asymptotic results same as in Equation 1.8, we see the above matrix elements as

$$\begin{aligned} &|\langle j+1|\hat{n}|j\rangle| \simeq \sqrt{\frac{j+1}{2}} \left(\frac{E_J}{8E_C}\right)^{1/4} \\ &|\langle j+k|\hat{n}|j\rangle| \to 0, \quad |k| > 1. \end{aligned} \tag{1.17}$$

Thus, after rotating wave approximation, we obtain the effective generalized Jaynes-Cummings Hamiltonian

$$\hat{H} = \hbar \sum_j \omega_j |j\rangle\langle j| + \hbar\omega_r \hat{a}^\dagger \hat{a} + \left(\hbar \sum_i g_{i,i+1} |i\rangle\langle i+1| \hat{a}^\dagger + h.c.\right). \tag{1.18}$$

1.3 The dispersive regime

For a Transmon qudit dispersively coupled to a linear cavity [6, 7], as we approach the limit that $E_j \gg E_c$, and apply the rotating wave approximation, the system Hamiltonian should be,

$$\begin{aligned}
\hat{H} &= \hat{H}_0 + \hat{V}, \\
\hat{H}_0 &= \hbar \sum_j \omega_j |j\rangle\langle j| + \hbar\omega_r \hat{a}^\dagger \hat{a}, \\
\hat{V} &= \hbar \sum_i g_{j,j+1}(|j\rangle\langle j+1|\hat{a}^\dagger + |j+1\rangle\langle j|\hat{a}).
\end{aligned} \tag{1.19}$$

Here the coupling strength $g_{i,i+1} \approx \sqrt{i+1} g_0$ is proportional to the non-zero element of the Cooper pair number operator. [3] [depends on introductions of notions before] In the dispersive limit, the detuning between adjacent energy level differences of the qutrit is much larger than the coupling strengths. This allows us to perform the Schrieffer-Wolff transformation, which can approximately diagonalize the system Hamiltonian in the dispersive limit, $\hat{H}_{\text{eff}} = e^{-\hat{S}} \hat{H} e^{\hat{S}}$, with

$$\hat{S} = \sum_i \lambda_i (|i+1\rangle\langle i|\hat{a} - |i\rangle\langle i+1|\hat{a}^\dagger), \tag{1.20}$$

where $\lambda_i = g_{i,i+1}/(\omega_{i,i+1} - \omega_r)$, and $\omega_{i,i+1} = \omega_{i+1} - \omega_i$. From

$$\begin{aligned}
&[\hat{a}, \hat{a}^\dagger\hat{a}] = \hat{a},\ \ [\hat{a}^\dagger, \hat{a}^\dagger\hat{a}] = -\hat{a}^\dagger,\ \ [|i+1\rangle\langle i|, |j\rangle\langle j|] = \delta_{i,j}|i+1\rangle\langle i| - \delta_{i+1,j}|i+1\rangle\langle i| \\
&[|i\rangle\langle i+1|, |j\rangle\langle j|] = \delta_{i+1,j}|i\rangle\langle i+1| - \delta_{i,j}|i\rangle\langle i+1|
\end{aligned} \tag{1.21}$$

we can have

$$[\hat{S}, \hat{H}_0] = \hbar \sum_i \lambda_i (-\omega_{i+1} + \omega_i + \omega_r)(|i+1\rangle\langle i|\hat{a} + |i\rangle\langle i+1|\hat{a}^\dagger), \tag{1.22}$$

here the relation $[\hat{S}, \hat{H}_0] + \hat{V} = 0$ stands. Also, from the Baker-Campbell-Hausdorff relation, there is $\hat{H}_{\text{eff}} = \hat{H}_0 + \hat{V} + [\hat{S}, \hat{H}_0] + [\hat{S}, \hat{V}] + \frac{1}{2}[\hat{S}, [\hat{S}, \hat{H}_0]] + \frac{1}{2}[\hat{S}, [\hat{S}, \hat{V}]] + ...$ Then we have,

$\hat{H}_{\text{eff}} = \hat{H}_0 + \frac{1}{2}[\hat{S}, \hat{V}] + O(\lambda^2)$. In that sense we calculate $[\hat{S}, \hat{V}]$, from

$$\begin{aligned} [|i+1\rangle\langle i|\hat{a}, |j+1\rangle\langle j|\hat{a}] &= \delta_{i,j+1}|i+1\rangle\langle i-1|\hat{a}\hat{a} - \delta_{i+1,j}|i+2\rangle\langle i|\hat{a}\hat{a}, \text{and} \\ [|i+1\rangle\langle i|\hat{a}, |j\rangle\langle j+1|\hat{a}^\dagger] &= \delta_{i,j}|i+1\rangle\langle i+1| - \hat{a}^\dagger\hat{a}(\delta_{i,j}|i+1\rangle\langle i+1| - \delta_{i,j}|i\rangle\langle i|), \end{aligned} \tag{1.23}$$

we can have,

$$\begin{aligned} [\hat{S}, \hat{V}] &= \hbar\sum_i(\lambda_{i+1}g_{i,i+1} - \lambda_i g_{i+1,i+2})(|i+2\rangle\langle i|\hat{a}\hat{a} + |i\rangle\langle i+2|\hat{a}^\dagger\hat{a}^\dagger) \\ &+2\hbar\sum_i \chi_{i,i+1}|i+1\rangle\langle i+1| + 2\hbar\sum_{i=1}^{\infty}(\chi_{i-1,i} - \chi_{i,i+1})|i\rangle\langle i|\hat{a}^\dagger\hat{a} - 2\hbar\chi_{0,1}|0\rangle\langle 0|\hat{a}^\dagger\hat{a}. \end{aligned} \tag{1.24}$$

With the two-photon transition term involving $\hat{a}\hat{a}$ and $\hat{a}^\dagger\hat{a}^\dagger$ small and can be omitted, the final Hamiltonian becomes,

$$\begin{aligned} H_{\text{eff}} = \hbar\sum_j \omega_j|j\rangle\langle j| + \hbar\omega_r\hat{a}^\dagger\hat{a} + \hbar\sum_i \chi_{i,i+1}|i+1\rangle\langle i+1| \\ +\hbar\sum_{i=1}^{\infty}(\chi_{i-1,i} - \chi_{i,i+1})|i\rangle\langle i|\hat{a}^\dagger\hat{a} - \hbar\chi_{0,1}|0\rangle\langle 0|\hat{a}^\dagger\hat{a} \end{aligned} \tag{1.25}$$

Here $\chi_{i,i+1}$ is defined as $\lambda_i g_{i,i+1}$ which is $g_{i,i+1}^2/(\omega_{i,i+1} - \omega_r)$. We can see that, for a superconducting qudit interacting with cavity modes in the dispersive limit, the energy-level-dependent shifts for the cavity resonance frequency take the form similiar to the case where a two-level system is coupled to the cavity. The term in the second line of the equation, which involves $|i\rangle\langle i|\hat{a}^\dagger\hat{a}$, can be explained both as a shift in the cavity frequency dependent on the state of the qudit, or as a shift in the qudit energy levels dependent on the number of photons in the cavity. Due to reduced aharmonicity for a superconducting transmon design, higher level cavity shifts interfere with each other, resulting in the cavity shift between ground state $|0\rangle$ and the first excited state $|1\rangle$ as $2\chi_{0,1} - \chi_{1,2}$, and, for $i \geq 1$, the cavity shift between state $|i\rangle$ and state $|i+1\rangle$ as $2\chi_{i,i+1} - \chi_{i-1,i} - \chi_{i+1,i+2}$.

1.4 Relaxation and dephasing of the Transmon qubit

Here we consider the intrinsic dissipation channels for a typical single Transmon qubit. With the descriptions inherited from the NMR case [8], superconducting qubits dissipation channels are dominated by the longitudinal relaxation (depolarization) rate $\Gamma_1 = T_1^{-1}$ and the transverse relaxation (dephasing) rate $\Gamma_2 = T_2^{-1}$. The qubit relaxation time, T_1, is characterized by the diagonal term of the density matrix, $\rho_{ee}(t) = \rho_{ee}(0)e^{-\frac{t}{T_1}}$, which reflects random relaxation event from state $|e\rangle$ to state $|g\rangle$, emitting energy in the form of photons into the environment. The qubit dephasing time, T_2, is characterized by the cross term of the density matrix, $|\rho_{ge}(t)| = |\rho_{ge}(0)|e^{-\frac{t}{T_2}}$, which reflects fluctuations in the energy levels due to variations in the parameters, e.g. offset charge, flux, E_C or E_J. Here, the dephasing process consists of contributions from the longitudinal relaxation rate, Γ_1, and from the pure dephasing rate, $\Gamma_\phi = T_\phi^{-1}$, with relation $\Gamma_2 = \Gamma_1/2 + \Gamma_\phi$. This could also be reflected in the Lindblad master equation [9],

$$\dot{\rho} = \mathcal{L}\rho = \Gamma_1 \mathcal{D}[\hat{\sigma}_-]\rho + \frac{\Gamma_\phi}{2}\mathcal{D}[\hat{\sigma}_z]\rho, \tag{1.26}$$

where $\mathcal{D}[\hat{L}]\rho = (2\hat{L}\rho\hat{L}^\dagger - \hat{L}^\dagger\hat{L}\rho - \rho\hat{L}^\dagger\hat{L})/2$, $\hat{\sigma}_z$ is the Pauli operator and $\hat{\sigma}_- = |g\rangle\langle e|$.

For a qudit, the noise constituents could be more complex than the qubit case. For the relaxation process from state $|i\rangle$ to state $|j\rangle$ $(i > j)$, there are certain selection rules for the main relaxation mechanisms. For example, for spontaneous emission altered by the presence of the resonator, namely the Purcell effect, its rate in the dispersive limit in the absence of cavity photons is $\Gamma_1^{i,i+1} \propto g_{i,i+1}^2/(\omega_{i,i+1} - \omega_r)^2$ [3] before Purcell filtering. This dominating relaxation process poses selection rules contributing to spontaneous emission only from state $|i+1\rangle$ to state $|i\rangle$. Meanwhile, since the coupling strengths associated with higher levels increase as $g_{i,i+1} = \sqrt{i+1}g_0$, the relaxation rate related to this mechanism scales linearly with the level number involved, which indicates shorter relaxation time between higher levels. In the Lindblad master equation, to count for the spontaneous emission process for a single qudit, we can substitute the qubit term

$$\Gamma_1 \mathcal{D}[\hat{\sigma}_-]\rho \rightarrow \sum_i \Gamma_1^{i,i+1} \mathcal{D}[\hat{\sigma}_-^{i,i+1}]\rho, \tag{1.27}$$

where $\hat{\sigma}_-^{i,i+1} = |i\rangle\langle i+1|$. In the qutrit case, for example, we could hereby mainly consider the energy relaxation directly from state $|e\rangle$ to state $|g\rangle$ or from state $|f\rangle$ to state $|e\rangle$, omitting the two-level energy relaxation directly from state $|f\rangle$ to state $|g\rangle$, which should be smaller according to noise analysis. This is adapted in Section 3.4.2.3.

For the dephasing processes, we mainly consider the fluctuations on the qudit energy levels to obtain the pure dephasing rate between each two levels. Away from the sweet spot of a certain parameter α, we consider the system Hamiltonian in the rotating frame for the averaged energy levels,

$$\delta H = \hbar \sum_i \delta\omega_i |i\rangle\langle i| = \hbar \sum_i \frac{\partial \omega_i}{\partial \alpha} \delta\alpha |i\rangle\langle i|, \tag{1.28}$$

with $\delta\alpha$ being a parameter fluctuating around according to the environment noise spectrum. At the sweet spot of parameter α, we have $\partial\omega_i/\partial\alpha|_{\alpha=\alpha_0} = 0$, then the system Hamiltonian fluctuates as

$$\delta H = \hbar \sum_i \delta\omega_i |i\rangle\langle i| = \hbar \sum_i \frac{\partial^2 \omega_i}{\partial \alpha^2} \frac{\delta\alpha^2}{2} |i\rangle\langle i|. \tag{1.29}$$

Here, according to Bloch-Redfield theory [10, 11, 8], for noise spectrum defined well around $\omega = 0$, the dephasing is of the exponential form, written as $\rho_{ij}(t) = \rho_{ij}(0)\exp\left(-\Gamma_\phi^{ij} t\right)$. From the same noise source, the induced dephasing rate between each two levels are quadratic to the corresponding derivative of the energy difference, in form of $\Gamma_\phi^{ij} = \gamma_\alpha^{(1)} (\partial\omega_{ij}/\partial\alpha)^2|_{\alpha=\alpha_0}$ away from the sweet spot and $\Gamma_\phi^{ij} = \gamma_\alpha^{(2)} (\partial^2\omega_{ij}/\partial\alpha^2)^2|_{\alpha=\alpha_0}$ at the sweet spot. Phenomenally, this dephasing process can be described in the Lindblad master equation as,

$$\frac{\Gamma_\phi}{2} \mathcal{D}[\hat{\sigma}_z]\rho \rightarrow 2\gamma_\alpha^{(1)} \mathcal{D}\left[\sum_i \frac{\partial\omega_i}{\partial\alpha} |i\rangle\langle i|\right]\rho, \tag{1.30}$$

for the parameter α away from the sweet spot, and as,

$$\frac{\Gamma_\phi}{2}\mathcal{D}[\hat{\sigma}_z]\rho \to 2\gamma_\alpha^{(2)}\mathcal{D}\left[\sum_i \frac{\partial^2\omega_i}{\partial\alpha^2}|i\rangle\langle i|\right]\rho, \tag{1.31}$$

for the parameter α at the sweet spot. However, in quantum experiments, the existence of $1/f$ noise is ubiquitous, which has a divergent behaviour in the noise spectrum around $\omega = 0$. By further calculations, this gives us dephasing in the form of $\rho_{ij}(t) = \rho_{ij}(0)\exp\left(-\Gamma_\phi^{ij\,2}t^2\right)$ [3, 8]. By similar scaling behaviours in $\Gamma_\phi^{ij\,2}$ for the derivatives of the energy level differences, we have the induced dephasing rate as $\Gamma_\phi^{ij} = \sqrt{\gamma_\alpha^{(1)}}\partial\omega_{ij}/\partial\alpha|_{\alpha=\alpha_0}$ away from the sweet spot and $\Gamma_\phi^{ij}(t) = \sqrt{\gamma_\alpha^{(2)}}\partial^2\omega_{ij}/\partial\alpha^2|_{\alpha=\alpha_0}$ at the sweet spot. Still phenomenally, this process could be described by the Lindblad master equation with time-dependent parameters. For the parameter away from the sweet spot, the Lindbladian becomes,

$$\frac{\Gamma_\phi}{2}\mathcal{D}[\hat{\sigma}_z]\rho \to 4\gamma_\alpha^{(1)}t\mathcal{D}\left[\sum_i \frac{\partial\omega_i}{\partial\alpha}|i\rangle\langle i|\right]\rho, \tag{1.32}$$

and for the parameter at the sweet spot,

$$\frac{\Gamma_\phi}{2}\mathcal{D}[\hat{\sigma}_z]\rho \to 4\gamma_\alpha^{(2)}t\mathcal{D}\left[\sum_i \frac{\partial^2\omega_i}{\partial\alpha^2}|i\rangle\langle i|\right]\rho. \tag{1.33}$$

Such description applies to several parameters causing the energy level fluctuations as is mentioned before. The above equivalent behaviors between the noise description and the Lindblad master equation was confirmed by simulations in Qutip [12, 13] and in HOQST [14], with the latter having specific function of modelling $1/f$ noise stochastically with fluctuating Hamiltonians. Since those dephasing mechanisms need more characterization, we just consider a very rough noise model in Section 3.4.2.3 corresponding to the dephasing process, where the dephasing operator $\hat{\sigma}_z$ is considered between adjacent states, in order to roughly simulate the noise levels.

1.5 Quantum non-demolition measurement in the dispersive regime

Starting from Eqn. 1.25, here we apply an additional term for the cavity probe with detuning Δ from the shifted cavity frequency. We thus have the Hamiltonian simply written as

$$H_{\mathrm{eff}} = \hbar \sum_{i=0}^{\infty} \chi_i |i\rangle\langle i| \hat{a}^\dagger \hat{a} + \hbar\epsilon(\hat{a}^\dagger + \hat{a}) + \hbar\Delta\hat{a}^\dagger\hat{a}, \tag{1.34}$$

in the rotating frame of the cavity probe and qudit frequencies. Considering the dissipation of the cavity photon for a finite cavity linewidth (FWHM), κ, and ignoring the intrinsic qudit dephasing and relaxation at this point, we have the Lindblad master equation [9] as

$$\dot{\rho} = \mathcal{L}\rho = -\frac{i}{\hbar}[H_{\mathrm{eff}}, \rho] + \kappa\mathcal{D}[\hat{a}]\rho, \tag{1.35}$$

where $\mathcal{D}[\hat{L}]\rho = (2\hat{L}\rho\hat{L}^\dagger - \hat{L}^\dagger\hat{L}\rho - \rho\hat{L}^\dagger\hat{L})/2$. Following the argument in previous work [15] going beyond the Gaussian approximation, we have the time-evolved full density matrix for the qudit-cavity system as

$$\rho = \sum_{i,j} \hat{\rho}_{ij} \otimes |i\rangle\langle j|. \tag{1.36}$$

Then we obtain the differential equations for $\hat{\rho}_{ij}$,

$$\dot{\hat{\rho}}_{ij} = -i(\chi_i \hat{a}^\dagger\hat{a}\hat{\rho}_{ij} - \chi_j\hat{\rho}_{ij}\hat{a}^\dagger\hat{a}) - i\epsilon[\hat{a}^\dagger + \hat{a}, \hat{\rho}_{ij}] - i\Delta[\hat{a}^\dagger\hat{a}, \hat{\rho}_{ij}] + \kappa\mathcal{D}[\hat{a}]\hat{\rho}_{ij}. \tag{1.37}$$

Now we assume the density matrices as

$$\hat{\rho}_{ij} = c_{ij}(t)|\alpha_i(t)\rangle\langle\alpha_j(t)|, \tag{1.38}$$

to solve the above equations. Still we have the relations

$$\hat{a}|\alpha\rangle = \alpha|\alpha\rangle, \quad \hat{a}^\dagger|\alpha\rangle = \left(\partial_\alpha + \frac{\alpha^*}{2}\right)|\alpha\rangle. \tag{1.39}$$

Putting Equation 1.38 into Equation 1.37, we obtain that

$$\begin{aligned}
&\dot{c}_{ij}(t)|\alpha_i(t)\rangle\langle\alpha_j(t)| + c_{ij}(t)|\dot{\alpha}_i(t)\rangle\langle\alpha_j(t)| + c_{ij}(t)|\alpha_i(t)\rangle\langle\dot{\alpha}_j(t)| \\
&= c_{ij}(t)\Big[-i\left(\chi_i + \Delta - \frac{\kappa}{2}i\right)\hat{a}^\dagger\hat{a}|\alpha_i(t)\rangle\langle\alpha_j(t)| + i\left(\chi_j + \Delta + \frac{\kappa}{2}i\right)|\alpha_i(t)\rangle\langle\alpha_j(t)|\hat{a}^\dagger\hat{a} \\
&-i\epsilon(\hat{a}^\dagger + \hat{a})|\alpha_i(t)\rangle\langle\alpha_j(t)| + i\epsilon|\alpha_i(t)\rangle\langle\alpha_j(t)|(\hat{a}^\dagger + \hat{a}) + \kappa\hat{a}|\alpha_i(t)\rangle\langle\alpha_j(t)|\hat{a}^\dagger\Big] \\
&= c_{ij}(t)\Big[-i\left(\chi_i + \Delta - \frac{\kappa}{2}i\right)\alpha_i(t)\hat{a}^\dagger|\alpha_i(t)\rangle\langle\alpha_j(t)| - i\epsilon(\hat{a}^\dagger + \alpha_i(t))|\alpha_i(t)\rangle\langle\alpha_j(t)| \\
&+ i\left(\chi_j + \Delta + \frac{\kappa}{2}i\right)\alpha_j^*(t)|\alpha_i(t)\rangle\langle\alpha_j(t)|\hat{a} + i\epsilon|\alpha_i(t)\rangle\langle\alpha_j(t)|(\alpha_j^*(t) + \hat{a}) \\
&+\kappa\alpha_i(t)\alpha_j^*(t)|\alpha_i(t)\rangle\langle\alpha_j(t)|\Big] \\
&= c_{ij}(t)\Big[-i\left(\chi_i + \Delta - \frac{\kappa}{2}i\right)\alpha_i(t)\partial_\alpha|\alpha_i(t)\rangle\langle\alpha_j(t)| - i\epsilon\partial_\alpha|\alpha_i(t)\rangle\langle\alpha_j(t)| \\
&+ i\left(\chi_j + \Delta + \frac{\kappa}{2}i\right)\alpha_j^*(t)|\alpha_i(t)\rangle\partial_{\alpha^*}\langle\alpha_j(t)| + i\epsilon|\alpha_i(t)\rangle\partial_{\alpha^*}\langle\alpha_j(t)| \\
&- i\left(\chi_i + \Delta - \frac{\kappa}{2}i\right)\frac{\alpha_i(t)\alpha_i^*(t)}{2}|\alpha_i(t)\rangle\langle\alpha_j(t)| - i\epsilon\left(\frac{\alpha_i^*(t)}{2} + \alpha_i(t)\right)|\alpha_i(t)\rangle\langle\alpha_j(t)| \\
&+ i\left(\chi_j + \Delta + \frac{\kappa}{2}i\right)\frac{\alpha_j(t)\alpha_j^*(t)}{2}|\alpha_i(t)\rangle\langle\alpha_j(t)| + i\epsilon\left(\frac{\alpha_j(t)}{2} + \alpha_j^*(t)\right)|\alpha_i(t)\rangle\langle\alpha_j(t)| \\
&+\kappa\alpha_i(t)\alpha_j^*(t)|\alpha_i(t)\rangle\langle\alpha_j(t)|\Big].
\end{aligned} \tag{1.40}$$

Notice that we have the derivatives of the coherent states written as

$$|\dot{\alpha}_i(t)\rangle = \dot{\alpha}_i(t)\partial_\alpha|\alpha_i(t)\rangle + \dot{\alpha}_i^*(t)\partial_{\alpha^*}|\alpha_i(t)\rangle = \dot{\alpha}_i(t)\partial_\alpha|\alpha_i(t)\rangle - \frac{\alpha_i(t)\dot{\alpha}_i^*(t)}{2}|\alpha_i(t)\rangle. \tag{1.41}$$

We first put forward the differential equations for those coherent states,

$$\begin{aligned}
\dot{\alpha}_i(t)\partial_\alpha|\alpha_i(t)\rangle\langle\alpha_j(t)| &= -i\left(\chi_i + \Delta - \frac{\kappa}{2}i\right)\alpha_i(t)\partial_\alpha|\alpha_i(t)\rangle\langle\alpha_j(t)| - i\epsilon\partial_\alpha|\alpha_i(t)\rangle\langle\alpha_j(t)|, \\
\dot{\alpha}_i(t)\partial_\alpha|\alpha_i(t)\rangle\langle\dot{\alpha}_j(t)| &= i\left(\chi_j + \Delta + \frac{\kappa}{2}i\right)\alpha_j^*(t)|\alpha_i(t)\rangle\partial_{\alpha^*}\langle\alpha_j(t)| + i\epsilon|\alpha_i(t)\rangle\partial_{\alpha^*}\langle\alpha_j(t)|.
\end{aligned} \tag{1.42}$$

Such relations are equivalent to that

$$\dot{\alpha}_i(t) = -i\left(\chi_i + \Delta - \frac{\kappa}{2}i\right)\alpha_i(t) - i\epsilon, \quad \dot{\alpha}_j^*(t) = i\left(\chi_j + \Delta + \frac{\kappa}{2}i\right)\alpha_j^*(t) + i\epsilon. \tag{1.43}$$

Also we have the differential equations for the coefficients as

$$\begin{aligned}
&\dot{c}_{ij}(t)|\alpha_i(t)\rangle\langle\alpha_j(t)| - \frac{\alpha_i(t)\dot{\alpha}_i^*(t)}{2}c_{ij}(t)|\alpha_i(t)\rangle\langle\alpha_j(t)| - \frac{\dot{\alpha}_j(t)\alpha_j^*(t)}{2}c_{ij}(t)|\alpha_i(t)\rangle\langle\alpha_j(t)| \\
&= \Bigg[-i\left(\chi_i + \Delta - \frac{\kappa}{2}i\right)\frac{\alpha_i(t)\alpha_i^*(t)}{2}|\alpha_i(t)\rangle\langle\alpha_j(t)| - i\epsilon\left(\frac{\alpha_i^*(t)}{2} + \alpha_i(t)\right)|\alpha_i(t)\rangle\langle\alpha_j(t)| \\
&+ i\left(\chi_j + \Delta + \frac{\kappa}{2}i\right)\frac{\alpha_j(t)\alpha_j^*(t)}{2}|\alpha_i(t)\rangle\langle\alpha_j(t)| + i\epsilon\left(\frac{\alpha_j(t)}{2} + \alpha_j^*(t)\right)|\alpha_i(t)\rangle\langle\alpha_j(t)| \\
&+\kappa\alpha_i(t)\alpha_j^*(t)|\alpha_i(t)\rangle\langle\alpha_j(t)|\Bigg] c_{ij}(t).
\end{aligned} \tag{1.44}$$

We then assume the form of the coefficients as

$$c_{ij}(t) = \frac{a_{ij}(t)}{\langle\alpha_j(t)|\alpha_i(t)\rangle} = a_{ij}(t)e^{\frac{1}{2}(|\alpha_j(t)|^2 + |\alpha_i(t)|^2 - 2\alpha_j^*(t)\alpha_i(t))}. \tag{1.45}$$

Then we have the differential equation for the coefficients as

$$\begin{aligned}
&\frac{\dot{a}_{ij}(t)}{a_{ij}(t)}c_{ij}(t) + \left(\frac{\dot{\alpha}_i(t)\alpha_i^*(t) + \alpha_j(t)\dot{\alpha}_j^*(t)}{2} - \dot{\alpha}_j^*(t)\alpha_i(t) - \alpha_j^*(t)\dot{\alpha}_i(t)\right)c_{ij}(t), \\
&= \left\{\left[-i\left(\chi_i + \Delta - \frac{\kappa}{2}i\right)\alpha_i(t) - i\epsilon\right]\frac{\alpha_i^*(t)}{2} + \left[i\left(\chi_j + \Delta + \frac{\kappa}{2}i\right)\alpha_j^*(t) + i\epsilon\right]\frac{\alpha_j(t)}{2}\right. \\
&\left. - \left(-i\epsilon - \frac{\kappa}{2}\alpha_i(t) - i\Delta\alpha_i(t)\right)\alpha_j^*(t) - \left(i\epsilon - \frac{\kappa}{2}\alpha_j^*(t) + i\Delta\alpha_j^*(t)\right)\alpha_i(t)\right\} c_{ij}(t) \\
&= \left[\frac{\dot{\alpha}_i(t)\alpha_i^*(t)}{2} + \frac{\alpha_j(t)\dot{\alpha}_j^*(t)}{2} - \dot{\alpha}_i(t)\alpha_j^*(t) - \dot{\alpha}_j^*(t)\alpha_i(t) + i(\chi_j - \chi_i)\alpha_i(t)\alpha_j^*(t)\right] c_{ij}(t),
\end{aligned} \tag{1.46}$$

which is equivalent to that

$$\frac{\dot{a}_{ij}(t)}{a_{ij}(t)} = i(\chi_j - \chi_i)\alpha_i(t)\alpha_j^*(t). \tag{1.47}$$

Up till now, we have obtained the time-evolved full density matrix as

$$\rho(t) = \sum_{i,j} c_{ij}(t)|i\rangle\langle j| \otimes |\alpha_i(t)\rangle\langle\alpha_j(t)|, \tag{1.48}$$

with the coefficients being

$$c_{ij}(t) = \frac{a_{ij}(t)}{\langle\alpha_j(t)|\alpha_i(t)\rangle}, \quad a_{ij} = \exp\Big\{\Big(i(\chi_j - \chi_i)\int_0^t \alpha_i(t')\alpha_j^*(t')dt'\Big)\Big\}. \tag{1.49}$$

Notice that for $i = j$, which denotes a diagonal term in the density matrix, $c_{ij}(t) \equiv 1$, meaning that the state population undergoes no relaxation for this channel. For longer time where $\kappa t \gg 1$, the cavity reaches equilibrium state for each qudit state,

$$\alpha_i^s = \frac{-\epsilon}{\chi_i + \Delta - \frac{\kappa}{2}i}. \tag{1.50}$$

In this limit, the qudit get dephased between state $|i\rangle$ and state $|j\rangle$ by the measurement process, with rate $\Gamma_m^{ij} = (\chi_j - \chi_i)\,\mathrm{Im}(\alpha_i^s\alpha_j^{s*}) = D_s^{ij}\kappa/2$, where $D_s^{ij} = |\alpha_i^s - \alpha_j^s|^2$ measures the distinguishability of the cavity states $|\alpha_i^s\rangle$ and $|\alpha_j^s\rangle$. Thus, for such measurement induced dephasing, the Lindbladian in corresponding rotating frame is

$$\dot{\rho} = \mathcal{L}\rho = \frac{\kappa}{2}\mathcal{D}[\hat{A}]\rho + \frac{\kappa}{2}\mathcal{D}[\hat{A}^\dagger]\rho, \tag{1.51}$$

where the jump operator $\hat{A} = \sum_i \alpha_i^s|i\rangle\langle i|$.

In Section **??**, we consider the partial measurement scheme as is shown in Fig. 2.2 (b) and (c). For paritial measurement on state $|k\rangle$, we require that $|\chi_i - \chi_k| \gg \kappa$ for any $i \neq k$, and also we tune the cavity probe to be exactly on resonance with the shifted cavity frequency for state $|k\rangle$, $\Delta = -\chi_k$. Thus, the steady state cavity response for state $|k\rangle$ is $\alpha_k^s = -2\epsilon i/\kappa$, while for other states $|i \neq k\rangle$ the cavity response is approximately $\alpha_i^s \simeq -\epsilon/(\chi_i - \chi_k)$ as $|\chi_i - \chi_k|/\kappa \to \infty$. In this case, the measurement-induced dephasing rates between state $|k\rangle$

and other states are $\Gamma_m^{ik} \simeq 2\epsilon^2/\kappa$, which is a finite value, while the dephasing rates between two other states are $\Gamma_m^{ij} \simeq 0$. By such arragement of cavity parameters and cavity probes, we are able to only selectively dephase one state while keeping the coherence between all the other states, demonstrating a partial measurement. For such partial measurement process, the Lindbladian in corresponding rotating frame is

$$\dot{\rho} = \mathcal{L}\rho = \frac{\kappa}{2}\mathcal{D}[\hat{A}]\rho + \frac{\kappa}{2}\mathcal{D}[\hat{A}^\dagger]\rho, \tag{1.52}$$

where the jump operator can be set to $\hat{A} = |\alpha_k^s||k\rangle\langle k|$.

Chapter 2

Decoherence induced geometric phase

2.1 The geometric phase

As was systematically pointed out by Berry [16], the overall phase of a quantum system accumulates under an adiabatic evolution. This accumulated phase factor is additional to the phase accumulation due to the dynamics of the Hamiltonian itself, dependent on the geometric feature of the evolution path in parameter space. While adding an overall phase to a quantum system does not change the expectation values of a local observable, we are still able to observe this phase factor via interference with another quantum system undergoing a different path [17].

Consider an adiabatic evolution of the Hamiltonian dependent on a vector in parameter space, $\hat{H}(\vec{R}(t))$, the system state $|\psi(t)\rangle$ evolves as,

$$\hat{H}(\vec{R}(t))|\psi(t)\rangle = i\hbar|\dot{\psi}(t)\rangle. \tag{2.1}$$

With the Hamiltonian changing with time slowly enough, the system starting from an eigenstate, $|\psi(0)\rangle = |n(\vec{R}(0))\rangle$, of the Hamiltonian, $\hat{H}(\vec{R}(0))$, will stay in the eigenstate, $|\psi(t)\rangle = |n(\vec{R}(t))\rangle$, of the Hamiltonian, $\hat{H}(\vec{R}(t))$, assuming that no crossing happens between any two energy levels. Such evolution gives us that

$$\hat{H}(\vec{R}(t))|n(\vec{R}(t))\rangle = E_n(\vec{R}(t))|n(\vec{R}(t))\rangle, \tag{2.2}$$

and thus the expression for the system state as,

$$|\psi(t)\rangle = \exp\left\{\frac{-i}{\hbar}\int_0^t dt' E_n(\vec{R}(t'))\right\}\exp(i\gamma_n(t))|n(\vec{R}(t))\rangle. \tag{2.3}$$

Plugging Eqn. 2.3 into Eqn. 2.1, we have

$$\begin{aligned} \hat{H}(\vec{R}(t))|\psi(t)\rangle &= E_n(\vec{R}(t))\exp\left\{\frac{-i}{\hbar}\int_0^t dt' E_n(\vec{R}(t'))\right\}\exp(i\gamma_n(t))|n(\vec{R}(t))\rangle, \\ i\hbar|\dot{\psi}(t)\rangle &= i\hbar\frac{-i}{\hbar}E_n(\vec{R}(t))\exp\left\{\frac{-i}{\hbar}\int_0^t dt' E_n(\vec{R}(t'))\right\}\exp(i\gamma_n(t))|n(\vec{R}(t))\rangle \\ &\quad + i\hbar i\dot{\gamma}_n(t)\exp\left\{\frac{-i}{\hbar}\int_0^t dt' E_n(\vec{R}(t'))\right\}\exp(i\gamma_n(t))|n(\vec{R}(t))\rangle \\ &\quad + i\hbar\exp\left\{\frac{-i}{\hbar}\int_0^t dt' E_n(\vec{R}(t'))\right\}\exp(i\gamma_n(t))|\dot{n}(\vec{R}(t))\rangle, \end{aligned} \tag{2.4}$$

and thus

$$\dot{\gamma}_n(t) = i\langle n(\vec{R}(t))|\dot{n}(\vec{R}(t))\rangle = i\langle n(\vec{R}(t))|\vec{\nabla}_{\vec{R}} n(\vec{R}(t))\rangle \cdot \dot{\vec{R}}(t), \tag{2.5}$$

which finally gives us the accumulated geometric phase as

$$\gamma_n(\mathcal{C}) = i\oint_{\mathcal{C}} \langle n(\vec{R})|\vec{\nabla}_{\vec{R}} n(\vec{R})\rangle \cdot d\vec{R} = \oint_{\mathcal{C}} \vec{\mathcal{A}}_n(\vec{R}) \cdot d\vec{R}, \tag{2.6}$$

when the parameter vector $\vec{R}$ evolves around a closed path $\mathcal{C}$ with $\vec{R}(T) = \vec{R}(0)$ in time period T. Here we got the definition of Berry connection (Berry potential) as,

$$\vec{\mathcal{A}}_n(\vec{R}) = i\langle n(\vec{R})|\vec{\nabla}_{\vec{R}} n(\vec{R})\rangle. \tag{2.7}$$

When the parameter space is three-dimensional, with Stokes' theorem, such integral over a closed path $\mathcal{C}$ with a encircled surface $\mathcal{S}$ can be written as,

$$\gamma_n(\mathcal{C}) = \oint_{\mathcal{C}} \vec{\mathcal{A}}_n(\vec{R}) \cdot d\vec{R} = \int_{\mathcal{S}} \left[\vec{\nabla}_{\vec{R}} \times \vec{\mathcal{A}}_n(\vec{R})\right] \cdot d\vec{S} = \int_{\mathcal{S}} \vec{\Omega}_n(\vec{R}) \cdot d\vec{S}. \tag{2.8}$$

This gives the definition of Berry curvature in three-dimensional parameter space, $\vec{\Omega}_n(\vec{R}) =$

$\vec{\nabla}_{\vec{R}} \times \vec{\mathcal{A}}_n(\vec{R})$. In higher dimensional case, similarly, the Berry curvature is defined as a 2-form,

$$\Omega_{n,\mu\nu}(\vec{R}) = \frac{\partial \mathcal{A}_{n,\nu}(\vec{R})}{\partial R^{\mu}} - \frac{\partial \mathcal{A}_{n,\mu}(\vec{R})}{\partial R^{\nu}}. \tag{2.9}$$

2.2 Measurement induced geometric phase

The first findings about measurement-induced geometric phase was decades ago before Berry's work on adiabaticity-induced geometric phase, when Pancharatnam pointed out in 1956 [17] that in optical systems, measurement could result in phase difference in the interference of polarized light beams. In such cases with a sequence of projective measurements $\{P_k\}$ on a sequence of states $\{|\psi_k\rangle\}$ with all-positive outcomes, the resulting quantum state can be written as

$$|\tilde{\psi}_N\rangle = P_N ... P_2 P_1 |\psi_0\rangle, \quad P_k = |\psi_k\rangle\langle\psi_k|, \tag{2.10}$$

up to normalization. The accumulated geometric phase for a pair of states, $|\psi_j\rangle$ and $|\psi_k\rangle$, can be defined as $\chi(|\psi_j\rangle, |\psi_k\rangle) = \arg[\langle\psi_j|\psi_k\rangle]$. Then the total geometric phase accumulated in the measurement sequence is

$$\chi^{(P)}_{\text{geom}} = \arg[\langle\psi_0|\tilde{\psi}_N\rangle] = \arg[\langle\psi_0|P_N ... P_2 P_1|\psi_0\rangle]. \tag{2.11}$$

Such Pancharatnam phase induced by projective measurements can be related to Berry's adiabatic geometric phase in a way that, the Pancharatnam phase is equal to the Berry phase accumulated along the shortest geodesics connecting each measurement point in Hilbert space [18]. Here we consider a sequence of measurements with a more general form, which are described by weak measurements, $\{M_k^{(r_k)}\}$, for the k_{th} measurement with corresponding outcome r_k. For a particular string of measurement results, $\{r_k\}$, the induced geometric

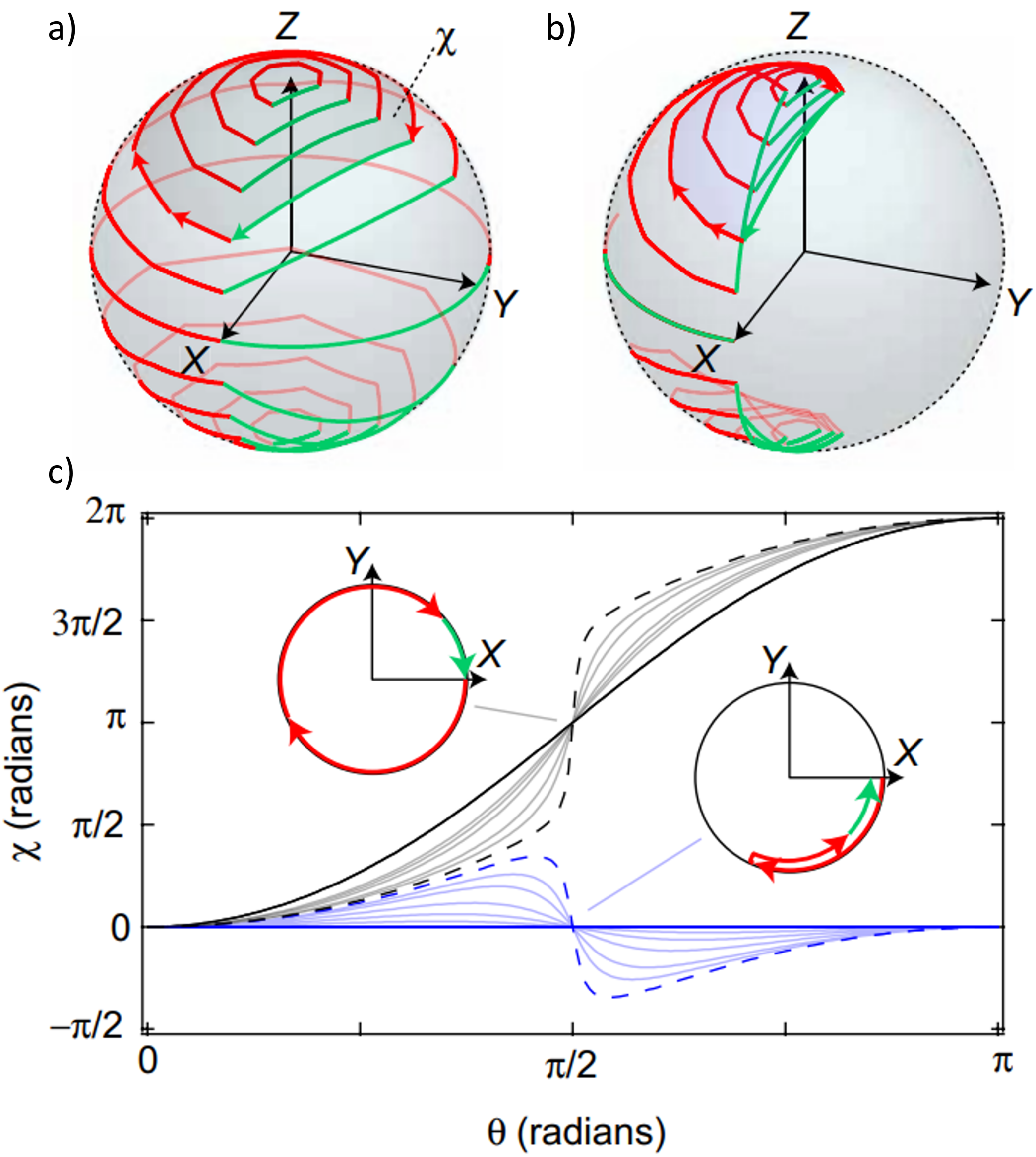

Fig. 2.1: Measurement induced topological transition in geometric phases. (a) A sequence of measurements along a fixed latitude drags the state on a trajectory displayed on the Bloch sphere surface (red line and arrow). When a final projective measurement closes the path (green arrow), the state acquires a geometric phase (χ). Considering all latitudes, these trajectories form a closed surface winding around the Bloch sphere. (b) Weaker measurements result in smaller back action on the state. The trajectories thus form a closed surface that does not wrap around the Bloch sphere. (c) Dependence of the geometric phase on the polar angle θ for the measurement sequences with measurement strengths slightly below (blue dashed line) and above (black dashed line) the critical value. The black solid line shows the case of infinitely strong measurements and the blue solid line represents zero measurement strength, and faint lines indicate intermediate measurement strengths. The insets illustrate the origin of the transition.

phase can be written as

$$\chi_{\text{geom}}^{(M)} = \arg[\langle\psi_0|\tilde{\psi}_N\rangle] = \arg[\langle\psi_0|M_N^{(r_N)}...M_k^{(r_k)}...M_2^{(r_2)}M_1^{(r_1)}|\psi_0\rangle]. \tag{2.12}$$

Now we consider the measurement sequences happening in a two-level system on the Bloch sphere, which is specified by state $|+\rangle$ and $|-\rangle$. Assume that the unitary rotation operator U_k connects between $|\psi_k\rangle$ and $|+\rangle$ with $|\psi_k\rangle = U_k|+\rangle$, where $|+\rangle$ is along the z axis of the Bloch sphere. Then the measurement $M_k^{(r_k)}$ can be viewed as being along state $|\psi_k\rangle$ if $M_k^{(r_k)} = U_k M_z^{(r_k)} U_k^\dagger$, with $M_z^{(r_k)}$ being a weak measurement along the z axis of the Bloch sphere with outcome r_k. As an example, we could consider a model of measurement where $r_k \in \{+,-\}$ with $M_z^{(+)} = |+\rangle\langle+| + \sqrt{1-\eta}|-\rangle\langle-|$ and $M_z^{(-)} = \sqrt{\eta}|-\rangle\langle-|$. Here the measurement strength is characterized by η. When $\eta = 0$, the weak measurement has no impact on the system and the outcome is always $+$. When $\eta = 1$, the weak measurement becomes projective that $M_z^{(+)} = |+\rangle\langle+|$ and $M_z^{(-)} = |-\rangle\langle-|$.

By such definition, we could consider a sequence of weak measurements, $\{M_k^{(r_k)}\}$, along states $|\psi_k\rangle$ specified by (θ, ϕ_k) on the Bloch sphere. Here ϕ_k distributes evenly between $[0, 2\pi]$ defining a measurement sequence around the Bloch sphere along the latitude with polar angle θ. We also consider the system state after the k_{th} measurement as $|\tilde{\psi}_k\rangle = M_k^{(r_k)}...M_2^{(r_2)}M_1^{(r_1)}|\psi_0\rangle$, which is specified by $(\Theta_k(\theta,\phi_k), \Phi_k(\theta,\phi_k))$ on the Bloch sphere with accumulated phase $\alpha(\theta,\phi_k)$. Notice that Φ_k does not necessarily keeps constant like ϕ does, since only the latitude of $\theta = \pi/2$ is also along a geodesic line. We then consider the quasi-continuous limit of measurements, where an infinite number of measurements are performed with ϕ_k being close to each other with infinite small separations. In that case, we could map (θ,ϕ) towards (Θ,Φ) from the Bloch sphere surface to a surface formed by measurement-induced trajectories under postselection. As is studied by Gebhart et. al. [19], the Chern number can be considered by integration of the Berry curvature over the entire surface in the parameter space, where

$$\mathcal{C} \equiv \frac{1}{2\pi}\int_0^{\pi} d\theta \int_0^{2\pi} dt\tilde{B}(\theta,t) = \frac{1}{2\pi}(\chi_{\mathrm{geom}}(\pi) - \chi_{\mathrm{geom}}(0)) \in \{0,-1\}. \tag{2.13}$$

Here, such integral of the Berry curvature is equal to the difference between geometric phases accumulated along latitude $\theta = 0$ and latitude $\theta = \pi$, which is bounded to be multiples of 2π. This results in discrete values of the Chern number, which is of topological differences and thus robust against perturbations in the system parameters. Due to system symmetry such that $\chi_{\mathrm{geom}}(\pi-\theta) = -\chi_{\mathrm{geom}}(\theta)$, we obtain that $\chi_{\mathrm{geom}}(\pi/2) = (\chi_{\mathrm{geom}}(0) + \chi_{\mathrm{geom}}(\pi))/2 = \pi\mathcal{C} \in \{0, -\pi\}$. Here, the topological feature of the system is directly related to the geometric phase accumulated around the equator, which lies between two discrete values in the strong measurement limit and the weak measurement limit. Such behaviour indicates an abrupt transition of the topological feature at a critical value of measurement strength.

In the experimental realization presented in Section 2.3, we approach the above quasi-continuous limit where six discrete weak measurements are performed along with an additional final projective measurement. The above measurements are performed along a certain latitude with polar angle θ, on points with evenly separated azimuthal angles, ϕ. As is shown in Fig. 2.1, the topological behaviour is still clearly shown for the discrete and experimentally realizable measurement sequences. The values of the geometric phase χ for $\theta = 0$ and $\theta = \pi$ must differ by a multiple of 2π. This difference cannot be changed by continuous deformation of the dependence of χ on θ. Thus the behaviors above and below the transition are topologically distinct. The insets illustrate the origin of the transition. For sufficiently strong measurements the equatorial trajectory circumnavigates the Bloch sphere while for weak measurements it does not.

2.3 Experimental realizations

2.3.1 Partial measurements in dispersive limit

Here we consider a superconducting transmon qudit dispersively coupled to a linear cavity, which is shown in Fig. 2.2(a). This means that for the coupling strength g and cavity-qubit detuning Δ, we have the condition $g^2/\Delta \ll 1$. From the derivation in Section 1.3, we have the effective Hamiltonian as,

$$\mathrm{H}_{\text{eff}} = \hbar\omega_r a^\dagger a + \sum_j \hbar\omega_j |j\rangle\langle j| + \sum_j \hbar\xi_j |j\rangle\langle j| a^\dagger a. \tag{2.14}$$

Here $a^\dagger(a)$ is the cavity photon number operator, $\hbar\omega_j$ represents the transmon energy on energy eigenstate $|j\rangle$, and $\hbar\xi_j$ is the interaction energy between the cavity eigenstate and transmon energy level $|j\rangle$. The effect brought by such interaction energy ξ_j can be viewed as a qutrit-state-dependent shift on the cavity frequency, enabling quantum non-demolition weak measurements of the circuit energy states. As is shown in Fig. 2.2(b), with the cavity probed by a coherent state, the output signal distributes on the quadrature space of the electromagnetic field depending on the cavity transmission at the measurement frequency.

Assuming that the system starts from an unentangled density matrix $\hat{\rho} = \hat{\rho}_q \otimes \hat{\rho}_b = \sum_{i,j} \rho_{ij} |i\rangle\langle j| \otimes \hat{\rho}_b$, the qudit state gets entangled with the field leaking outside of the cavity as $\hat{\rho} = \sum_{i,j} \rho_{ij} |i\rangle\langle j| \otimes |\alpha_i\rangle\langle\alpha_j|$, which is in consistency with the evolution discussed in Section 1.5. For signal processing with the Josephson amplifier working as a linear phase-preserving amplifier, the input-output relation shows [20],

$$\hat{a}_m = \frac{1}{\sqrt{G}} \hat{a}_{Sig}^{out} = \hat{a}_{Sig}^{in} + i\frac{\sqrt{G-1}}{\sqrt{G}} \hat{a}_{Idl}^{in\,\dagger} \simeq \hat{a}_{Sig}^{in} + i\hat{a}_{Idl}^{in\,\dagger} \tag{2.15}$$

in the limit $G \gg 1$, with $\hat{I}_m/\sigma_0 = \hat{a}_m + \hat{a}_m^\dagger$, $i\hat{Q}_m/\sigma_0 = \hat{a}_m - \hat{a}_m^\dagger$, and σ_0 being the variance of each field quadrature. Here, we have the the commutation relation with $[I_m, Q_m] = 0$, as well as eigenstate relations with $\hat{a}_{Sig}^{in}|\alpha_i\rangle = \alpha_i|\alpha_i\rangle$, $\hat{a}_{Idl}^{in}|\alpha_i\rangle = 0|\alpha_i\rangle$, and $\hat{I}_m|I_m, Q_m\rangle =$

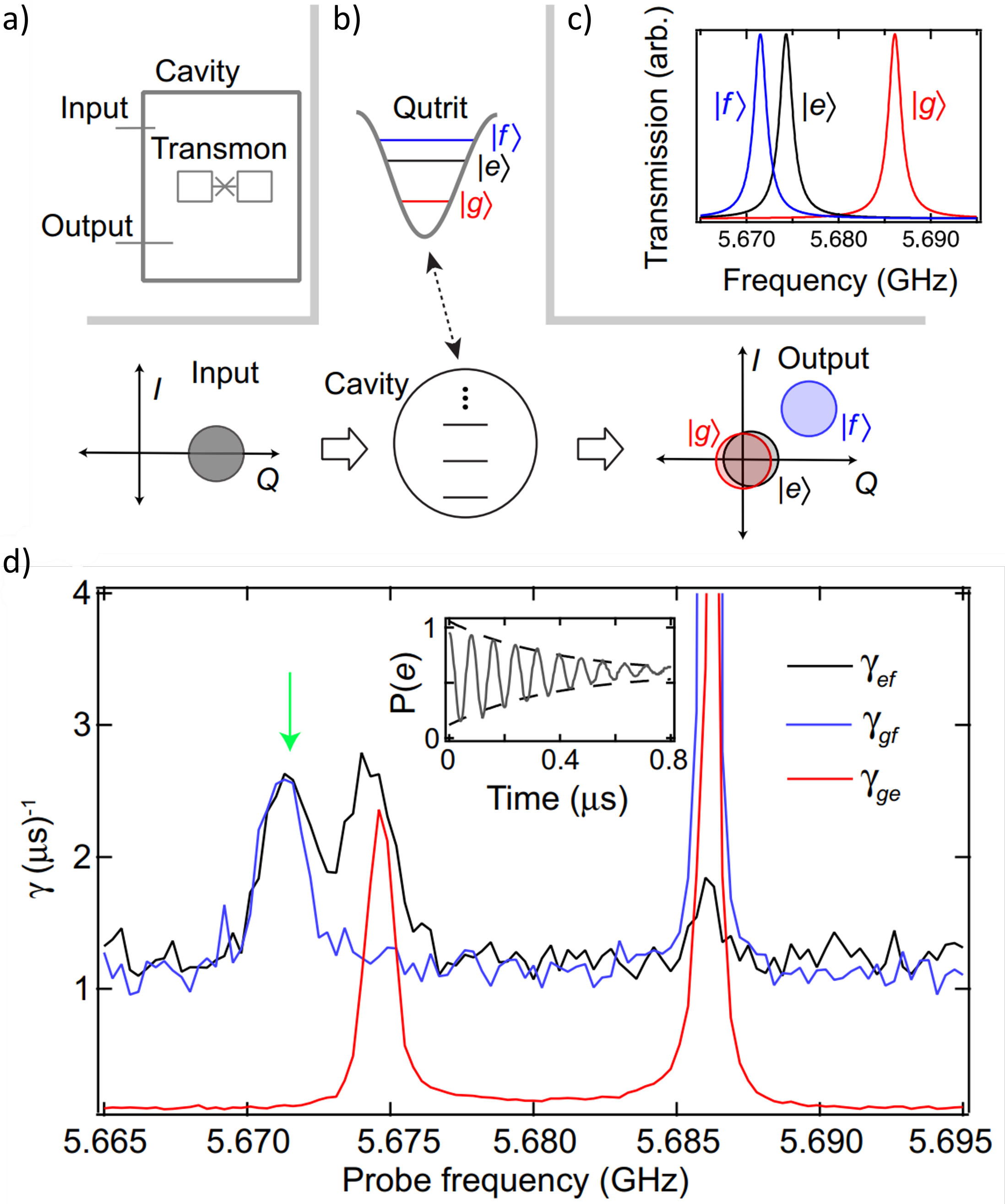

Fig. 2.2: **Experimental realization of partial measurement** (a) A superconducting transmon qubit and a dissipative linear cavity are dispersively coupled. The cavity shift dependent on the qubit, ξ, is much larger than the cavity linewidth, κ. (b) When coherently driven, the caivty response acquires qutrit-state-dependent displacements on the I/Q plane. (c) The cavity transmission is dependent on the qubit state due to the dispersive interaction. Probing the cavity at the resonance frequency for one state leads to partial measurement of the state. (d) For fixed strength of cavity probe, we depict the dephasing rate between each two levels vs. frequency of the cavity probe. Inset shows a typical Ramsey measurement pattern. The green arrow marks the chosen frequency for the applied cavity probe.

$I_m|I_m, Q_m\rangle$, $\hat{Q}_m|I_m, Q_m\rangle = Q_m|I_m, Q_m\rangle$. From the relation between the operators, we could calculate the overlap between a coherent state $|\alpha_i\rangle$ and $|I_m, Q_m\rangle$ as [20]

$$\langle I_m, Q_m|\alpha_i\rangle = \xi_{\alpha_i}(I_m, Q_m) = \frac{1}{\sqrt{\pi}}\frac{1}{2\sigma_0}\exp\left(-\frac{(I_m - \bar{I}_m^{(i)})^2 + (Q_m - \bar{Q}_m^{(i)})^2}{2(2\sigma_0)^2}\right), \tag{2.16}$$

with $\alpha_i = \bar{I}_m^{(i)} + i\bar{Q}_m^{(i)}$. When the measurement outcome is (I_m, Q_m), a projective measurement is applied onto state $|I_m, Q_m\rangle$. Then the system density matrix, $\hat{\rho}$ becomes

$$\frac{M_b(I_m, Q_m)\hat{\rho}M_b^\dagger(I_m, Q_m)}{\mathrm{Tr}\left(M_b(I_m, Q_m)\hat{\rho}M_b^\dagger(I_m, Q_m)\right)} = \frac{\sum_{i,j}\rho_{i,j}\xi_{\alpha_i}(I_m, Q_m)\xi^*_{\alpha_j}(I_m, Q_m)|i\rangle\langle j|}{\mathrm{Tr}\left(\sum_{i,j}\rho_{i,j}\xi_{\alpha_i}(I_m, Q_m)\xi^*_{\alpha_j}(I_m, Q_m)|i\rangle\langle j|\right)}\otimes|I_m, Q_m\rangle\langle I_m, Q_m| \tag{2.17}$$

after the measurement process, with $M_b(I_m, Q_m)$ being the projective operator on the field, $M_b(I_m, Q_m) = |I_m, Q_m\rangle\langle I_m, Q_m|$. Tracing out the outside field, we have the qudit density matrix

$$\hat{\rho}_q = \rho_{ij}|i\rangle\langle j| \rightarrow \frac{\sum_{i,j}\rho_{i,j}\xi_{\alpha_i}(I_m, Q_m)\xi^*_{\alpha_j}(I_m, Q_m)|i\rangle\langle j|}{\mathrm{Tr}\left(\sum_{i,j}\rho_{i,j}\xi_{\alpha_i}(I_m, Q_m)\xi^*_{\alpha_j}(I_m, Q_m)|i\rangle\langle j|\right)} = \frac{M(I_m, Q_m)\hat{\rho}_q M^\dagger(I_m, Q_m)}{\mathrm{Tr}\left(M(I_m, Q_m)\hat{\rho}_q M^\dagger(I_m, Q_m)\right)}. \tag{2.18}$$

Here, the Kraus operator acting on the qudit system is

$$M(I_m, Q_m) = \sum_i \xi_{\alpha_i}(I_m, Q_m)|i\rangle\langle i| = \frac{1}{\sqrt{\pi}}\frac{1}{\sigma}\sum_i e^{-\frac{(\vec{r}-\vec{r}_i)^2}{2\sigma^2}}|i\rangle\langle i| \tag{2.19}$$

Here $\vec{r}$ represents the output signal's location on the I/Q plane, (I_m, Q_m), $\vec{r}_i$ is the mean output signal when the transmon is in the energy eigenstate $|i\rangle$, $(\bar{I}_m^{(i)}, \bar{Q}_m^{(i)})$, and $\sigma = 2\sigma_0$ is the total variance of the signal in both quadratures.

Considering the lowest three energy levels, $j \in \{g, e, f\}$, the Kraus operators can be written explicitly as,

$$M_z^{(\vec{r})} = \sqrt{\frac{1}{\pi}\frac{1}{\sigma}} \begin{pmatrix} e^{-(\vec{r}-\vec{r}_f)^2/2\sigma^2} & 0 & 0 \\ 0 & e^{-(\vec{r}-\vec{r}_e)^2/2\sigma^2} & 0 \\ 0 & 0 & e^{-(\vec{r}-\vec{r}_g)^2/2\sigma^2} \end{pmatrix} \tag{2.20}$$

in energy eigenstate basis. Here $\vec{r}_g$, $\vec{r}_e$ and $\vec{r}_f$ are the mean output signal when the transmon is in the energy eigenstates $|g\rangle$, $|e\rangle$ and $|f\rangle$.

2.3.2 Partial measurements in strong dispersive regime

The setup [21] is operated in the strong dispersive regime, where the cavity linewidth $\kappa \ll \xi_j$. Fig. 2.2(b) and (c) present that a weak probe of the cavity near the $|f\rangle$ resonance will be transmitted only if the circuit is in the $|f\rangle$ state, which means that $\vec{r}_g \approx \vec{r}_e \approx 0$ while $\vec{r}_f = \vec{r}_0$ is a finite value. In the limit $\xi \gg \kappa$ the Kraus operators associated with a probe near the $|f\rangle$ resonance in Equation 2.20 become

$$M_z^{(\vec{r})} = \sqrt{\frac{1}{\pi}\frac{1}{\sigma}} \begin{pmatrix} e^{-(\vec{r}-\vec{r}_0)^2/2\sigma^2} & 0 & 0 \\ 0 & e^{-\vec{r}^2/2\sigma^2} & 0 \\ 0 & 0 & e^{-\vec{r}^2/2\sigma^2} \end{pmatrix}. \tag{2.21}$$

Such measurement distinguishes the state $|f\rangle$ from both $|e\rangle$ and $|g\rangle$, but does not distinguish $|e\rangle$ from $|g\rangle$. The selective nature of this measurement architecture allows us to reserve one energy level (e.g. $|g\rangle$) as a quantum phase reference in order to determine the global phase accumulated by a state in the $\{|e\rangle, |f\rangle\}$ manifold. Applying such a measurement pulse ideally gives us dephasing between each two states $\gamma_{ef}t = \gamma_{gf}t = \frac{\vec{r}_0^2}{4\sigma^2}$ and $\gamma_{ge}t = 0$.

We characterize the strength and selectivity of the measurement by examining the dephasing rates of each pair of states, which is explained in detail in Section 1.5. We drive the cavity with a weak probe, and perform Ramsey measurement on each pair of levels to determine the dephasing rates $\gamma_{ge}, \gamma_{ef}, \gamma_{gf}$. In Figure 2.2(d) we display these measured dephasing rates versus probe frequency. The data show enhanced dephasing at each qutrit-state-dressed cavity resonance, as expected. We further observe larger background dephasing on the $|f\rangle$ state which is due to the reduced charge noise insensitivity of the higher transmon levels [3]. A cavity probe frequency $\omega_{\mathrm{p}}/2\pi = 5.6715$ GHz therefore allows us to realize measurements on the $\{|e\rangle, |f\rangle\}$ manifold, while preserving coherence within the $\{|g\rangle, |e\rangle\}$ manifold. The measurement strength can be tuned via the duration of the measurement for the constant weak probe. Providing enough amount of dephasing for strong measurements via long waiting time, the probe itself is weak enough so that the averaged photon number in the cavity, $\bar{n}$, is below 1. Although number splitting typically happens in the strong dispersive regime [15], shifting the qubit transition energy by $\bar{n}\xi$, we can still drive efficient two-level rotations with Rabi drive that $\Omega \gg \xi$ in the existence of the probe. Thus, such measurement probe can be always-on and serves as a background, with neglectable influences on the coherent rotation pulses we apply.

2.3.3 Designed pulse sequences

With the partial measurements descriminating only state $|f\rangle$ from other states, we can now design experimental pulse sequences. We consider a two-level system consisting the second and the third energy level of a qutrit. This two-level system undergoes measurements and gains the geometric phase factor, with basis $|e\rangle$ and $|f\rangle$. The ground state the system, $|g\rangle$, is utilized here to extract the geometric phase by interference. The partial measurement, not separating the cavity response from state $|g\rangle$ and state $|e\rangle$, keeps coherence between the third level and the measured two-level system.

In that case, since all measurements are in the energy eigenstates, they happen along the z axis of the Bloch sphere defined by the two basis $|e\rangle$ and $|f\rangle$. However, to observe the topological transition as is described in Section **??**, we have to make a sequence of measurements around the Bloch sphere at an arbitrary latitude. As is shown in Fig. 2.3 (a), we utilize two rotation pulses to perform such a measurement process along an arbitrary axis. Assuming that the measurement direction is along $|\vec{n}\rangle$ on the Bloch sphere, then the corresponding Kraus operator for measurement result $\vec{r}$ is $M_{\vec{n}}^{(\vec{r})} = \Psi(\vec{r})|\vec{n}\rangle\langle\vec{n}|+\tilde{\Psi}(\vec{r})|-\vec{n}\rangle\langle-\vec{n}|$. The rotation operator is chosen so that $R_{\vec{n}}^{\dagger}|e\rangle = |\vec{n}\rangle$. Then, for the measurement along the z axis, $M_0^{(\vec{r})} = \Psi(\vec{r})|e\rangle\langle e| + \tilde{\Psi}(\vec{r})|f\rangle\langle f|$, we have $M_{\vec{n}}^{(\vec{r})} = R_{\vec{n}}^{\dagger}M_0^{(\vec{r})}R_{\vec{n}}$. For $|\vec{n}\rangle$ represented by $|\theta,\phi\rangle$ on the Bloch sphere, we note $R_{\vec{n}}^{\dagger}$ as $R_{ef,\phi}^{\theta}$, $R_{\vec{n}}$ as $R_{ef,\phi}^{-\theta}$, the three-level measurement operator along the z axis as M_z, and the measurement operator along $|\theta,\phi\rangle$ axis as $M_{\theta,\phi}$ in Fig. 2.3 (b).

We assume that the initial qutrit state is denoted by $|\phi_i\rangle$ and the final state after the measurement sequence is $|\phi_f\rangle$. Here we start with a superposition between the reference state and the measured two-level system, $|\phi_i\rangle = a_i^{(e)}|e\rangle + a_i^{(g)}|g\rangle$. As is shown in Fig. 2.3 (b), such initial state is prepared by a $\pi/2$ Rabi pulse between state $|g\rangle$ and state $|e\rangle$. Then, the rotation pulse between state $|e\rangle$ and state $|f\rangle$, $R_{ef,\phi=0}^{\theta}$, takes the two-level subspace onto the chosen latitude, θ. After that, N weak measurements around the Bloch sphere are carried out, which is concluded with a projective measurement along the axis of $|\theta,\phi=0\rangle$, with the Kraus operator $P_{\vec{n}}^{+} = P_{\phi=0}^{\theta}$. Finally we rotate the state from latitude θ back to state $|e\rangle$, in order to bring it into interference with the reference state, $|g\rangle$. This entire process gives us

$$\begin{aligned}
|\phi_f\rangle &= R_0 P_{\vec{n}}^{+}\prod_{n=1}^{N} M_{\theta,\phi=-2\pi in/(N+1)} R_0^{\dagger}|\phi_i\rangle \\
&= R_{ef,\phi=0}^{-\theta}(R_{ef,\phi=0}^{\theta}P_{ge}R_{ef,\phi=0}^{-\theta})\prod_{n=1}^{N}(R_{ef,\phi=-2\pi in/(N+1)}^{\theta}M_z R_{ef,\phi=-2\pi in/(N+1)}^{-\theta})R_{ef,\phi=0}^{\theta}|\phi_i\rangle \qquad (2.22)\\
&= P_{ge}R_{ef,\phi=0}^{-\theta}\prod_{n=1}^{N}(R_{ef,\phi=-2\pi in/(N+1)}^{\theta}M_z R_{ef,\phi=-2\pi in/(N+1)}^{-\theta})R_{ef,\phi=0}^{\theta}|\phi_i\rangle.
\end{aligned}$$

Here P_{ge} is the projective measurement on subspace $\{|g\rangle,|e\rangle\}$. With $|\phi_f\rangle = a_i^{(e)}e^{i\chi}|e\rangle+a_i^{(g)}|g\rangle$, the Ramsey-like pulses between $|g\rangle$ and $|e\rangle$ create interference patterns which is shown in Fig. 2.3 (c). The phase of the interference pattern measures the accumulated phase χ for the subspace $\{|e\rangle,|f\rangle\}$ and the amplitude of the pattern measures the contrast of the geometric phase extracted from an ensemble after the measurement. In the experiment, we chose $N = 6$ as a reasonable number of weak measurements.

For carrying out such rotation pulses, we apply a Rabi drive near the qubit resonance frequency to the cavity, which is dispersively coupled to the qubit. With rotating wave approximation, the system Hamiltonian is,

$$\begin{aligned}
&\hat{H} = \hat{H}_0 + \hat{V}, \\
&\hat{H}_0 = \hbar\frac{\omega_q}{2}\hat{\sigma}_z + \hbar\omega_c\hat{a}^\dagger\hat{a} + \hbar\epsilon_r(e^{-i(\omega_r t+\alpha)}\hat{a}^\dagger + e^{i(\omega_r t+\alpha)}\hat{a}), \\
&\hat{V} = \hbar g(\hat{\sigma}_-\hat{a}^\dagger + \hat{\sigma}_+\hat{a}).
\end{aligned} \tag{2.23}$$

Here $\hbar\omega_c$ and $\hbar\omega_q$ are the cavity and qubit energy splittings, ϵ_r and ω_r are the amplitude and frequency of the Rabi drive on the cavity, and g is the coupling strength between the qubit and the cavity. As is introduced in section 1.3, in the dispersive limit, the detuning between the qubit and the cavity is much larger than the coupling strength. Performing the Schrieffer-Wolff transformation, we have $\hat{H}_{\text{eff}} = e^{-\hat{S}}\hat{H}e^{\hat{S}}$, with

$$\hat{S} = \lambda(\hat{\sigma}_+\hat{a} - \hat{\sigma}_-\hat{a}^\dagger), \tag{2.24}$$

where $\lambda = g/(\omega_q - \omega_c)$. From

$$[\hat{a}, \hat{a}^\dagger\hat{a}] = \hat{a},\ [\hat{a}^\dagger, \hat{a}^\dagger\hat{a}] = -\hat{a}^\dagger,\ [\hat{\sigma}_-, \hat{\sigma}_z] = 2\hat{\sigma}_-,\ [\hat{\sigma}_+, \hat{\sigma}_z] = -2\hat{\sigma}_+, \tag{2.25}$$

we can have

$$[\hat{S}, \hat{H}_0] = \hbar\lambda(\omega_c - \omega_q)(\hat{\sigma}_-\hat{a}^\dagger + \hat{\sigma}_+\hat{a}) + \hbar\epsilon_r\lambda(e^{i(\omega_r t+\alpha)}\hat{\sigma}_- + e^{-i(\omega_r t+\alpha)}\hat{\sigma}_+), \tag{2.26}$$

giving the relation $[\hat{S}, \hat{H}_0] + \hat{V} = O(\lambda)$. The Baker-Campbell-Hausdorff relation reveals $\hat{H}_{\text{eff}} = \hat{H}_0 + \hat{V} + [\hat{S}, \hat{H}_0] + [\hat{S}, \hat{V}] + \frac{1}{2}[\hat{S}, [\hat{S}, \hat{H}_0]] + \frac{1}{2}[\hat{S}, [\hat{S}, \hat{V}]] + \ldots$. Thus, $\hat{H}_{\text{eff}} = \hat{H}_0 + [\hat{S}, \hat{H}_0] +$

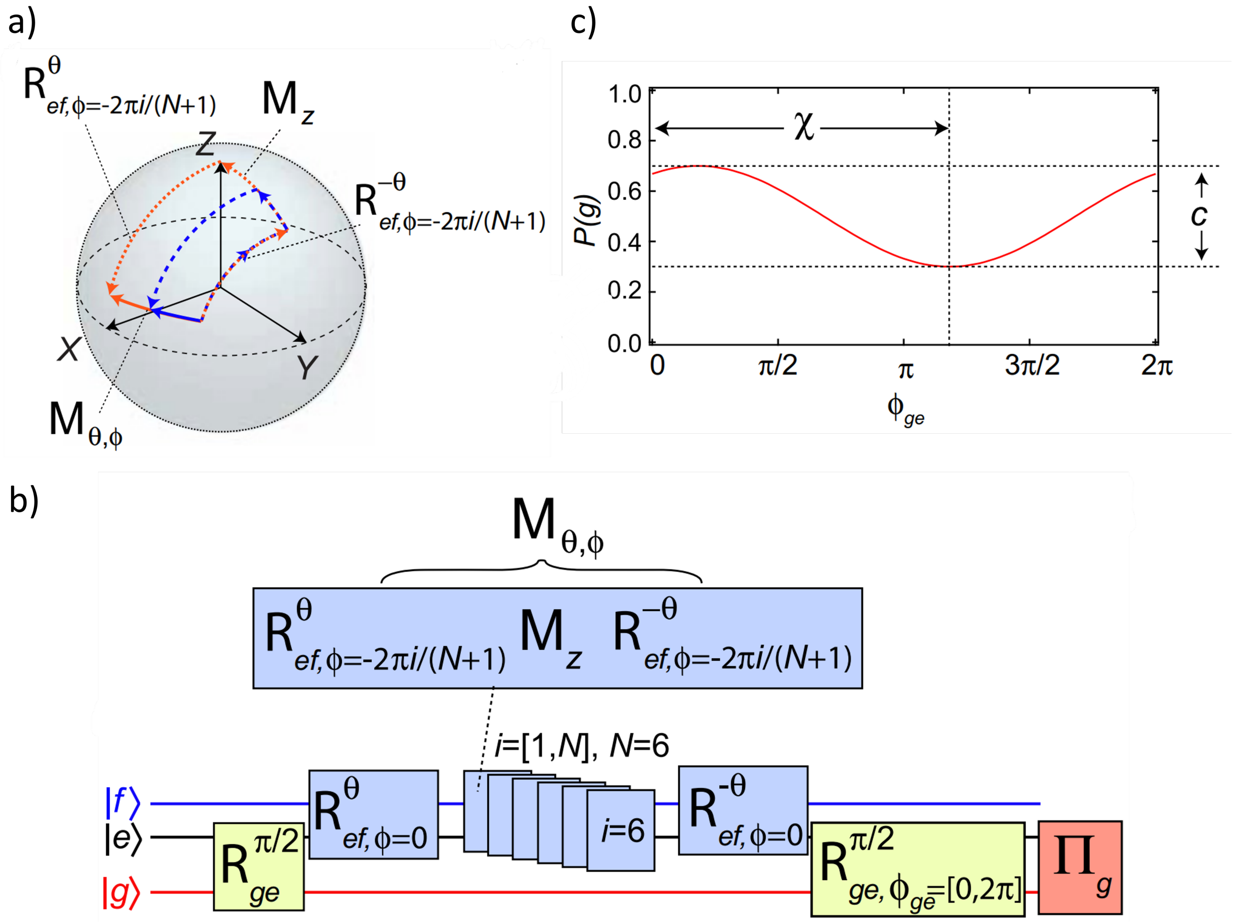

Fig. 2.3: **Experimental pulse sequence** (a) Measurements at an arbitrary point of the Bloch sphere are realized with the z axis measurement sandwiched by two rotation pulses which counter each other. Blue (red) arrows mark the actual (dashed lines) and effective (solid lines) trajectory of the weak (projective) measurement. (b) The entire arrangement of the experimental sequence, with six times of weak measurements around the Bloch sphere with a decreasing azimuthal angle, ϕ, and a chosen altitulde, θ. (c) Here $P(g)$ is the probability of obtaining outcome g from the final projective measurement, Π_g. From the final interference pattern between state $|g\rangle$ and $|e\rangle$, we extract the geometric phase, χ, and the interference contrast, c.

$\hat{V} + \frac{1}{2}[\hat{S}, \hat{V}] + O(\lambda^2)$. Then we have,

$$[\hat{S}, \hat{V}] = 2\hbar g\lambda[\hat{\sigma}_+\hat{a}, \hat{\sigma}_-\hat{a}^\dagger] = 2\hbar g\lambda(|e\rangle\langle e| + \hat{\sigma}_z\hat{a}^\dagger\hat{a}) \tag{2.27}$$

Moving to the corresponding rotating frame with ω_r for the qubit and ω_c for the cavity, we drop the fast rotating terms due to large cavity-qubit detuning. The effective Hamiltonian is obtained as,

$$\hat{H}_{\text{eff}} = \hbar\frac{\omega_q + \xi - \omega_r}{2}\hat{\sigma}_z + \hbar\xi\hat{\sigma}_z\hat{a}^\dagger\hat{a} + \hbar\epsilon_r\lambda(e^{i\alpha}\hat{\sigma}_- + e^{-i\alpha}\hat{\sigma}_+), \tag{2.28}$$

with $\xi = \lambda g = g^2/(\omega_q - \omega_c)$. Here we set the Rabi drive frequency to the dressed qubit resonance frequency, $\omega_r = \omega_q + \xi$. Since the cavity is driven off-resonantly, the qubit-cavity coupling term takes a higher order of small values ϵ/Δ and λ, we can omit the corresponding dephasing caused by the Rabi drive. Then, the operator in time interval τ, $\hat{R} = e^{-i\frac{\hat{H}_{\text{eff}}}{\hbar}\tau}$ can be written in basis $\{|e\rangle, |g\rangle\}$ as

$$\hat{R} = \begin{pmatrix} \cos\epsilon_r\lambda\tau & -i\sin\epsilon_r\lambda\tau e^{-i\alpha} \\ -i\sin\epsilon_r\lambda\tau e^{i\alpha} & \cos\epsilon_r\lambda\tau \end{pmatrix}. \tag{2.29}$$

The conclusion holds for the Rabi drive between state $|e\rangle$ and state $|f\rangle$ since we can independently drive adjacent levels due to the aharmonicity. For the rotation pulse $\hat{R}^\theta_{ef,\phi}$ taking state $|e\rangle$ to state $|\theta, \phi\rangle = \cos\frac{\theta}{2}|e\rangle + \sin\frac{\theta}{2}e^{i\phi}|f\rangle$, it can be represented in basis $\{|f\rangle, |e\rangle\}$ as

$$\hat{R}^\theta_{ef,\phi} = \begin{pmatrix} \cos\frac{\theta}{2} & \sin\frac{\theta}{2}e^{i\phi} \\ -\sin\frac{\theta}{2}e^{-i\phi} & \cos\frac{\theta}{2} \end{pmatrix}, \tag{2.30}$$

by choosing $\alpha = 3\pi/2 - \phi$ and $\epsilon_r\lambda\tau = \theta/2$. As we have shown, such realization of rotation pulses could prevent the system from generating additional dynamical phases.

2.3.4 Decoherence induced geometric phase

By now, we have only dealt with weak measurements with a certain series of outcomes forming a single trajectory. For each measurement with an outcome represented by a vector $\vec{r}$ on the I/Q plane, the Kraus operator for the two level system can be assumed to be

$$M_0^{(\vec{r})} = \begin{pmatrix} \tilde{\Psi}(\vec{r}) & 0 \\ 0 & \Psi(\vec{r}) \end{pmatrix} \tag{2.31}$$

with generality. Here $\Psi(\vec{r})$ and $\tilde{\Psi}(\vec{r})$ are functions satisfying the conditions $\int_\Omega \Psi^*(\vec{r})\Psi(\vec{r}) = 1$ and $\int_\Omega \tilde{\Psi}^*(\vec{r})\tilde{\Psi}(\vec{r}) = 1$. If we consider the overall Kraus operator for the entire three level system, since there are no measurement or dephasing happening between state $|g\rangle$ and state $|e\rangle$, the final Kraus operator written in basis of $\{|f\rangle, |e\rangle\}$ becomes

$$\hat{M}_z^{(\vec{r})} = \left(\begin{array}{cc|c} \tilde{\Psi}(\vec{r}) & 0 & 0 \\ 0 & \Psi(\vec{r}) & 0 \\ \hline 0 & 0 & \Psi(\vec{r}) \end{array}\right), \tag{2.32}$$

consistent with Equation 2.21. As is presented in Equation 2.22, with a certain series of measurement outcomes, $\{\vec{r}_1, \vec{r}_2, ..., \vec{r}_k, ...\}$, we briefly denote the final system state as,

$$|\phi_f\rangle = \hat{P}_{ge}\hat{R}_0 \prod_k (\hat{R}_k^\dagger \hat{M}_z^{(\vec{r}_k)} \hat{R}_k) \hat{R}_0^\dagger |\phi_i\rangle. \tag{2.33}$$

Since the geometric phase is eventually extracted with the cross term between the interference state $|f\rangle$ and the basis within the two-level system $|e\rangle$, it is the expectation value of operator Σ, where $\Sigma = \Sigma_x - i\Sigma_y = 2|g\rangle\langle e|$, with

$$\Sigma_x = \left(\begin{array}{cc|c} 0 & 0 & 0 \\ 0 & 0 & 1 \\ \hline 0 & 1 & 0 \end{array}\right), \Sigma_y = \left(\begin{array}{cc|c} 0 & 0 & 0 \\ 0 & 0 & -i \\ \hline 0 & i & 0 \end{array}\right). \tag{2.34}$$

Thus we have the definition of the geometric phase and its contrast, extracted from

$$ce^{i\chi} = \int_{\Omega} \langle \phi_f | \Sigma | \phi_f \rangle, \tag{2.35}$$

with Ω representing all possible sequences of values for $\{\vec{r}_k\}$. The operator A projects $|\phi_f\rangle$ into the $\{|g\rangle, |e\rangle\}$ subspace, effectively carried out the final projective measurement P_{ge}, which could be skipped in actual experiment.

Given the initial state $|\phi_i\rangle = a_i^{(e)} |e\rangle + a_i^{(g)} |g\rangle$, with certain measurement outcomes $\{\vec{r}_k\}$, the system is still in pure state $|\phi_f\rangle = a_f^{(e)}(\{\vec{r}_k\}) |e\rangle + a_f^{(g)}(\{\vec{r}_k\}) |g\rangle$. Since all the rotation operators R_k are in the $\{|e\rangle, |f\rangle\}$ manifold, the coefficient of the reference state $|g\rangle$ becomes

$$a_f^{(g)}(\{\vec{r}_k\}) = \prod_k \Psi(\vec{r}_k) a_i^{(g)}. \tag{2.36}$$

Then, the extracted geometric phase becomes

$$\begin{aligned} ce^{i\chi} &= 2 \int_{\Omega} \langle \phi_f | \, g \rangle \langle e \, | \phi_f \rangle = 2 \int_{\Omega} a_f^{(g)*}(\{\vec{r}_k\}) \langle e \, | \phi_f \rangle = 2 \langle e | \int_{\Omega} \prod_k \Psi^*(\vec{r}_k) a_i^{(g)*} |\phi_f\rangle \\ &= 2 a_i^{(g)*} \langle e | \int_{\Omega} \prod_k \Psi^*(\vec{r}_k) \hat{P}_{ge} \hat{R}_0 \prod_k \left(\hat{R}_k^\dagger \hat{M}_z^{(\vec{r}_k)} \hat{R}_k \right) \hat{R}_0^\dagger |\phi_i\rangle \\ &= 2 a_i^{(g)*} \langle e | \int_{\Omega} \hat{R}_0 \prod_k \left(\hat{R}_k^\dagger \Psi^*(\vec{r}_k) \hat{M}_z^{(\vec{r}_k)} \hat{R}_k \right) \hat{R}_0^\dagger |\phi_i\rangle . \end{aligned} \tag{2.37}$$

Here we note that the whole ensemble is a weighted average according to its Kraus operator coefficient $\Psi(\vec{r}_k)$ on the $\{|g\rangle, |e\rangle\}$ manifold depending on the measurement outcome, which is very similar to the case of selective averaging under very strong measurement. Finally we have

$$ce^{i\chi} = 2 a_i^{(g)*} \langle e | R_0 \prod_k \left(R_k^\dagger \tilde{M}_z R_k \right) R_0^\dagger |\phi_i\rangle , \tag{2.38}$$

with the integrated effective Kraus operator

$$\begin{aligned}
\tilde{M}_z &= \int_\Omega \Psi^*(\vec{r}) \left(\begin{array}{cc|c} \tilde{\Psi}(\vec{r}) & 0 & 0 \\ 0 & \Psi(\vec{r}) & 0 \\ \hline 0 & 0 & \Psi(\vec{r}) \end{array}\right) \\
&= \left(\begin{array}{cc|c} \int_\Omega \Psi^*(\vec{r})\tilde{\Psi}(\vec{r}) & 0 & 0 \\ 0 & \int_\Omega \Psi^*(\vec{r})\Psi(\vec{r}) & 0 \\ \hline 0 & 0 & \int_\Omega \Psi^*(\vec{r})\Psi(\vec{r}) \end{array}\right) \\
&= \left(\begin{array}{cc|c} \int_\Omega \Psi^*(\vec{r})\tilde{\Psi}(\vec{r}) & 0 & 0 \\ 0 & 1 & 0 \\ \hline 0 & 0 & 1 \end{array}\right) = \tilde{M}_z^{\{|e\rangle,|f\rangle\}} \otimes \hat{I}^{\{|g\rangle\}},
\end{aligned} \tag{2.39}$$

where $\tilde{M}_z^{\{|e\rangle,|f\rangle\}}$ is the null outcome weak measurement operator on the $\{|e\rangle, |f\rangle\}$ manifold, same as the one considered in previous theory works [19, 22, 23]. And $\hat{I}^{\{|g\rangle\}}$ is identity operator on state $|g\rangle$. Such ensemble averaged Kraus operator has the same form as the type of weak measurement studied in Section 2.2 with a positive outcome.

Hence, with the internal weighted averaging nature of the partial resolving measurement, we can extract the geometric phase with an effectively all-positive measurement outcome sequence, under all range of measurement strength. From now on, we can claim the geometric phase equivalence relation between a single trajectory under postselected measurements and the averaged ensemble under measurements without postselection, with the latter equivalent to pure dephasing between energy levels.

2.3.5 Simulation results

Instead of performing a postselected weak measurement, we can observe the geometric phase induced with the same form by applying dephasing with rate γ and time interval τ to the off-diagonal term in the density matrix. The above equivalence of extracted geometric phase

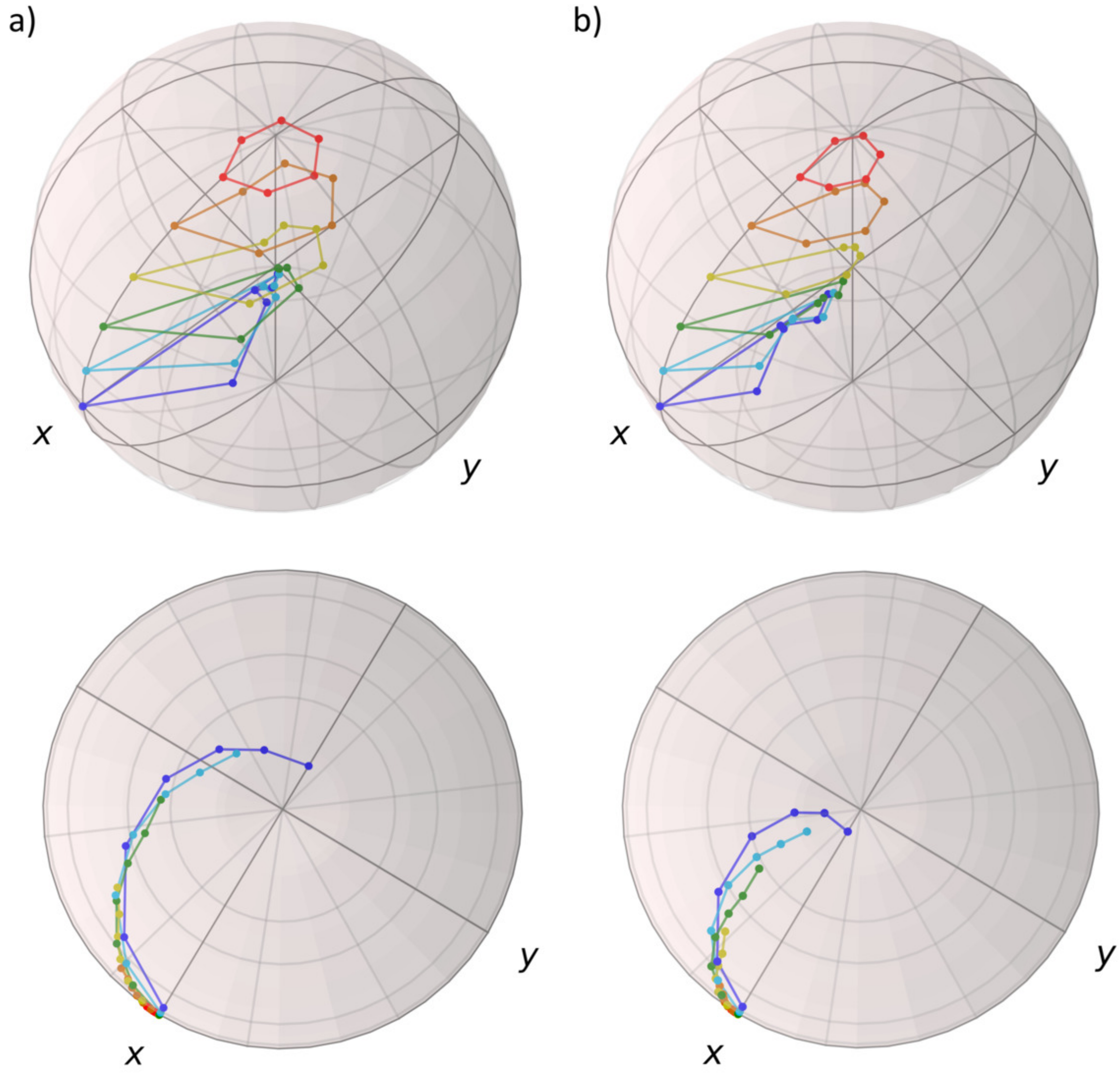

Fig. 2.4: Decoherence induced topological transition in geometric phase. (a) The amount of dephasing, which determines the weak measurement strength, is above the critical value. Upper: Representation of the reduced density matrix for the subspace spanned by states $\{|e\rangle, |f\rangle\}$ during the six weak measurements performed by dephasing and the one final measurement performed by projection. Lower: Representation of the reduced density matrix for the subspace spanned by states $\{|g\rangle, |e\rangle\}$ during the process. (b) The amount of dephasing, which determines the weak measurement strength, is below the critical value.

between dephasing process and postselected measurement indicates correspondence between the amount of dephasing performed during each interval, $\gamma\tau$, and the desired measurement strength, η. When we need to vary the measurement strength below and above the critical value, the amount of dephasing performed at each measurement is varied instead. For convenience, we choose to fix the induced dephasing rate, γ, and vary the time interval τ. In Fig. 2.4, we visualize the change in the system density matrix during the process of six weak measurements and one final projective measurement. The six weak measurements are performed by selective dephasing between state $|f\rangle$ and the subspace spanned by $\{|g\rangle, |e\rangle\}$. And the final projective measurement is performed naturally by the final tomography process. The evolution is shown on the Bloch sphere for the subspace spanned by states $\{|e\rangle, |f\rangle\}$ (Upper) and by states $\{|g\rangle, |e\rangle\}$ (Lower). The density matrices starts from a pure state at the positive direction of the x axis for both cases. As the density matrix evolves cyclically inside the Bloch sphere in subspace $\{|e\rangle, |f\rangle\}$, the geometric phase accumulates in subspace $\{|g\rangle, |e\rangle\}$. For strong measurements shown in Fig. 2.4 (a), the geometric phase gained along latitudes with polar angle $0 \to \pi$ varies continuously and ends up at the negative x axis. In contrast, for weak measurements shown in Fig. 2.4 (a), the continuously varying geometric phase ends up at the positive x axis. Such behaviour gives us either 0 or π for polar angle $\theta = \pi$ along the equator. If we consider the polar angle $0 \to 2\pi$, the strong measurement case gives a continuous cyclic evolution around the origin point, while the weak measurement case fails to circumvent the origin point. Such topologically distinct behaviour gives us either 0 or 2π for the geometric phase at the same polar angle $\theta = 2\pi$, at the opposite polar point. A discrete and abrupt jump of such topological behaviour happens between the strong measurement and weak measurement cases,

2.3.6 Experimental results

In this experiment, we utilize a superconducting Transmon circuit ($E_\mathrm{J}/h = 13.015$ GHz, $E_\mathrm{C}/h = 285$ MHz) to produce transition frequencies $\omega_{ge}/2\pi = 5.12487$ GHz, $\omega_{ef}/2\pi =$

4.80788 GHz. The Transmon circuit is embedded in a three-dimensional aluminum microwave cavity [24] with linewidth $\kappa/2\pi = 0.841$ MHz, where the dispersive interaction between the Transmon and the cavity causes the cavity frequency to shift from its bare resonance frequency of $\omega_{\text{bare}}/2\pi = 5.6724$ GHz to a state-dependent frequency of $\omega_g/2\pi = 5.6861$ GHz, $\omega_e/2\pi = 5.6743$ GHz, and $\omega_f/2\pi = 5.6715$ GHz. To control and measure the system, we employ three microwave generators, with one generator addressing the Transmon transitions through single-sideband modulation, another contributing the measurement at frequency ω_f, and a final generator operating at ω_{bare} to produce state readout through the Jaynes-Cummings nonlinearity technique [25]. The qubit/cavity system is embedded in copper and magnetic shielding and cooled to a base temperature of 10 mK in a dilution refrigerator. As is shown in Fig. 2.5, the input line is subject to 70 dB of attenuation and lossy low-pass microwave filtering, while the output stage passed through three cryogenic circulators before amplification with a HEMT amplifier.

For such experimental setup based on a Transmon circuit, we have to stabilize higher Transmon states against charge noise. Although a superconducting Transmon circuit is designed to reduce the charge noise sensitivity of the $|e\rangle$ state exponentially in the ratio between $E_{\text{J}}/h = 13.015$ GHz and $E_{\text{C}}/h = 285$ MHz [3], the third energy level $|f\rangle$ may still be affected by charge noise. We observe both increased dephasing in the $\{|e\rangle, |f\rangle\}$ manifold (Fig. 2.2), as well as abrupt transitions in the $|f\rangle$ energy and associated fluctuations. We stabilize the experiment against these fluctuations by tracking the Ramsey pattern in the $\{|e\rangle, |f\rangle\}$ manifold and sorting the acquired data in a post-processing step.

In order to probe the topological transition we record the geometric phase χ and interference contrast c for different trajectory latitudes and measurement strength. The results are displayed in Figure 2.6 and show good agreement with the theory and simulation results at measurement strengths above, below, and near the topological transition. In the limit of strong measurement, $\exp\{(-\gamma_{ef}\tau)\} \to 0$ (towards the data points where $\gamma_{ef}\tau \sim 2$ in the figure), the measurement backaction is sufficient to allow the quantum state to follow the

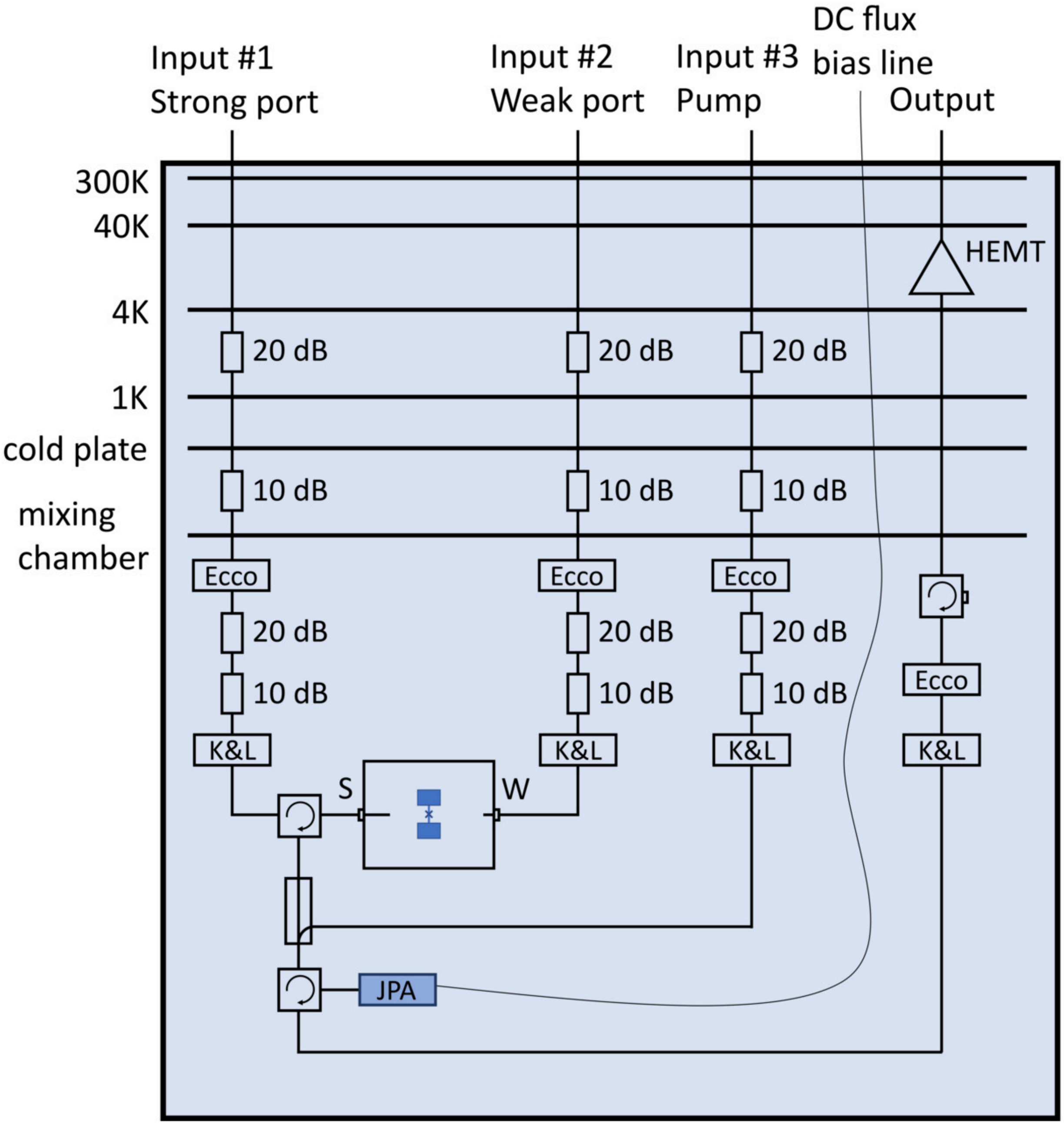

Fig. 2.5: The experimental layout in the dilution refrigerator. The Josephson parametric amplifier (JPA) flux control and pump circuit is meant for weak measurement readout, but not actively used in the actual experiment since we achieved equivalence between measurement and dephasing in obtaining the geometric phase.

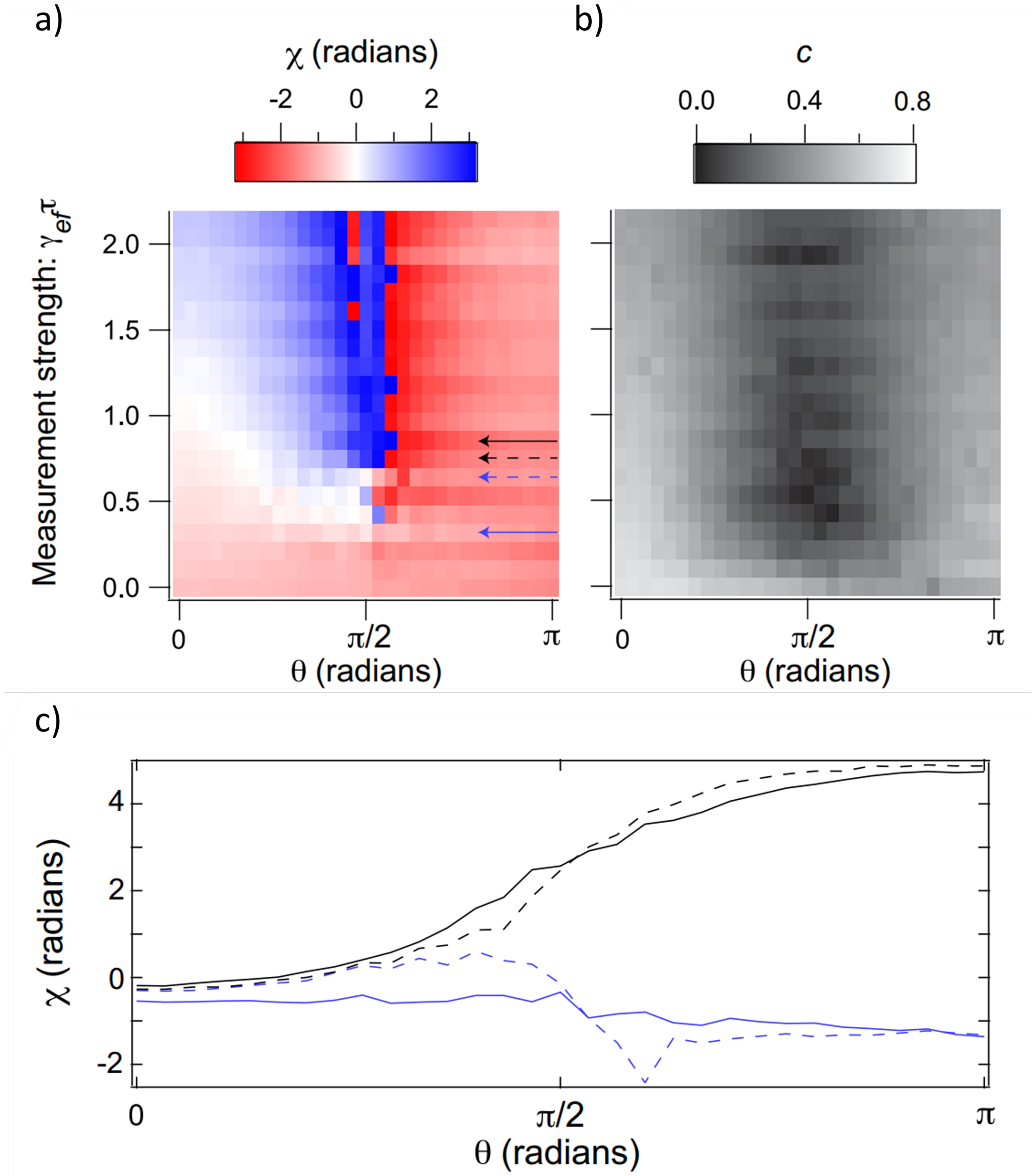

Fig. 2.6: Experimental results (a) The geometric phase under varying one-time measurement strength ($\gamma\tau$) gained with sequential measurements along different latitude of the Bloch sphere for polar angle $0-2\pi$. (b) The corresponding visibility of the extracted geometric phases.

measurement axis, leading to a monotonically increasing geometric phase with the polar angle. In the weak measurement limit, $\exp\{(-\gamma_{ef}\tau)\} \rightarrow 1$ (towards the data points where $\gamma_{ef}\tau \sim 0$ in the figure), no measurement dynamics occur, thus there is no observed dependence of the geometric phase on the polar angle. Between these two limits we encounter the topological transition, which appears as a 2π phase winding about a point of zero contrast. For $\theta = \pi/2$, this topological transition occurs as a function of the measurement strength. Increasing the measurement strength at $\theta = \pi/2$, we observe an abrupt jump in the geometric phase of π at a measurement strength of $\gamma t \sim 0.5$ associated with the contrast decreasing to zero. This transition corresponds to the critical measurement strength that drags the state half way around the Bloch sphere. Near the transition, the state after the final projection is a mixture of trajectories that either encircled the Bloch sphere, acquiring a geometric phase of π, and those that did not, acquiring null geometric phase. The resulting interference contrast therefore goes to zero as seen in Fig. 2.6 (b). For data along latitudes with polar angles from 0 to π, which is shown in Figure 2.6 (b), the geometric phase gained with strong enough measurements shows antisymmetrical behavior about the equator. This is consistent with the theory picture since the encircled solid angles are opposite to each other for trajectories that are symmetric about the equator plane. Meanwhile, the visibility near the transition point is also undergoing a dip that is wider and deeper around the equator but shallower and disappearing for traces near the Bloch sphere polar with $\theta = 0$ or π. This is also reasonable since the the geometric phase is gradually ill-defined near the transition point when approching the Bloch sphere equator, where the phase jump eventually happens, while the visibility is contantly 1 on the Bloch sphere polars,with all the sequential measurements actually happening at the same point.

To verify the above result, we take into account the dynamical phase gained in such situation. The quantum evolution in our experiment that takes place over $\sim \mu$s of evolution is associated with large dynamical phases (on the order of 10^4 radians). This dynamical phase is effectively canceled by the natural rotating frames associated with microwave generator

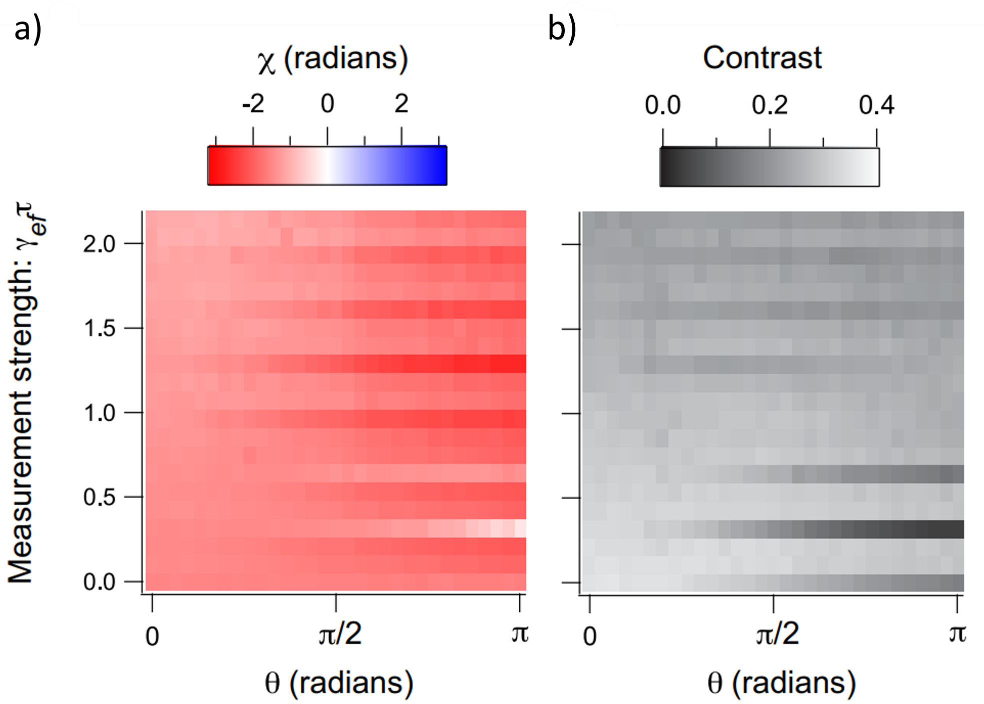

Fig. 2.7: Subtracting the dynamical part of the accumulated phase (a) The experimental results of accumulated dynamical phases, under the reference measurement sequences with fixed azimuth angle $\phi = 0$. (b) The corresponding contrast for the reference geometric phase. The dynamical phase here is smooth, indicating that it is effectively canceled through appropriate rotating frames.

used to perform Transmon rotations. To confirm this cancellation, we perform a reference experiment at each data point using rotation sequences with fixed $\phi = 0$ instead of the sequential $\phi = [0, -2\pi]$. The reference experiment makes the same number and strength of sequential measurements at the same point on the latitude instead of winding around the Z axis. The observed reference interference phase and contrast are shown in Fig. 2.7, indicating only ~ 1 radian residual dynamical phase variation. The observed stripe features in the reference phase and contrast are likely due to residual dynamical phase associated with the anharmonicity of the Transmon. This additional phase is in fact averaged to zero in the experiment with sequential measurements rotating with $\phi = [0, -2\pi]$, as is displayed in Fig. 2.6.

Chapter 3

State stabilization by dissipation

3.1 Overview

Dissipation is usually viewed as undesirable processes in handling quantum information, which destroys quantum coherence and should be removed by quantum error correction. However, dissipative processes can also contribute novel elements for quantum information processing when controlled and engineered [26]. One such application is in preparing a quantum manybody system into the ground state of a generic manybody Hamiltonian [27], as initializing the quantum manybody system into a specific state is a prerequisite by quantum simulation protocols in many cases. This kind of preparation is typically achieved in one of two ways. One can engineer the system with the interactions of a certain Hamiltonian and relax the system towards the ground state [28]. However, the appropriate interactions or relaxation may not be generally achievable, or sufficiently low temperatures may pose a challenge. Alternatively, one can prepare a manybody entangled state using adiabaticity [29, 30], where a system is initialized in a trivial ground state and the Hamiltonian is slowly tuned to adiabatically produce the manybody ground state. Here, high fidelity requires slow evolution and an absence of excess dissipation that induce quantum jumps between states. The limitations of these two approaches motivate the investigation of driven dissipative methods in preparing and stabilizing a manybody system in a non-trivial state. Here, by designing the dissipative terms in the system Lindbladian [9], the desired manybody state can be reached and stabilized as the fixed point of the resulting dynamics [31].

First proposed by Affleck, Kennedy, Lieb and Tasaki (AKLT) in 1987, the AKLT state (Fig. 3.1(a)) is a prototypical example of the Haldane phase [32] with a symmetry-protected topological order. It works as a resource state for measurement-based quantum computation [33, 34], and can be efficiently represented by matrix-product states (MPS) [35]. Since the MPS representation efficiently describes a large variety of low-energy states of manybody Hamiltonians, protocols that can produce the AKLT state may be generalized for a range of applications. Compared with the typical preparation method of the AKLT state based on its matrix product representation via postselection [36, 37], or based on sequential unitary gates [38] and assisted with measurements [39], driven-dissipative methods create the manybody state with robustness and self-correcting features. Here, the system coherence can last much longer than the lifetime of a single component. Prior proposals have addressed possible implementation in ion trap and cold atom systems [40, 41]. In this chapter we propose such preparation and stabilization of the AKLT state in a superconducting transmon platform.

In the experimental platform of superconducting qubits embedded in cQED setups, driven-dissipative methods have been realized in the stabilization of single body states [42, 43, 44, 45, 46, 47, 48, 49], two-body states [50, 51, 52], and manybody entangled states [53]. In this article, we propose a scheme to dissipatively stabilize the 1-dimensional AKLT state consisting of spin-1 particles on such a platform. As is presented in Fig. 3.1, a spin-1 chain can be realized with an array of superconducting transmon circuits [3], where each spin-1 particle is identified with lowest three energy levels as a qutrit [54]. Here the dissipative element is provided by automomous feedback [50] from reservoir engineering. With two qutrits both coupled to a microwave resonator, local drives combined with cavity dissipation pump the qutrit pair into the subspace where their total spin $S_{\text{total}} \in \{1, 0\}$. In stabilization of the ground state of a frustration-free Hamiltonian, the manybody entangled state is achieved by applying such two-body dissipation terms simultaneously on each nearest neighbour pair as the system size scales up [55]. We thus demonstrate the viability of preparing

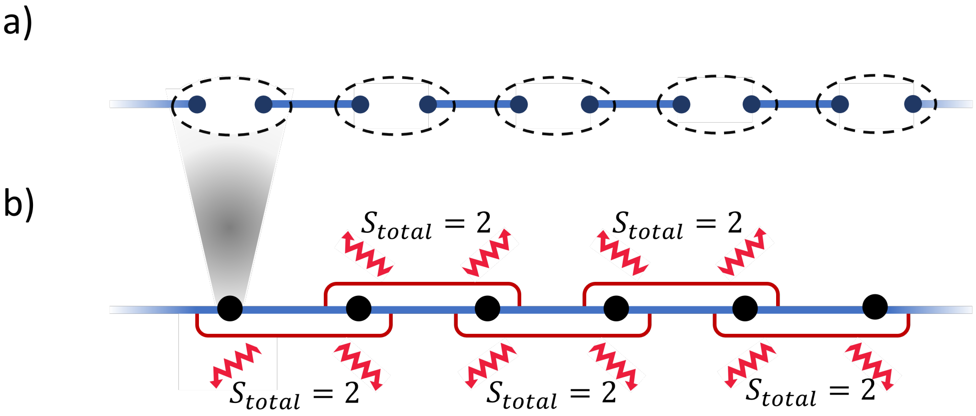

Fig. 3.1: Schemetic diagram of the AKLT state and the local dissipations applied. (a) The AKLT state represented in for of a spin-1/2 chain, the blue lines represent spin singlet pairs, and the dashed circles represent projections into spin triplet states. (b) The AKLT state represented in form of a spin-1 chain, where neighboring pairs of spin-1 particles are excluded from the $S_{\text{total}} = 2$ manifold. Here each spin-1 particle corresponds to two spin-1/2s as in the representation in (a), with the pair undergoing projection into the triplet subspace.

and stabilizing a weakly entangled manybody state, the AKLT state, within devices of superconducting transmon qutrits, linear microwave resonators, and specific microwave drives.

This work is structured as follows. In Section 3.2, we review the specific features of the AKLT state and describe the basic idea of stabilizing the AKLT state via quasi-local dissipations applied at the same time. In Section 3.3, we then try to generalize several one-qubit or two-qubit stabilization protocols to realize the desired quasi-local dissipations. With one successful generalization, we checked the protocol performance as the system scales up in Section 3.4, in terms of state preparation time and steady-state fidelity. Section 3.5 listed a possible chip design towards experimental realization.

3.2 The AKLT state

The AKLT Hamiltonian can be obtained with one quadratic term added to the quantum Heisenberg model

$$\hat{\mathrm{H}}_{\mathrm{AKLT}} = \sum_i [\vec{S}_i \cdot \vec{S}_{i+1} + \frac{1}{3}(\vec{S}_i \cdot \vec{S}_{i+1})^2]. \tag{3.1}$$

Here $\vec{S}_i$ is the angular momentum vector operator for the spin-1 particle on the i_{th} site. This model was first proposed by Affleck, Kennedy, Lieb and Tasaki (AKLT) in 1987 as an exactly solvable model with one unique ground state under periodic boundary condition [32]. It was significant for confirming the Haldane conjecture, by exemplifying a gapped excitation spectrum on an interger spin chain [56, 57, 58]. Such a ground state with finite energy differences to the excited states in the thermodynamic limit defines the Haldane phase, and thus a symmetry-protected topological (SPT) order for odd-integer spin particles, as in the 1-D AKLT chain [59, 60]. Hence, the AKLT state, being in the SPT phase, is short-range entangled, while its smooth transformation into a product state is prohibited without breaking, e.g. the $Z_2 \times Z_2$ symmetry [58]. Also, the computation capability of the AKLT chain as a quantum wire in measurement based quantum computation is shared by all states in the $Z_2 \times Z_2$ symmetry-protected topological phase [61]. The SPT order in the AKLT state can be detected by the string order parameter [62] or characterized by the entanglement spectrum [63].

The nontrivialness of the SPT order can be revealed by the edge states of the AKLT chain. Under open boundary condition, the unique ground state of $\hat{\mathrm{H}}_{\mathrm{AKLT}}$ becomes 4-fold degenerate, with two fractionalized degrees of freedom emerging on each of the two boundaries. Those edge modes are protected by symmetry, which means that their degeneracy can resist local perturbations that do not break, e.g. the $Z_2 \times Z_2$ symmetry [64]. For a better understanding of the edge states, one can visualize the AKLT state on a spin-1/2 chain, which is shown in Fig. 3.1 (a). In this case, the AKLT state can be obtained by preparing adjacent spin singlet pairs and then projecting each two edges into the spin triplet subspace. This is the approach that is followed in optical systems for the preparation of the AKLT state for measurement based quantum computation [36]. Such a representation views the edge modes as unpaired spin-1/2 particles.

To represent the AKLT state in a more relevant way to the driven-dissipative protocol, its parent Hamiltonian can also be written in the form of quasi-local projectors,

$$\hat{\mathrm{H}}_{\mathrm{AKLT}} = \sum_i \hat{P}^{S=2}_{i,i+1}. \tag{3.2}$$

Here $\hat{P}^{S=2}_{i,i+1}$ projects a pair of neighbouring spin-1 particles (the i_{th} and the $(i+1)_{\mathrm{th}}$) onto the subspace where their total spin equals 2, thereby adding an energetic cost to the $S_{\mathrm{total}} = 2$ subspace. Since the AKLT Hamiltonian is frustration-free [58], its ground state can be reached by driving each bond into the $S_{\mathrm{total}} \in \{0, 1\}$ subspace. The AKLT state can then be obtained whenever the projection onto $S_{\mathrm{total}} = 2$ is eliminated for each adjacent pair of sites, which is shown in Figure 3.1 (b).

3.3 Towards manybody state stabilization

For the aim of stabilizing a manybody entangled state by engineering two-body local interactions, we attempt to generalize existing two-body entanglement stabilization method or single qubit stabilization method into two-qutrit subspace. For already realized experiments of stabilizing a two-qubit Bell state, we consider two methods that may have enough degree of freedom, the parametric coupling method [52] and the autonomous feedback method [50]. We also consider generalizing the single qubit stabilization protocol utilizing Raman scattering [42]. In this section, the two-qubit protocols are reviewed, and the two-qutrit generalizations are explored, which is shown in Fig. 3.2. As is reviewed above, the AKLT Hamiltonian is frustration-free with a unique ground state on periodic boundary conditions and a four-fold degenerate ground state subspace with open boundary conditions. Thus, the AKLT state can be reached by the strategy of driving each two adjacent spin-1 particles out of the $S_{\mathrm{total}} = 2$ subspace, as is manifested by the projector form of $\hat{\mathrm{H}}_{\mathrm{AKLT}}$ in Eqn. 3.2. That is the stabilization of target subspace for the two-qutrit generalizations to realize.

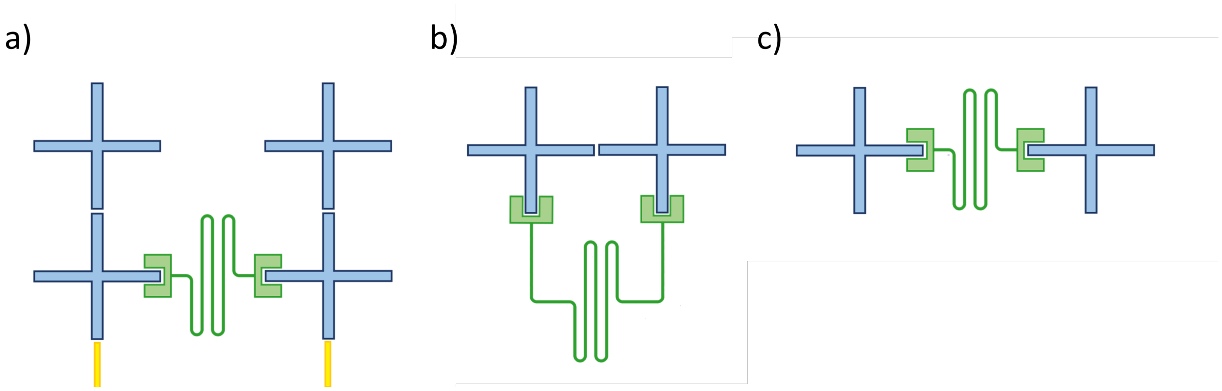

Fig. 3.2: Schemetic diagram of the two-qutrit minimal unit of the system designed by the three dissipation mechanisms. (a) The two-qutrit generalization of the trade-off free stabilization protocol, here each qutrit is coupled to the far-dentuned linear cavity via a flux-tuned coupler, which is modulated by AC and DC drives. (b) The two-qutrit generalization of the Raman scattering protocol, here the cavity shifted, first-two-level transitions of two qutrits are in resonance, while the anharmonicities have enough detuning. The two qutrits are capacitively coupled to each other and dispersively coupled to a common linear cavity. (c) The two-qutrit generalization of the autonomous feedback protocol, here the two cavities are both dispersively coupled to a common linear cavity, without any direct couplings between them.

3.3.1 The trade-off free stabilization protocol

3.3.1.1 Two qubit protocol

The parametric stabilization of two-qubit Bell state via driven dissipative method was proposed theoretically by Doucet et. al. [65] and carried out experimentally by Brown et. al. [52]. With the design of flux-tunable coupling strength mediated by a SQUID, for periodically varied flux one have periodically modulated coupling strength between the cavity and the qutrit or qubit. Driving at the two red sideband frequencies, and applying in-phase Rabi rotations on both the qubit and qutrit, the effective system Hamiltonian can be written as [52]

$$\mathrm{H}_{\mathrm{eff}} = \hat{a}^\dagger \hat{c}_p + \hat{a}\hat{c}_p^\dagger + \Omega_{\mathrm{A}}(|g\rangle_{\mathrm{A}}\langle e|_{\mathrm{A}} + |e\rangle_{\mathrm{A}}\langle g|_{\mathrm{A}}) + \Omega_{\mathrm{B}}(|g\rangle_{\mathrm{B}}\langle e|_{\mathrm{B}} + |e\rangle_{\mathrm{B}}\langle g|_{\mathrm{B}}), \tag{3.3}$$

when going to the rotating frame of both the qubit, the qutrit and the cavity, dropping the counter-rotating terms. Here $\hat{a}^\dagger$ and $\hat{a}$ are the creation and annilation operator of the cavity photon, $|g\rangle$, $|e\rangle$ and $|f\rangle$ are the energy levels of qutrit A and qubit B, and Ω are the Rabi frequency of the first two levels of qutrit A and qubit B. The collapse operator is given by

$$\hat{c}_p = c_A^{ef}|e\rangle_{\mathrm{A}}\langle f|_{\mathrm{A}} + c_A^{ge}|g\rangle_{\mathrm{A}}\langle e|_{\mathrm{A}} + c_B^{ge}|g\rangle_{\mathrm{B}}\langle e|_{\mathrm{B}}. \tag{3.4}$$

Here c_A^{ef}, c_A^{ge} and c_B^{ge} are complex numbers with controllable amplitudes and phases. When parameters are tuned to $c_A^{ge} = c_B^{ge}$, $\hat{c}_p$ has its dark states $|gg\rangle$ and $(|ge\rangle - |eg\rangle)/\sqrt{2}$, where $\hat{c}_p|gg\rangle = \hat{c}_p(|ge\rangle - |eg\rangle)/\sqrt{2} = 0$. Other than the subspace spanned by the dark spaces, the dissipation processes drive the system towards the Bell state via a higher level $|f\rangle$ in qutrit A, as is shown in Figure 3.3 (a). In this case, the system may still get trapped in dark state $|gg\rangle$, which could be resolved by applying the in-phase Rabi drive on both the qutrit and the qubit. With $\Omega_A = \Omega_B$, the effective unitary rotation operators are given by

$$\hat{R}_{\mathrm{eff}} = \hat{\sigma}_x^{\mathrm{A}} \otimes I^{\mathrm{B}} + I^{\mathrm{A}} \otimes \hat{\sigma}_x^{\mathrm{B}}, \tag{3.5}$$

Here $\hat{\sigma}$s are the Pauli matrices for the first two level of qutrit A and qubit B. Such drive connects between the represented spin triplet states, but with the spin singlet state as the dark state. In this process, the protocol stabilizes the system towards the Bell state regardless of the initial conditions.

3.3.1.2 Two qutrit generalization

The above two-qubit protocol is represented by the first two levels of a qutrit and a qubit. Here we try to extend the two-qubit protocol to a two-qutrit protocol represented by the first three levels of a qudit and a qutrit. The designed two-qutrit layout is shown in Fig. 3.2 (a), where two qutrits are coupled indirectly to a common linear cavity by two tunable couplers with flux tuning. Instead of the Bell state in the two-qubit case, the two-qutrit protocol has a four-dimensional target subspace of $S_{\mathrm{total}} \in \{0, 1\}$. As is shown in Figure 3.3 (b), we expect that $\hat{c}_p$ has its dark states including all four states in the $S_{\mathrm{total}} \in \{0, 1\}$ subspace. Other

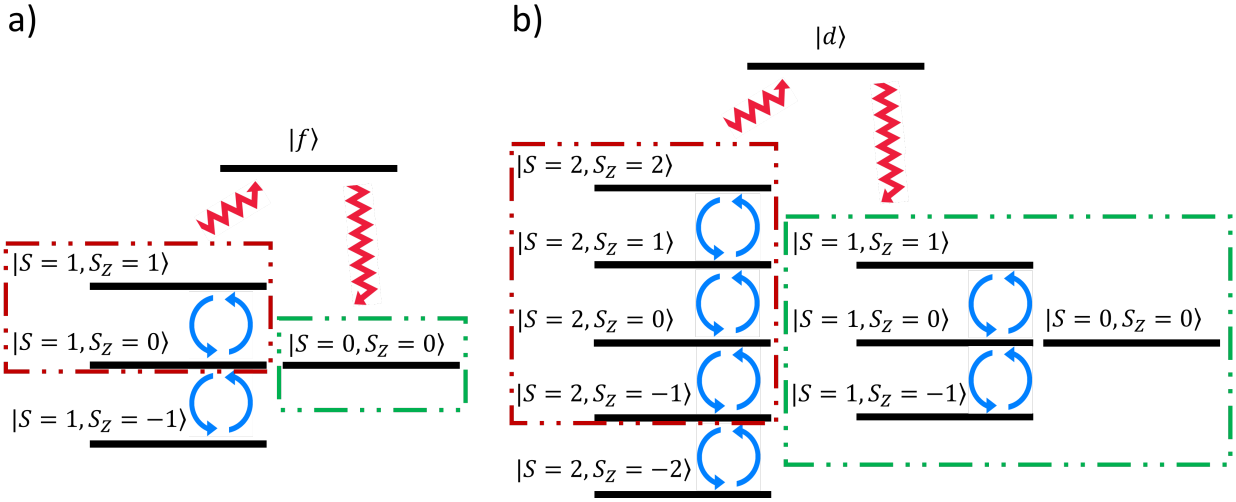

Fig. 3.3: Scheme of the trade-off free stabilization protocol. (a) Hilbert space engineering for the Bell state stabilization scheme [52]. The red rectangle encircles the subspace affected by the engineered collapse operator, and the green rectangle encircles the Bell state to stabilize the system into. The blue arrows are in-phase single qubit drives that connnect the unwanted dark state of the collapse operator, thus preventing the system from being trapped in that state. The red zigzagged arrows show the dissipative processes realized by parametric coupling between the qubits and the cavity. (b) Assumed Hilbert space engineering for the stabilization of two adjacent qutrits into the $S_{\text{total}} \in \{0, 1\}$ subspace. The red rectangle encircles the subspace affected by the engineered collapse operator, and the green rectangle encircles the target subspace to stabilize of $S_{\text{total}} \in \{0, 1\}$. The blue arrows are qutrit drives that connects the unwanted subspace with the states in red rectangle and the red zigzagged arrows show the dissipative processes. For a successful stabilization of the target subspace, the states in the green rectangle should all reside in the dark space of the collapse operator, with no crossover between the red and green rectangle.

than the subspace spanned by the dark spaces, the dissipation processes drive the system towards the target subspace via the fourth energy level $|d\rangle$ in qutrit A. Also, in-phase Rabi rotations between both $|g\rangle$, $|e\rangle$ and $|e\rangle$, $|f\rangle$ are applied to prevent the system from trapped in unwanted subspace. With the control ability to parameters, we assume that the effective Hamiltonian could be

$$\mathrm{H}_{\text{eff}} = \hat{a}^{\dagger}\hat{c}_p + \hat{a}\hat{c}_p^{\dagger} + \Omega_{\mathrm{A}}(|g\rangle_{\mathrm{A}}\langle e|_{\mathrm{A}} + |e\rangle_{\mathrm{A}}\langle f|_{\mathrm{A}} + h.c.) + \Omega_{\mathrm{B}}(|g\rangle_{\mathrm{B}}\langle e|_{\mathrm{B}} + |e\rangle_{\mathrm{B}}\langle f|_{\mathrm{B}} + h.c.), \tag{3.6}$$

With the collapse operator given by,

$$\begin{aligned}\hat{c}_p = c_A^{fd}|f\rangle_{\mathrm{A}}\langle d|_{\mathrm{A}} + c_A^{ge}|g\rangle_{\mathrm{A}}\langle e|_{\mathrm{A}} + c_A^{ef}|e\rangle_{\mathrm{A}}\langle f|_{\mathrm{A}} + c_A^{ge+}|e\rangle_{\mathrm{A}}\langle g|_{\mathrm{A}} + c_A^{ef+}|f\rangle_{\mathrm{A}}\langle e|_{\mathrm{A}} \\ + c_B^{ge}|g\rangle_{\mathrm{B}}\langle e|_{\mathrm{B}} + c_B^{ef}|e\rangle_{\mathrm{B}}\langle f|_{\mathrm{B}} + c_B^{ge+}|e\rangle_{\mathrm{B}}\langle g|_{\mathrm{B}} + c_B^{ef+}|f\rangle_{\mathrm{B}}\langle e|_{\mathrm{B}}.\end{aligned} \tag{3.7}$$

Here $|d\rangle_A$ is the fourth energy level of qudit A. We can see that, with the effective unitary rotation operators given by

$$\hat{R}_{\text{eff}} = \hat{\sigma}_x^{\mathrm{A}} \otimes I^{\mathrm{B}} + I^{\mathrm{A}} \otimes \hat{\sigma}_x^{\mathrm{B}}. \tag{3.8}$$

Since the rotation operator commutes with the total spin, the $S_{\text{total}} = 2$ subspace is connected while there is no component to rotate between $S_{\text{total}} = 2$ subspace and $S_{\text{total}} \in \{0, 1\}$ subspace. Hence, as long as we can design the parameters to reside the four-fold target subspace in the dark space of $\hat{c}_p$, the system can be stabilized in the target space regardless of its initial state. This requires that $\hat{c}_p|S^{\text{total}} \in \{0,1\}\rangle = 0$. Here $\hat{c}_p|S^{\text{total}} = 1, S_z^{\text{total}} = 1\rangle = 0$ means that $\hat{c}_p(|ef\rangle - |fe\rangle)/\sqrt{2} = 0$, which can be solved as

$$c_A^{ge} = c_B^{ge} = c_A^{gf} = c_B^{gf} = 0,\ c_A^{ef} = c_B^{ef},\ c_A^{ef+} = c_B^{ef+}.$$

Similarly, $\hat{c}_p|S^{\text{total}} = 1, S_z^{\text{total}} = 0\rangle = 0$ means that $\hat{c}_p(|gf\rangle - |fg\rangle)/\sqrt{2} = 0$, which can be solved as

$$c_A^{ge+} = c_B^{ge+} = c_A^{ef} = c_B^{ef} = 0,\ c_A^{gf} = c_B^{gf},\ c_A^{gf+} = c_B^{gf+}.$$

Also, $\hat{c}_p|S^{\text{total}} = 1, S_z^{\text{total}} = -1\rangle = 0$ means that $\hat{c}_p(|ge\rangle - |eg\rangle)/\sqrt{2} = 0$, which can be solved as

$$c_A^{gf+} = c_B^{gf+} = c_A^{ef+} = c_B^{ef+} = 0,\ c_A^{ge} = c_B^{ge},\ c_A^{ge+} = c_B^{ge+}.$$

Finally, $\hat{c}_p|S^{\text{total}} = 0, S_z^{\text{total}} = 0\rangle = 0$ means that $\hat{c}_p(|gf\rangle + |fg\rangle - |ee\rangle)/\sqrt{3} = 0$, which can be solved as

$$c_A^{ge} = c_B^{ef},\ c_B^{ge} = c_A^{ef},\ c_A^{ge+} = c_B^{ef+},\ c_B^{ge+} = c_A^{ef+},\ c_A^{gf} = -c_B^{gf},\ c_A^{gf+} = -c_B^{gf+}.$$

Here, a non-zero solution that satisfies all the four conditions does not exist. Hence, the degree of freedom that the two-qutrit protocol provides is not enough for stabilizing the four-dimensional subspace of $S^{\text{total}} \in \{0, 1\}$.

3.3.2 The Raman scattering protocol

3.3.2.1 Single qubit protocol

The single qubit stabilization protocol via Raman scattering was experimentally realized by Murch et. al. [42]. For a single qubit dispersively coupled to a linear cavity, the system Hamiltonian can be written as,

$$\hat{\mathrm{H}}_0 = \omega_r \hat{a}^\dagger \hat{a} + \frac{\omega_q}{2}\hat{\sigma}_z + \chi \hat{a}^\dagger \hat{a} \hat{\sigma}_z. \tag{3.9}$$

Here, ω_r, ω_q are the resonance frequencies of the cavity and the qubit and χ is the dispersive interaction term which represents the cavity shift. $\hat{a}^\dagger$ and $\hat{a}$ are the creation and annihilation operator of the cavity photon and $\hat{\sigma}$ are Pauli matrices on the qubit. With Rabi drive on the qubit at frequency ω_q' and cavity probe at ω_r', and in the corresponding rotating frame of the two frequencies, the system Hamiltonian becomes

$$\hat{\mathrm{H}} = (\omega_r - \omega_r')\hat{a}^\dagger \hat{a} + \frac{\omega_q - \omega_q'}{2}\hat{\sigma}_z + \chi \hat{a}^\dagger \hat{a} \hat{\sigma}_z + \frac{\Omega_R}{2}\hat{\sigma}_x + \varepsilon_r(\hat{a}^\dagger + \hat{a}) \tag{3.10}$$

Here Ω_R is the Rabi drive frequency and ε_r is the cavity probe amplitude. Displacing the field operator by the mean field, $\hat{a} = \bar{a} + \hat{d}$, we get a shift in the Hamiltonian from the transformation of the cavity dissipation term in the Lindblad master equation, $\delta \mathrm{H} = \frac{i\kappa}{2}(\bar{a}^*\hat{d} - \bar{a}\hat{d}^\dagger)$. Then the effective Hamiltonian becomes

$$\hat{\mathrm{H}}_{\text{eff}} = \Delta\omega_r \hat{d}^\dagger \hat{d} + (\frac{\Delta\omega_q}{2} + \chi\bar{n})\hat{\sigma}_z + \frac{\Omega_R}{2}\hat{\sigma}_x + \chi(\bar{a}^*\hat{d} + \bar{a}\hat{d}^\dagger + \hat{d}^\dagger\hat{d})\hat{\sigma}_z. \tag{3.11}$$

Here we have $\Delta\omega_r = \omega_r - \omega_r'$ and $\Delta\omega_q = \omega_q - \omega_q'$. Choosing parameters as $\frac{\Delta\omega_q}{2} + \chi\bar{n} = 0$, and representing the qubit in $|+\rangle$ and $|-\rangle$, which are the basis of operator $\hat{\sigma}_x$, this Hamiltonian can be written as,

$$\hat{\mathrm{H}}_{\text{eff}} = \Delta\omega_r \hat{d}^\dagger \hat{d} + \frac{\Omega}{2}(|+\rangle\langle+| - |-\rangle\langle-|) + \chi(\bar{a}^*\hat{d} + \bar{a}\hat{d}^\dagger + \hat{d}^\dagger\hat{d})(|+\rangle\langle-| + |-\rangle\langle+|). \tag{3.12}$$

For this instance, with the energy splitting much larger than the strength of the coupling term, $\Omega_R \gg \chi$, we can drop the counter rotating terms and arrive at

$$\hat{\mathrm{H}}'_{\text{eff}} = \Delta\omega_r \hat{d}^\dagger \hat{d} + \frac{\Omega}{2}(|+\rangle\langle+| - |-\rangle\langle-|) + \chi(\bar{a}^*\hat{d}|+\rangle\langle-| + \bar{a}\hat{d}^\dagger|-\rangle\langle+|).$$

Here, with dissipation term $\sqrt{\kappa}\hat{a}$ placed on the cavity photons, the two level system dissipates towards state $|-\rangle$.

3.3.2.2 Two qubit generalization

For two qubits A and B capacitively coupled with each other, and both coupled dispersively with the cavity, the system Hamiltonian after rorating wave approximation can be written as,

$$\hat{\mathrm{H}}_0 = \omega_r \hat{a}^\dagger\hat{a} + \frac{\omega_q^{\mathrm{A}}}{2}\hat{\sigma}_z^{\mathrm{A}} + \chi^{\mathrm{A}}\hat{a}^\dagger\hat{a}\hat{\sigma}_z^{\mathrm{A}} + \frac{\omega_q^{\mathrm{B}}}{2}\hat{\sigma}_z^{\mathrm{B}} + \chi^{\mathrm{B}}\hat{a}^\dagger\hat{a}\hat{\sigma}_z^{\mathrm{B}} + J(\hat{\sigma}_-^{\mathrm{A}}\hat{\sigma}_+^{\mathrm{B}} + \hat{\sigma}_+^{\mathrm{A}}\hat{\sigma}_-^{\mathrm{B}}).$$

Here, ω_r, ω_q^A and ω_q^B are the resonance frequencies of the cavity, qubit A and qubit B. χ_A and χ_B are the dispersive interaction terms which represent the cavity shift for qubit A and

B. J is the coupling strength between qubit A and qubit B. $\hat{a}^\dagger$ and $\hat{a}$ are the creation and annihilation operator of the cavity photon and $\hat{\sigma}$ are Pauli matrices on the qubits. When probing the cavity at ω_r' with amplitude ε_r, and moving into the rotating frame with ω_q' for the qubits and ω_r' for the cavity, the system Hamiltonian becomes

$$\hat{\mathrm{H}} = \Delta\omega_r \hat{a}^\dagger\hat{a} + \frac{\Delta\omega_q^A}{2}\hat{\sigma}_z^A + \chi^A \hat{a}^\dagger\hat{a}\hat{\sigma}_z^A + \frac{\Delta\omega_q^B}{2}\hat{\sigma}_z^B + \chi^B \hat{a}^\dagger\hat{a}\hat{\sigma}_z^B + J(\hat{\sigma}_-^{\mathrm{A}}\hat{\sigma}_+^{\mathrm{B}} + \hat{\sigma}_+^{\mathrm{A}}\hat{\sigma}_-^{\mathrm{B}}) + \varepsilon_r(\hat{a}^\dagger + \hat{a}) \tag{3.13}$$

Here we write $\Delta\omega_r = \omega_r - \omega_r'$, $\Delta\omega_q^A = \omega_q^A - \omega_q'$ and $\Delta\omega_q^B = \omega_q^B - \omega_q'$. Again, displacing the field operator by the mean field as in the above section, $\hat{a} = \bar{a} + \hat{d}$, as well as choosing parameters so that $\frac{\Delta\omega_q^A}{2} + \chi^A\bar{n} = 0$ and $\frac{\Delta\omega_q^B}{2} + \chi^B\bar{n} = 0$, the effective Hamiltonian becomes

$$\hat{\mathrm{H}}_{\mathrm{eff}} = \Delta\omega_r \hat{d}^\dagger\hat{d} + J(\hat{\sigma}_-^{\mathrm{A}}\hat{\sigma}_+^{\mathrm{B}} + \hat{\sigma}_+^{\mathrm{A}}\hat{\sigma}_-^{\mathrm{B}}) + (\bar{a}^*\hat{d} + \bar{a}\hat{d}^\dagger + \hat{d}^\dagger\hat{d})(\chi^A\hat{\sigma}_z^A + \chi^B\hat{\sigma}_z^B). \tag{3.14}$$

Here we assume state $|g\rangle$ and $|e\rangle$ to the qubits, denoting $|+\rangle = \frac{\sqrt{2}}{2}(|ge\rangle + |eg\rangle)$and $|-\rangle = \frac{\sqrt{2}}{2}(|ge\rangle - |eg\rangle)$, then the interaction term can be written as,

$$\hat{\sigma}_-^{\mathrm{A}}\hat{\sigma}_+^{\mathrm{B}} + \hat{\sigma}_+^{\mathrm{A}}\hat{\sigma}_-^{\mathrm{B}} = |+\rangle\langle+| - |-\rangle\langle-|$$

If we choose parameters as $\chi^A = -\chi^B = \chi_0$, then we have the cavity shift term written as,

$$\chi^A\hat{\sigma}_z^A + \chi^B\hat{\sigma}_z^B = \chi_0(\hat{\sigma}_z^A - \hat{\sigma}_z^B) = 2\chi_0(|+\rangle\langle-| + |-\rangle\langle+|)$$

With parameters satisfying $\Delta\omega_r = J$, we can eliminate the fast rotating term in the Hamiltonian and arrive at the effective Hamiltonian of

$$\hat{\mathrm{H}}_{\mathrm{eff}}' = \Delta\omega_r \hat{d}^\dagger\hat{d} + J(|+\rangle\langle+| - |-\rangle\langle-|) + 2\chi_0(\bar{a}^*\hat{d}|+\rangle\langle-| + \bar{a}\hat{d}^\dagger|-\rangle\langle+|) \tag{3.15}$$

Here, by the same process as in the single qubit case, when we apply dissipation term $\sqrt{\kappa}\hat{a}$ for the cavity photon, the system state can be driven unidirectionally from state $|+\rangle$ to state

$|-\rangle$. We thus numerically simulate the Lindblad master equation via Qutip [12, 13],

$$\frac{d}{dt}\rho(t) = -\frac{i}{\hbar}[\hat{\mathrm{H}}, \rho(t)] + \kappa \mathbf{D}[\hat{a}]\rho(t). \tag{3.16}$$

The Lindblad superoperator for an observable $\hat{O}$ acting on the density matrix ρ is defined as

$$\mathbf{D}[\hat{O}]\rho = \hat{O}\rho\hat{O}^\dagger - \frac{1}{2}\hat{O}^\dagger\hat{O}\rho - \frac{1}{2}\rho\hat{O}^\dagger\hat{O}. \tag{3.17}$$

Here the parameters are chosen as $\chi_0/2\pi = 1.5$ MHz and $J/2\pi = 15$ MHz for the unitary part $\hat{\mathrm{H}}$, $\bar{n} = 1$ for the averaged cavity photon population, and $\kappa/2\pi = 15$ MHz for the dissipation term. As is shown in Fig. 3.5 (a), the system is prepared in the fully mixed state in the two qubit Hilbert space, and the state population evolves under the protocol. We can see that for the states $|gg\rangle$ and $|ee\rangle$, the state populations are not affected by the protocol, but for state $|+\rangle$, which is denoted also by $|S = 1, S_z = 0\rangle$, the state population is evacuated and stabilized into $|S = 0, S_z = 0\rangle$, which is also $|-\rangle$.

Based on this partial stabilization mechanism, as is shown in Fig. 3.4 (a), the entire Hilbert space can be stabilized into $|-\rangle$ if drives are applied to rotate between different states in the $S_{\mathrm{total}} = 1$ subspace. With single qubit rotating drives applied in resonance and detuned by J, the Hamiltonian of the drives are

$$\hat{\mathrm{H}}^1_{\mathrm{rot}} = \Omega_1(\hat{\sigma}^A_x + \hat{\sigma}^B_x),\ \hat{\mathrm{H}}^2_{\mathrm{rot}} = \Omega_2 \cos{(Jt)}(\hat{\sigma}^A_x + \hat{\sigma}^B_x) - \Omega_2 \sin{(Jt)}(\hat{\sigma}^A_y + \hat{\sigma}^B_y).$$

With optimization on the amplitudes of the two drives, we have parameters chosen as $\Omega_1/2\pi = 0.825$ MHz and $\Omega_2/2\pi = 0.15$ MHz. As is shown in Fig. 3.5 (b), in about 10 times of the timescale in Fig. 3.5 (a), the stabilization of the entire subspace can be realized with state population fidelity over 95%.

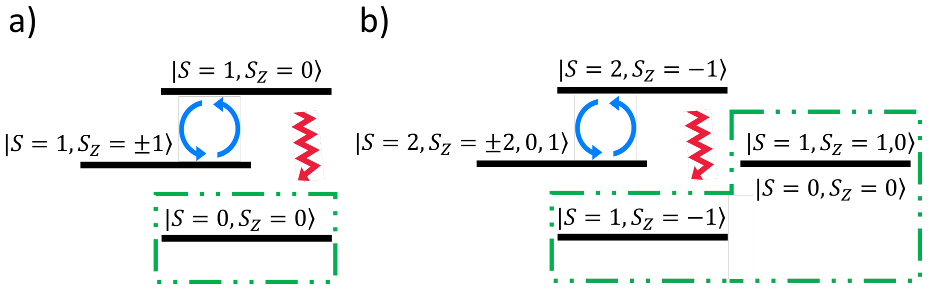

Fig. 3.4: Scheme of the two-qubit and two-qutrit Raman stabilization protocol. (a) For existing stabilization mechanism from state $|+\rangle$ to state $|-\rangle$, which is corresponding to from state $|S=1,S_z=0\rangle$ to state $|S=0,S_z=0\rangle$, the process is labeled by the red zigzaged arrow. The blue arrows are the rotating drives between state $+\rangle$ and other unwanted states $|gg\rangle$ and $|ee\rangle$, which is realized by resonant and detuned in-phase single qubit drives. And the green dashed rectangle encircles the target state to stabilize into. (b) For enough detuning between the anharmonicities of the two qutrits, same stabilization mechanism as in the two-qubit case from state $|+\rangle$ to state $|-\rangle$ exists. This corresponds to from state $|S=2,S_z=-1\rangle$ to state $|S=1,S_z=-1\rangle$ in the two-qutrit case, which is labeled by the red zigzaged arrow. The blue arrows are the rotating drives between state $+\rangle$ and other unwanted states, which is realized by resonant and in-phase single qutrit drives. And the green dashed rectangle encircles the target four-dimensional subspace to stabilize into.

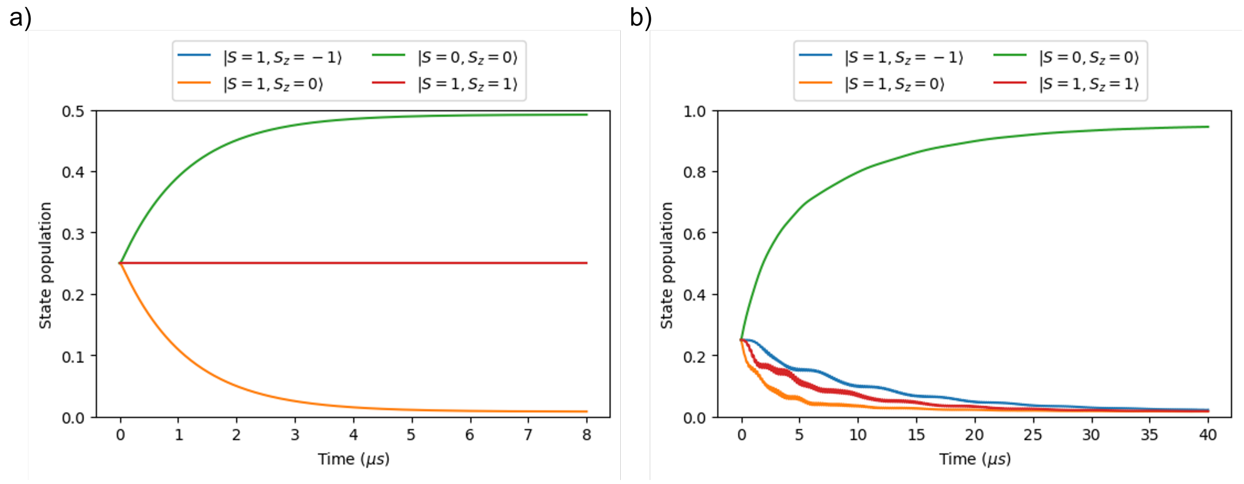

Fig. 3.5: Simulation results of the two-qubit Raman stabilization protocol. (a) The two qubits are prepared in fully mixed state in two-qubit Hilbert space. During the protocol without rotating drives between state $|+\rangle$ and other unwanted states, only the population of state $|+\rangle$ is eliminated and unidirectionally driven into state $|-\rangle$. (b) The two qubits are prepared in fully mixed state in two-qubit Hilbert space. During the protocol with single qubit drives between state $|+\rangle$ and other unwanted states, all three states except state $|-\rangle$ have their state populations eliminated, and the state population of state $|-\rangle$ is preserved and stabilized into.

3.3.2.3 Two qutrit generalization

Fig. 3.2 (b) shows two qutrits A and B capacitively coupled with each other, and both coupled dispersively with the cavity. Denoting the three qutrit energy levels as $|g\rangle$, $|e\rangle$ and $|f\rangle$, we have the transition energies from state $|g\rangle$ to state $|e\rangle$ for the two qutrits in resonance, but with the transition energies from state $|e\rangle$ to state $|f\rangle$ for the two qutrits off-resonant. This can be realized by having the anharmonicities of the two qutrits different, with e.g. $\alpha_1 = -150$ MHz and $\alpha_2 = -300$ MHz. Then the system Hamiltonian after rorating wave approximation can be written as,

$$\begin{aligned}\hat{\mathrm{H}}_0 = {} & \hbar\omega_{\mathrm{r}}\hat{a}^\dagger\hat{a} + \hbar\sum_j \omega_j^{\mathrm{A}}|j\rangle^{\mathrm{A}}\langle j|^{\mathrm{A}} + \hbar\sum_j \omega_j^{\mathrm{B}}|j\rangle^{\mathrm{B}}\langle j|^{\mathrm{B}} \\ & + \hbar\sum_j(\chi_j^{\mathrm{A}}|j\rangle^{\mathrm{A}}\langle j|^{\mathrm{A}} + \chi_j^{\mathrm{B}}|j\rangle^{\mathrm{B}}\langle j|^{\mathrm{B}})\hat{a}^\dagger\hat{a} + J(|g\rangle^A|e\rangle^B\langle e|^A\langle g|^B + |e\rangle^A|g\rangle^B\langle g|^A\langle e|^B).\end{aligned} \tag{3.18}$$

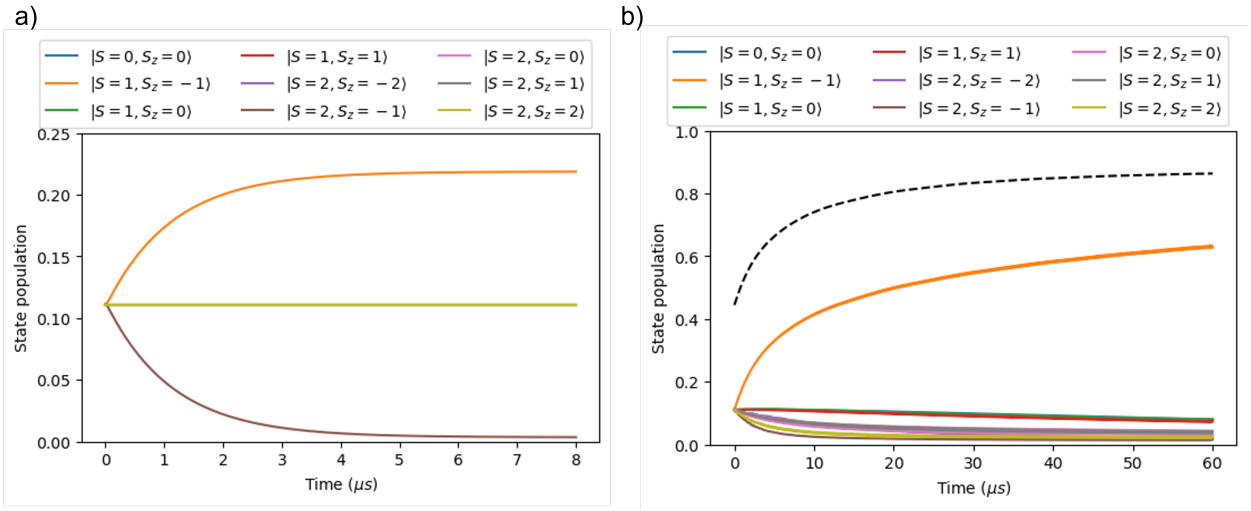

Fig. 3.6: Simulation results of the two-qutrit Raman stabilization protocol. (a) The two qutrits are prepared in fully mixed state in two-qutrit Hilbert space. During the protocol without single qutrit drives rotating between different states within subspace $S_{\text{total}} = 2$, only the population of state $|+\rangle$ ($|S = 2, S_z = -1\rangle$) is eliminated and unidirectionally driven into state $|-\rangle$ ($|S = 1, S_z = -1\rangle$). (b) The two qutrits are prepared in fully mixed state in two-qutrit Hilbert space. During the protocol with single qutrit drives between state $|+\rangle$ and other unwanted states, all five states with $S_{\text{total}} = 2$ have their state populations eliminated, and the state population of state $|-\rangle$ ($|S = 1, S_z = -1\rangle$) is preserved and stabilized into. However, the populations of other states in the stabilized subspace, $|S = 1, S_z = 0, 1$ and $|S = 0, S_z = 0$, are also reduced slowly over time.

Here $|j\rangle$ and $\hbar\omega_j$ represents the energy levels and corresponding energy eigenvalues of the energy levels for both qutrit A and B. And $\hbar\chi_j^{\mathrm{A(B)}}$ are the interaction energies between the cavity and qutrit A(B), indicating the cavity resonance frequency's shift summed over that induced by qutrit A and qutrit B. J is the coupling strength between the $|g\rangle$ to $|e\rangle$ transitions of qubit A and qubit B. When probing the cavity at ω_r' with amplitude ε_r, and moving into the rotating frame with ω_j' for the qutrits and ω_r' for the cavity, the system Hamiltonian becomes

$$\begin{aligned}\hat{\mathrm{H}} &= \hbar\Delta\omega_{\mathrm{r}}\hat{a}^\dagger\hat{a} + \hbar\sum_j \Delta\omega_j^{\mathrm{A}}|j\rangle^{\mathrm{A}}\langle j|^{\mathrm{A}} + \hbar\sum_j \Delta\omega_j^{\mathrm{B}}|j\rangle^{\mathrm{B}}\langle j|^{\mathrm{B}} + \varepsilon_r(\hat{a}^\dagger + \hat{a}) \\ &+ \hbar\sum_j(\chi_j^{\mathrm{A}}|j\rangle^{\mathrm{A}}\langle j|^{\mathrm{A}} + \chi_j^{\mathrm{B}}|j\rangle^{\mathrm{B}}\langle j|^{\mathrm{B}})\hat{a}^\dagger\hat{a} + J(|g\rangle^A|e\rangle^B\langle e|^A\langle g|^B + |e\rangle^A|g\rangle^B\langle g|^A\langle e|^B).\end{aligned} \tag{3.19}$$

Here we write $\Delta\omega_r = \omega_r - \omega_r'$, $\Delta\omega_j^A = \omega_j^A - \omega_j'$ and $\Delta\omega_j^B = \omega_j^B - \omega_j'$. Choosing parameters so that $\Delta\omega_j^A + \chi_j^A\bar{n} = 0$ and $\Delta\omega_j^B + \chi_j^B\bar{n} = 0$, as well as $\Delta\omega_r = J$, we thus numerically simulate the Lindblad master equation via Qutip [12, 13],

$$\frac{d}{dt}\rho(t) = -\frac{i}{\hbar}[\hat{\mathrm{H}}, \rho(t)] + \kappa\mathbf{D}[\hat{a}]\rho(t). \tag{3.20}$$

The Lindblad superoperator for an observable $\hat{O}$ acting on the density matrix ρ is defined as

$$\mathbf{D}[\hat{O}]\rho = \hat{O}\rho\hat{O}^\dagger - \frac{1}{2}\hat{O}^\dagger\hat{O}\rho - \frac{1}{2}\rho\hat{O}^\dagger\hat{O}. \tag{3.21}$$

The parameters are chosen as $\chi_{ge}^A/2\pi = -3$ MHz, $\chi_{gf}^A/2\pi = -4.5$ MHz, $\chi_{ge}^A/2\pi = 3$ MHz, $\chi_{ge}^A/2\pi = 3.5$ MHz, and $J/2\pi = 15$ MHz for the unitary part $\hat{\mathrm{H}}$, $\bar{n} = 1$ for the averaged cavity photon population, and $\kappa/2\pi = 15$ MHz for the dissipation term. As is described in Section 3.2, the two-qutrit protocol is expected to stabilize the system into the subspace where $S_{\mathrm{total}} \in 0, 1$. This is shown in Fig. 3.6 (a), the system is prepared in the fully mixed state in the two qutrit Hilbert space, and the state population evolves under the protocol. We can see that for state $|+\rangle$, which is denoted also by $|S = 2, S_z = -1\rangle$, the state population is evacuated and stabilized into $|S=1,S_z=-1\rangle$, which is also $|-\rangle$. For the 7-dimensional subspace orthogonal to those two states, the state populations are not affected by the protocol.

Based on this stabilization mechanism for one of the unwanted states, as is shown in Fig. 3.4 (b), the entire unwanted subspace can be stabilized into $|-\rangle$ if drives are applied to rotate between different states in the $S_{\text{total}}=2$ subspace. With single qutrit rotating drives applied in resonance and detuned by J, the Hamiltonian of the drives are

$$\hat{\mathrm{H}}^1_{\text{rot}}=\Omega_1(\hat{S}^A_x+\hat{S}^B_x),\ \hat{\mathrm{H}}^2_{\text{rot}}=\Omega_2\cos{(Jt)}(\hat{S}^A_x+\hat{S}^B_x)-\Omega_2\sin{(Jt)}(\hat{S}^A_y+\hat{S}^B_y).$$

With optimization on the amplitudes of the two drives, we have parameters chosen as $\Omega_1/2\pi=1.5$ MHz and $\Omega_2/2\pi=0.9$ MHz. As is shown in Fig. 3.6 (b), in about 10 times of the timescale in Fig. 3.6 (a), the target subspace population reaches a steady value over 85%. For this protocol, the typical timescale for a reasonable set of experimental parameters is quite long, with trade-offs between the final fidelity and the stabilization time. Also, mixing and dephasing happens considerably within the stabilized subspace, which does not necessarily commutes with the AKLT Hamiltonian and thus hinders the two-qutrit protocol to be generalized into a manybody protocol.

3.3.3 The autonomous feedback protocol

3.3.3.1 Two qubit protocol

In this section, we review the autonomous feedback protocol on two qubits stabilizing the two qubit Bell state. This protocol was theoretically proposed by Leghtas et. al. [66] and also experimentally carried out on two superconducting qubits [50]. We consider a linear cavity simultaneously coupled with both qubit A and B, then the system Hamiltonian can be written as [66]

$$\hat{\mathrm{H}} = \hbar\omega_{\mathrm{r}}\hat{a}^{\dagger}\hat{a} + \hbar\omega_{\mathrm{A}}\frac{\hat{\sigma}_z^{\mathrm{A}}}{2} + \hbar\omega_{\mathrm{B}}\frac{\hat{\sigma}_z^{\mathrm{B}}}{2} + \hbar g_{\mathrm{A}}(\hat{\sigma}_+^{\mathrm{A}}\hat{a} + \hat{\sigma}_-^{\mathrm{A}}\hat{a}^{\dagger}) + \hbar g_{\mathrm{B}}(\hat{\sigma}_+^{\mathrm{B}}\hat{a} + \hat{\sigma}_-^{\mathrm{B}}\hat{a}^{\dagger}) \tag{3.22}$$

in rotating wave approximation. Here ω_r, ω_A and ω_B are the transition frequencies for the linear cavity, qubit A and qubit B. Parameters g_A and g_B are the coupling strengths between qubit A or B and the linear cavity. Operators $\hat{a}^{\dagger}$ and $\hat{a}$ are the creation and annilation operator of the cavity photon, and $\hat{\sigma}$ represents Pauli operators on qubit A and B. With large enough detuning between resonance frequencies of the elements compared to the coupling strengths, the nearest neighbor couplings are dispersive and the next nearest neighbour virtual interaction is effectively turned off [67]. In the rotating frame of the two qubit and the cavity, performing the dispersive limit, the effective Hamiltonian becomes,

$$\hat{\mathrm{H}}_{\mathrm{eff}} = \hbar\chi_{\mathrm{A}}\frac{\hat{\sigma}_z^{\mathrm{A}}}{2}\hat{a}^{\dagger}\hat{a} + \hbar\chi_{\mathrm{B}}\frac{\hat{\sigma}_z^{\mathrm{B}}}{2}\hat{a}^{\dagger}\hat{a}. \tag{3.23}$$

Here $\hbar\chi_{\mathrm{A(B)}}$ is the interaction energy between the cavity and qubit A(B). This indicates a shift in the cavity resonance frequency equivalent to the addition of the shifts from qubit A and B, as is shown in the shifted cavity spectrum in Fig. 3.7(a). This interaction term also indicates a shift in the qubit spectrum corresponding to different photon numbers in the cavity, which allows us to perform qubit operations conditioned on the cavity photon population.

Representing a spin-half particle as a two-level system denoted by $|g\rangle$ and $|e\rangle$, Fig. 3.7(b) demonstrates Hilbert space engineering in this dissipative stabilization scheme. The cavity is driven at $\omega_{\mathrm{r}} - (\chi_{\mathrm{A}} + \chi_{\mathrm{B}})/2$ and $\omega_{\mathrm{r}} + (\chi_{\mathrm{A}} + \chi_{\mathrm{B}})/2$, corresponding to the resonance spectrum peaks for two-qubit states $|gg\rangle$ and $|ee\rangle$. Thus, whenever the qubits are in $|gg\rangle$ or $|ee\rangle$, the cavity photon population ramps up to an average number of $\bar{n}$. Otherwise, the cavity photon number exponentially decays to zero assuming that $\chi \gg \kappa$.

When the cavity is populated with 0 photons, the transition energies for qubit A and

B are $\hbar\omega_\mathrm{A}$ and $\hbar\omega_\mathrm{B}$, while when the cavity is populated with n photons, the transition energies for qubit A and B are shifted as $\hbar\omega'_\mathrm{A} = \hbar\omega_\mathrm{A} + \hbar\chi_\mathrm{A} n$ and $\hbar\omega'_\mathrm{B} = \hbar\omega_\mathrm{B} + \hbar\chi_\mathrm{B} n$. Hence, we can consider two types of single-qubit Rabi drives on both qubits. The "0-photon drive" is applied at $\omega_{\mathrm{A(B)}}$ with Rabi frequency Ω^0 while the "n-photon drive" is applied at $\omega_{\mathrm{A(B)}} + \chi_{\mathrm{A(B)}} n$ with Rabi frequency Ω^n, given that $n \approx \bar{n}$. Therefore, the former qubit drive is on resonance with the cavity unpopulated while the latter requires a component into the photon number eigenstate of n. The effective Hamiltonian for the qubit drives are given by

$$\begin{aligned} \hat{H}^0_\text{eff} &\propto \hat{\sigma}^\mathrm{A}_x \otimes I^\mathrm{B} + I^\mathrm{A} \otimes \hat{\sigma}^\mathrm{B}_x, \\ \hat{H}^n_\text{eff} &\propto \hat{\sigma}^\mathrm{A}_x \otimes I^\mathrm{B} - I^\mathrm{A} \otimes \hat{\sigma}^\mathrm{B}_x. \end{aligned} \tag{3.24}$$

We will now denote the cavity state with average photon number $\bar{n}$ in the rotating frame of its own driving frequency can be denoted as $|\bar{n}\rangle^\mathrm{C}$. When the qubit–cavity system is in $|gg\rangle|0\rangle^\mathrm{C}$ or $|ee\rangle|0\rangle^\mathrm{C}$, the cavity starts to populate with photons and is driven to a coherent state $|gg\rangle|\bar{n}\rangle^\mathrm{C}$ or $|ee\rangle|\bar{n}\rangle^\mathrm{C}$. At this moment, the "$n$-photon drive" come into resonance, rotating state $|gg\rangle|\bar{n}\rangle^\mathrm{C}$ and $|ee\rangle|\bar{n}\rangle^\mathrm{C}$ into state $|\phi_-\rangle|\bar{n}\rangle^\mathrm{C}$. Once leaving the two-qubit subspace spanned by states $|gg\rangle$ and $|ee\rangle$, with the system state in $|\phi_-\rangle|\bar{n}\rangle^\mathrm{C}$, the cavity probes are no longer in resonance. Subsequently, the cavity photon population decays into $|\phi_-\rangle|0\rangle^\mathrm{C}$, setting the "$n$-photon drive" off-resonant again. When Ω^n has the same scale as the cavity linewidth κ, the "n-photon drive" combined with cavity probes drives the two-qubit state unidirectionally from state $|gg\rangle|0\rangle^\mathrm{C}$ and $|ee\rangle|0\rangle^\mathrm{C}$ to the target Bell state $|\phi_-\rangle|0\rangle^\mathrm{C}$. As is shown in the inset of Fig. 3.7(b), the effect of such an autonomous feedback process is similar to that of quantum jump operators $|\phi_-\rangle\langle gg|$ and $|\phi_-\rangle\langle ee|$, which occur at a rate proportional to κ. Aside from the above feedback loop, the "0-photon drive" is applied to induce rotations between state $|\phi_+\rangle|0\rangle^\mathrm{C}$ and state $|gg\rangle|0\rangle^\mathrm{C}$ or $|ee\rangle|0\rangle^\mathrm{C}$. Choosing Ω^0 to be comparable with κ, any state in the Hilbert space is driven into the target Bell state $\{|\phi_+\rangle, |gg\rangle, |ee\rangle\} \to |\phi_-\rangle$. To summarize, the qubit protocol involves a "pump" that drives unwanted states $\{|\phi_+\rangle, |gg\rangle, |ee\rangle\}|0\rangle^{\mathrm{C}}$ to $\{|gg\rangle, |ee\rangle\}|\bar{n}\rangle^{\mathrm{C}}$. This then activates a "reset" which drives the qubits to $|\phi_-\rangle$, and the cavity decays to $|0\rangle^{\mathrm{C}}$.

3.3.3.2 Two qutrit generalization

In this section we generalize the above two-qubit protocol utilizing autonomous feedback of the reservoir to two-qutrit case, where we stabilize each nearest neighbour pair of a spin-1 chain [68]. As is stated in Section 3.2, the AKLT state can be reached by the strategy of driving each two adjacent spin-1 particles out of the $S_{\text{total}} = 2$ subspace. Hence, in this generalization towards two-qutrit system, we stabilize the system into two-qutrit subspace representing $S_{\text{total}} \in \{0, 1\}$ instead of the two-qubit Bell state.

Consider two qutrits coupled to a common linear cavity in the strong dispersive regime, which is shown in Fig. 3.2 (c). Without applied drives, the system Hamiltonian after rotating wave approximation becomes

$$\begin{aligned}\hat{\mathrm{H}} = {} & \hbar\omega_{\mathrm{r}}\hat{a}^\dagger\hat{a} + \hbar\sum_j \omega_j^{\mathrm{A}}|j\rangle^{\mathrm{A}}\langle j|^{\mathrm{A}} + \hbar\sum_j \omega_j^{\mathrm{B}}|j\rangle^{\mathrm{B}}\langle j|^{\mathrm{B}} + \\ & \hbar\sum_j g_j^{\mathrm{A}}(|j\rangle^{\mathrm{A}}\langle j+1|^{\mathrm{A}}\hat{a}^\dagger + |j+1\rangle^{\mathrm{A}}\langle j|^{\mathrm{A}}\hat{a}) + \hbar\sum_j g_j^{\mathrm{B}}(|j\rangle^{\mathrm{B}}\langle j+1|^{\mathrm{B}}\hat{a}^\dagger + |j+1\rangle^{\mathrm{B}}\langle j|^{\mathrm{B}}\hat{a})\end{aligned} \tag{3.25}$$

Here $|j\rangle$ and $\hbar\omega_j$ represents the energy levels and corresponding energy eigenvalues of the energy levels for both qutrit A and B. Parameter g_j represents the coupling strength between certain energy level and the cavity mode. With large enough detuning of resonance frequencies between the energy levels compared to the coupling strengths, we again negletct the next nearest neighbour virtual interaction, and consider the nearest neighbor couplings as dispersive. In the rotating frame of the two qutrit and the cavity, going to the dispersive limit, the effective Hamiltonian becomes,

$$\hat{\mathrm{H}}_{\mathrm{eff}} = \hbar\sum_j(\chi_j^{\mathrm{A}}|j\rangle^{\mathrm{A}}\langle j|^{\mathrm{A}} + \chi_j^{\mathrm{B}}|j\rangle^{\mathrm{B}}\langle j|^{\mathrm{B}})\hat{a}^\dagger\hat{a}. \tag{3.26}$$

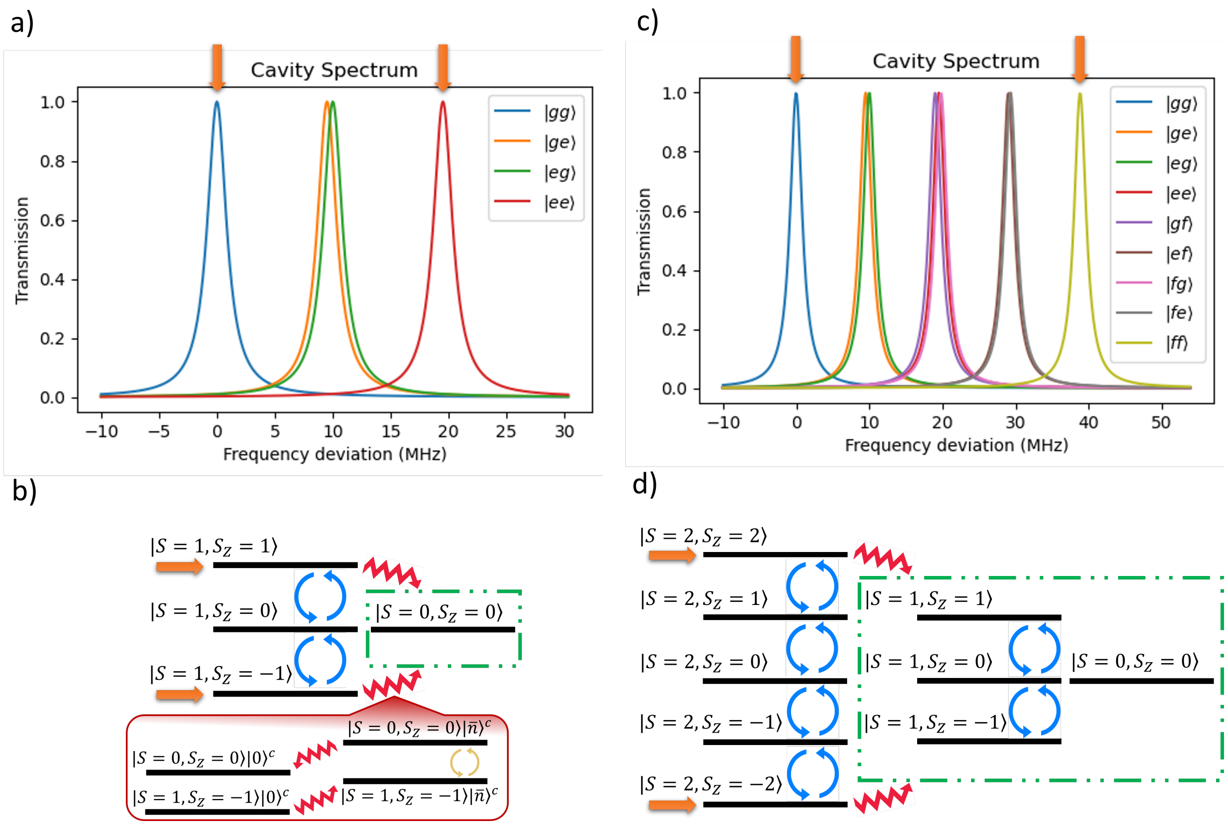

Fig. 3.7: **Scheme of the autonomous feedback protocol**. (a) The cavity spectrum shifted by different two-qubit states, with two cavity probes applied at the frequencies marked by the orange arrows. (b) Hilbert space engineering for the Bell state stabilization scheme [50]. The orange arrows mark the states measured by the two cavity probes shown in (a), and the blue arrows represent the "0-photon drive". The green rectangle encircles the stabilized state, and the zigzag red arrows are dissipative processes steering into the stabilized state, the mechanism of which is shown in the inset circled by the red rectangle. Inset: Realization of the jump operator from state $|gg\rangle$ and state $|ee\rangle$ to the stabilized state. The red arrows are populating and decaying of the cavity photons, and the yellow arrows denote the "n-photon drive". (c) The cavity spectrum shifted by different two-qutrit states, with two cavity probes applied at the frequencies marked by the orange arrows. (d) Hilbert space engineering for the stabilization of two adjacent qutrits into the $S_{\text{total}} \in \{0, 1\}$ subspace. The orange arrows mark the states measured by the two cavity probes shown in (c), and the blue arrows represent the "0-photon drive". The green rectangle encircles the stabilized subspace of $S_{\text{total}} \in \{0, 1\}$, and the zigzag red arrows are dissipative processes steering into the stabilized subspace, with similar mechanism as shown in the inset of (b).

Here $\hbar\chi_j^{\mathrm{A(B)}}$ are the interaction energies between the cavity and qutrit A(B), indicating the cavity resonance frequency's shift summed over that induced by qutrit A and qutrit B, which is depicted in Fig. 3.7 (c). This term also indicates

Inspired by the qubit protocol, the cavity is driven at its resonance frequencies for qutrit states $|gg\rangle$ and $|ff\rangle$, which acts as part of the "pump". With cavity photon number n, the qutrit energy levels are shifted to $\hbar\omega_j^{\mathrm{A(B)}} + n\hbar\chi_j^{\mathrm{A(B)}}$. Here, the three anharmonic energy levels are denoted as $|g\rangle$, $|e\rangle$ and $|f\rangle$, with $\omega_{ef}^{\mathrm{A(B)}} = \omega_f^{\mathrm{A(B)}} - \omega_e^{\mathrm{A(B)}}$, $\omega_{ge}^{\mathrm{A(B)}} = \omega_e^{\mathrm{A(B)}} - \omega_g^{\mathrm{A(B)}}$, $\chi_{ef}^{\mathrm{A(B)}} = \chi_f^{\mathrm{A(B)}} - \chi_e^{\mathrm{A(B)}}$, $\chi_{ge}^{\mathrm{A(B)}} = \chi_e^{\mathrm{A(B)}} - \chi_g^{\mathrm{A(B)}}$, and $\chi_{gf}^{\mathrm{A(B)}} = \chi_f^{\mathrm{A(B)}} - \chi_g^{\mathrm{A(B)}}$. Thus, we apply the "0 photon drive" at $\omega_{ge}^{\mathrm{A(B)}}$ and $\omega_{ef}^{\mathrm{A(B)}}$ simultaneously with the same Rabi frequency Ω^0, while the "n photon drive" is applied at $\omega_{ge}^{\mathrm{A(B)}} + n\chi_{ge}^{\mathrm{A(B)}}$ and $\omega_{ef}^{\mathrm{A(B)}} + n\chi_{ef}^{\mathrm{A(B)}}$ with Rabi frequency Ω^n. The effective drive Hamiltonians are

$$\begin{aligned} \hat{H}_{\mathrm{eff}}^{0} &\propto \hat{S}_x^{\mathrm{A}} \otimes I^{\mathrm{B}} + I^{\mathrm{A}} \otimes \hat{S}_x^{\mathrm{B}}, \\ \hat{H}_{\mathrm{eff}}^{n} &\propto \hat{R}_{gf}^{\mathrm{A}} \otimes I^{\mathrm{B}} - I^{\mathrm{A}} \otimes \hat{R}_{gf}^{\mathrm{B}}, \end{aligned} \tag{3.27}$$

where $\hat{S}_x^{\mathrm{A(B)}}$ are the spin angular momentum operators of the spin-1 particles represented by qutrit A(B), and $\hat{R}_{gf}^{\mathrm{A(B)}}$ are the rotation operator between the $|g\rangle$ state and the $|f\rangle$ state induced by direct two-photon transition on qutrit A(B).

The effective rotation operator $\hat{R}_{\mathrm{eff}}^{0}$ coincides with the total spin angular momentum $\hat{S}_x^{\mathrm{total}}$. Thus, this drive preserves the total spin represented by the two-qutrit system, while it rotates between different eigenstates of the z component for the total spin $\hat{S}_z^{\mathrm{total}}$. Meanwhile, the "$n$-photon drive" does not preserve the total spin and has non-zero components linking states $|gg\rangle|\bar{n}\rangle^{\mathrm{C}}$ and $|ff\rangle|\bar{n}\rangle^{\mathrm{C}}$ to the $|S_{\mathrm{total}} = 0\rangle|\bar{n}\rangle^{\mathrm{C}}$ and $|S_{\mathrm{total}} = 1\rangle|\bar{n}\rangle^{\mathrm{C}}$ subspace. Similar to the process described in Section 3.3.3.1, with those two drives combined, the two-qutrit system undergoes unidirectional evolution into the target subspace. The autonomous feedback loop here provides quantum jump operators from $|gg\rangle$ and $|ff\rangle$ to $S_{\mathrm{total}} \in \{0, 1\}$ subspace, with an overall rate proportional to the cavity linewidth κ. This stabilization process on two qutrits are depicted in Figure 3.7 (d).

Noticing that states $|gg\rangle$ and $|ff\rangle$ represent two spin-1 particles' states $|S^{\text{total}}=2, S_z^{\text{total}}=2\rangle$ and $|S^{\text{total}}=2, S_z^{\text{total}}=-2\rangle$, the drive $\hat{S}_x^{\text{total}}$ thus connects the entire subspace $S_{\text{total}}=2$ with $|gg\rangle$ and $|ff\rangle$. This "0-photon drive", when applied continuously, therefore assists to evacuate the $S_{\text{total}}=2$ subspace, leading to their stabilization into the target subspace where $S_{\text{total}}\in\{0,1\}$. Meanwhile, the drive $\hat{S}_x^{\text{total}}$ has no cross term between the $S_{\text{total}}=2$ subspace and the target subspace, preventing leakage back from the stabilized states. Consequently, the applied drives and dissipations ensure the AKLT state as the fixed point when the protocol is applied on a qutrit chain.

For the above two-qutrit protocol, we simulate the Lindblad master equation in Qutip [12, 13] master euqaton solver,

$$\frac{d}{dt}\rho(t)=-\frac{i}{\hbar}[\hat{\mathrm{H}}(t),\rho(t)]+\kappa\mathbf{D}[\hat{a}]\rho(t)+\sum_{\substack{l=ge,ef\\ j=A,B}}\left(\frac{1}{T_1^{j,l}}\mathbf{D}[\sigma_-^{j,l}]\rho(t)+\frac{1}{2T_\phi^{j,l}}\mathbf{D}[\sigma_z^{j,l}]\rho(t)\right). \quad (3.28)$$

Here, $T_1^{A(B),ge}$ and $T_1^{A(B),ef}$ are the realaxation time from state $|e\rangle$ to state $|g\rangle$ and from state $|f\rangle$ to state $|e\rangle$. The pure dephasing rate is given by,

$$1/T_\phi^{A(B),ge(ef)}=1/T_2^{A(B),ge(ef)}-1/2T_1^{A(B),ge(ef)},$$

where $T_2^{A(B),ge(ef)}$ are the dephasing times between the corresponding two adjacent levels. The Lindblad superoperator for an observable $\hat{O}$ acting on the density matrix ρ is defined as

$$\mathbf{D}[\hat{O}]\rho=\hat{O}\rho\hat{O}^\dagger-\frac{1}{2}\hat{O}^\dagger\hat{O}\rho-\frac{1}{2}\rho\hat{O}^\dagger\hat{O}. \quad (3.29)$$

For the unitary part of system evolution, we have the Hamiltonian,

$$\hat{\mathrm{H}}=\hat{\mathrm{H}}_{\text{system}}+\hat{\mathrm{H}}_{\text{probe}}+\hat{\mathrm{H}}_0+\hat{\mathrm{H}}_n. \quad (3.30)$$

Since we work in the rotating frame for the qutrit transition energies as well as for the center of the cavity resonance frequencies of corresponding to $|gg\rangle$ and $|ff\rangle$, this Hamiltonian consists of

$$\hat{\mathrm{H}}_{\mathrm{system}} = \hbar\left(\frac{\chi_{gf}^{A}}{2}\sigma_z^{A,gf} + \frac{\chi_{ge}^{A}-\chi_{ef}^{A}}{2}|e\rangle^A\langle e|^A + \frac{\chi_{gf}^{B}}{2}\sigma_z^{B,gf} + \frac{\chi_{ge}^{B}-\chi_{ef}^{B}}{2}|e\rangle^B\langle e|^B\right)\hat{a}^\dagger\hat{a}, \quad (3.31)$$

$$\hat{\mathrm{H}}_{\mathrm{probe}} = 2\hbar\varepsilon_C\cos\left(\frac{\chi_{gf}^{A}+\chi_{gf}^{B}}{2}t\right)\left(\hat{a}+\hat{a}^\dagger\right), \quad (3.32)$$

$$\hat{\mathrm{H}}_0 = \hbar\Omega^0\left(\sigma_x^{A,ge}+\sigma_x^{A,ef}+\sigma_x^{B,ge}+\sigma_x^{B,ef}\right), \quad (3.33)$$

and,

$$\hat{\mathrm{H}}_n = \hbar\Omega^n\left(\cos\left(n\frac{\chi_{gf}^{A}+\chi_{gf}^{B}}{2}t\right)\left(\sigma_x^{A,gf}-\sigma_x^{B,gf}\right) - \sin\left(n\frac{\chi_{gf}^{A}+\chi_{gf}^{B}}{2}t\right)\left(\sigma_y^{A,gf}-\sigma_y^{B,gf}\right)\right). \quad (3.34)$$

Here ε_C is the amplitude of the cavity probe with $\varepsilon_C = \kappa\sqrt{n}/2$. The qutrit operators are defined similarly to the qubit case, where $\sigma_+^{ge} = |e\rangle\langle g|$, $\sigma_-^{ge} = |g\rangle\langle e|$, $\sigma_+^{gf} = |f\rangle\langle g|$, $\sigma_-^{gf} = |g\rangle\langle f|$, $\sigma_+^{ef} = |f\rangle\langle e|$, and $\sigma_-^{ef} = |e\rangle\langle f|$. Thus we have $\sigma_x^{ge/ef/gf} = \sigma_+^{ge/ef/gf} + \sigma_-^{ge/ef/gf}$, $\sigma_y^{ge/ef/gf} = i\left(\sigma_+^{ge/ef/gf} - \sigma_-^{ge/ef/gf}\right)$, as well as $\sigma_z^{gf} = -|g\rangle\langle g| + |f\rangle\langle f|$. The parameters we used for the cavity-qutrit interaction term and the cavity linewidth are shown in the first line of Table 3.1. The T_1s and T_2s are set to optimistically large values of 500 μs, so that these decay channels contribute negligibly to the dynamics. The Rabi frequencies for the "0 photon drive" and the "n photon drive" are chosen as $\Omega^0 = \kappa/2$ and $\Omega^n = \kappa$ for optimization.

As is shown in Fig. 3.8(a), an adjacent pair of qutrits is initialized in a maximally mixed state of the nine-dimensional Hilbert space. The system then evolves under the driven dissipative protocol which consists of always-on drives. For the qutrit pair, all five states representing $S_{\mathrm{total}} = 2$ have their state population converging to zero throughout the protocol, while the four states in subspace $S_{\mathrm{total}} \in \{0, 1\}$ are preserved and stabilized. The protocol effectively eliminates the $S_{\mathrm{total}} = 2$ subspace while steering the system into the $S_{\mathrm{total}} \in \{0, 1\}$ subspace. Figure 3.8(b) shows the total four state population in subspace

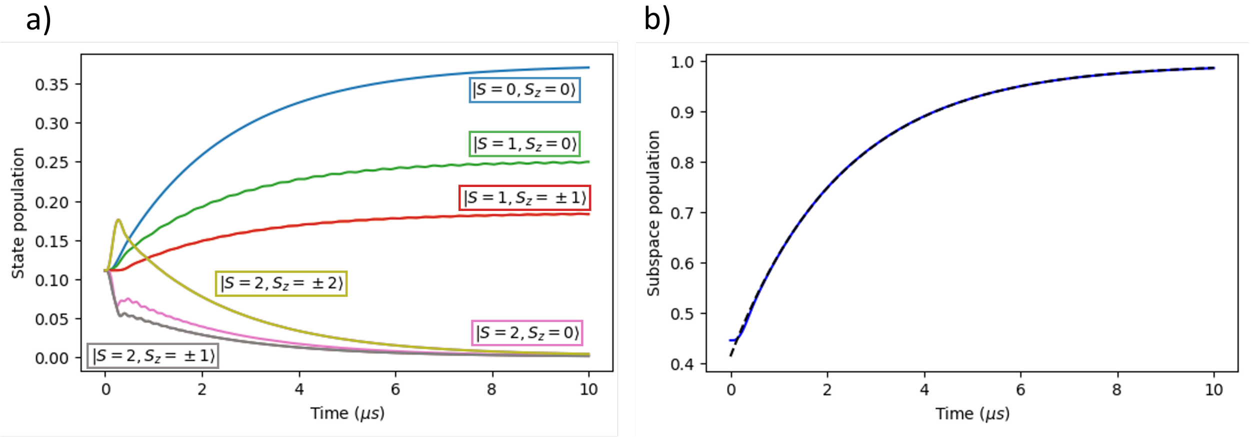

Fig. 3.8: Performance of the autonomous feedback protocol for two qutrits. (a) Stabilization process for one pair of neighboring qutrits, with the entire subspace $S_{\text{total}} = 2$ eliminated and subspace $S_{\text{total}} \in \{0, 1\}$ stabilized. The colored lines are the state populations for eigenstates of both $\hat{S}_{\text{total}}$ and $\hat{S}^z_{\text{total}}$. b) The blue line represents the change of total population in the targeted subspace where $S_{\text{total}} \in \{0, 1\}$. The black dotted line is an exponential fit.

$S_{\text{total}} \in \{0, 1\}$, which is the two-qutrit AKLT subspace. For stabilization time from about 500 ns, the curve can be well fitted with an exponential function $y = Ae^{-bx} + C$. The fitting parameter C is extracted as the final fidelity of the target subspace and b as the stabilization rate, with the convergence time for the protocol calculated as $1/b$.

3.4 Protocol performance with system scaling up

3.4.1 Numerical simulations

We thus generalize the two-qutrit protocol described in Section 3.3.3.2 to the system consisting N qutrits. Since the AKLT Hamiltonian is frustration-free, as the system scales up, the protocol applies two-qutrit dissipative processes to each adjacent pairs of qutrits. As the protocol is applied to a 1-D qutrit chain containing N qutrits, the Lindblad master equation

	$\chi_{ge}/2\pi$	$\chi_{gf}/2\pi$	$\chi'_{ge}/2\pi$	$\chi'_{gf}/2\pi$	$\kappa/2\pi$
Base parameters used in all simulations	40.00	79.20	38.00	76.00	2.00
Ideal “target” parameters	40.00	80.00	40.00	80.00	2.00
Cavity 1 mismatched 10% from target	43.64	87.81	39.67	87.81	1.93
Cavity 2 mismatched 10% from target	36.66	79.83	39.87	79.83	1.99
Cavity 3 mismatched 10% from target	41.52	76.96	42.79	76.96	1.94

Tab. 3.1: The cavity-qutrit interaction parameters and the cavity linewidth for one cavity in the chain. (Unit: MHz) Line 1: The base parameters we choose for simulating two-qutrit as well as multi-qutrit protocol performance in the article, except in Fig. 3.11(b). This set of base cavity parameters already holds a little bit mismatch within 5% from the ideal “target” parameters. Line 2: The ideal device parameters as the target of device fabrication processes. This set of parameters is the reference for generating the mismatching parameter. Line 3-5: The mismatched cavity parameters for a four-qutrit chain with its three cavities, the parameter deviations are randomly generated within 10 percent deviation from the ideal values. Such deviations are enlarged proportionally for generating the 20%, 30% and 40% mismatching parameters as given in Fig. 3.11b.

becomes

$$\frac{d}{dt}\rho(t) = -\frac{i}{\hbar}[\hat{\mathrm{H}}(t),\rho(t)] + \sum_{j=1}^{N-1}\kappa_j\mathbf{D}[\hat{a}_j]\rho(t) + \sum_{\substack{j=1\\ l=ge,ef}}^{N}\left(\frac{1}{T_1^{j,l}}\mathbf{D}[\sigma_-^{j,l}]\rho(t) + \frac{1}{2T_\phi^{j,l}}\mathbf{D}[\sigma_z^{j,l}]\rho(t)\right), \tag{3.35}$$

given that $\mathbf{D}[\hat{O}]\rho = \hat{O}\rho\hat{O}^\dagger - \frac{1}{2}\hat{O}^\dagger\hat{O}\rho - \frac{1}{2}\rho\hat{O}^\dagger\hat{O}$, with the Hamiltonian terms where $\hat{\mathrm{H}} = \hat{\mathrm{H}}_{\text{system}} + \hat{\mathrm{H}}_{\text{probe}} + \hat{\mathrm{H}}_0 + \hat{\mathrm{H}}_n$,

$$\hat{\mathrm{H}}_{\text{system}} = \hbar\sum_{i=1}^{N-1}\left(\frac{\chi^i_{gf}}{2}\sigma_z^{i,gf} + \frac{\chi^i_{ge}-\chi^i_{ef}}{2}|e\rangle^i\langle e|^i + \frac{\chi'^{\,i}_{gf}}{2}\sigma_z^{i+1,gf} + \frac{\chi'^{\,i}_{ge}-\chi'^{\,i}_{ef}}{2}|e\rangle^{i+1}\langle e|^{i+1}\right)\hat{a}_i^\dagger\hat{a}_i, \tag{3.36}$$

$$\hat{\mathrm{H}}_{\text{probe}} = 2\hbar\sum_{i=1}^{N-1}\varepsilon_C^i\cos\left(\frac{\chi^i_{gf}+\chi'^{\,i}_{gf}}{2}t\right)\left(\hat{a}_i+\hat{a}_i^\dagger\right), \tag{3.37}$$

$$\hat{\mathrm{H}}_0 = \hbar\Omega^0\sum_{i=1}^{N}\left(\sigma_x^{i,ge}+\sigma_x^{i,ef}\right), \tag{3.38}$$

and,

$$\hat{\mathrm{H}}_n = \hbar \sum_{i=1}^{N-1} \Omega_i^n (-1)^{i-1} \left(\cos\left(n \frac{\chi_{gf}^i + \chi_{gf}'^{\,i}}{2} t \right) (\sigma_x^{i,gf} - \sigma_x^{i+1,gf}) - \sin\left(n \frac{\chi_{gf}^i + \chi_{gf}'^{\,i}}{2} t \right) (\sigma_y^{i,gf} - \sigma_y^{i+1,gf}) \right). \tag{3.39}$$

Here $\chi^i_{ge/gf/ef}$ and $\chi'^{\,i}_{ge/gf/ef}$ are the cavity shifts on the i_{th} cavity induced by the i_{th} and the $(i+1)_{th}$ qutrit, and $\hat{a}_i(\hat{a}_i^\dagger)$ is the annihilation(creation) operator for the i_{th} cavity. With κ^i being the cavity linewidth of the i_{th} cavity, we apply the probe strength for this cavity $\varepsilon_C^i = \kappa^i \sqrt{n}/2$. The terms $\sigma_{x,y,z}^{i,ge/ef/gf}$ are the qutrit matrices for the i_{th} qutrit. The "0 photon drive", Ω^0, is chosen to be $\sum_{i=1}^{N-1} \kappa^i/2(N-1)$ and the "n photon drive", Ω_i^n, is chosen to be κ^i. The qutrit-cavity parameters and cavity linewidths are assumed to be the same for each cavity, equivalent to the two-qutrit case, which is shown in the first line of Table 3.1.

For the qutrit number $N_{\text{sites}} \leq 3$, we use the Qutip master equation solver to obtain the time evolution of the expectation value for the AKLT subspace projector. For $N_{\text{sites}} = 4$, the Monte Carlo solver is chosen for its better performance in case of large dimensional Hilbert spaces. In the latter solver, the equivalence to the system evolution under the master equation is obtained by stochastically calculating the trajectories for quantum jumps. The parameter settings are shown in the first line of Table 3.1, with general ratio between χ_{ge} and κ around 20. Table 3.1 displays the dispersive shifts and cavity linewidths used for the simulations. To ensure that our results do not hinge on perfect parameter matches, we performed all simulations with "base parameters" that were near to what might be considered ideal. The base parameters, and the "target" parameters are given in the first two lines of the table. The base parameters are used for the simulations displayed Fig. 3.8, Fig. 3.10, and Fig. 3.12 (a), (c), (d).

For optimization of the simulation process, it is desirable to make a cutoff at the maximal cavity photon population at the lowest value possible while maintaining accurate results. As is presented in Fig. 3.9, we thus monitored the cavity photon number population throughout the same stabilization process shown in Fig. 3.8. With the ground state or the maximally

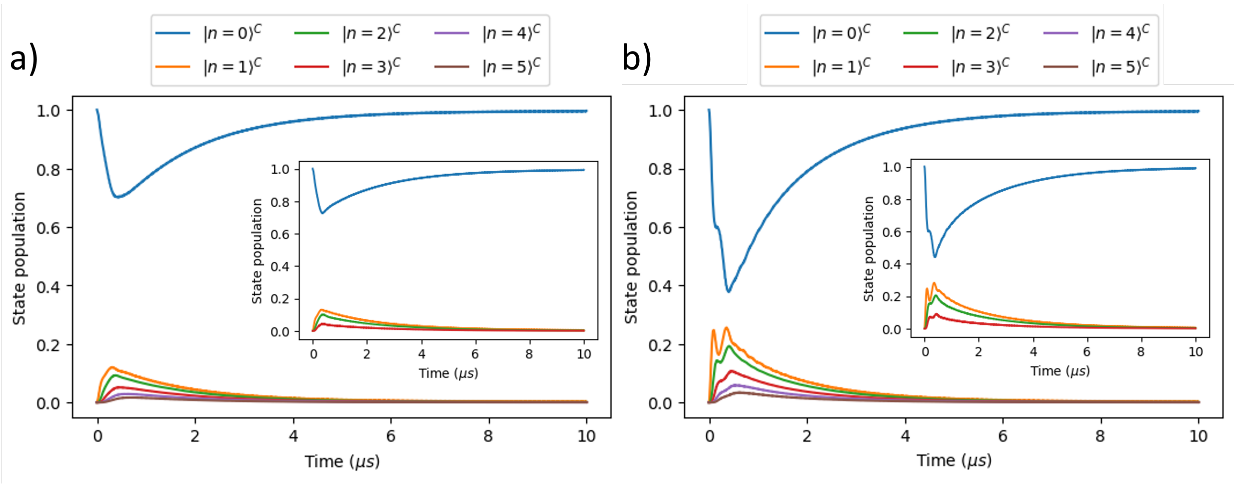

Fig. 3.9: Cavity photon population during the stabilization process. (a) The system is initialized with a fully mixed state and then evolves under the protocol. (b) The system is initialized in the ground state. Insets show the stabilization process calculated with a maximal photon number cutoff of $n = 3$ instead of $n = 9$.

mixed state unidirectionally projected into the $S_{\text{total}} \in \{0, 1\}$ subspace, the cavity photon number ramps up in about the first 500 ns and then decays monotonically. Whichever initial state we chose, the cavity photon numbers for $n \geq 4$ are quite small throughout the stabilization process. Actually, the behaviour of cavity photon number $n \in \{0, 1, 2, 3\}$ makes up 90 percent of the cavity state population, thus enabling representative description of the overall system behaviour with limited photon numbers. Consequently, we make a reasonable cutoff of the cavity photon population $n \leq 3$, with which the simulation results are shown in the insets of Fig. 3.9 (a), (b). By comparing the insets of Fig. 3.9 (a), (b) (with $n \leq 3$) to the main panels (with $n \leq 9$) we see very similar photon number dynamics further confirming that a simulation cuttoff of $n \leq 3$ produces accurate results.

Extended from the two-qutrit case, we study the evolution of the system with 2, 3 and 4 sites in the AKLT chain. We consider two initial preparations: either an AKLT state or the product state of single-qutrit undriven ground states, $|g\rangle$. The evolution of the populations in the AKLT subspace under the protocol is shown in Fig. 3.10 (a). While stabilization of the AKLT state is observed, the final fidelity decreases and the converging time increases for

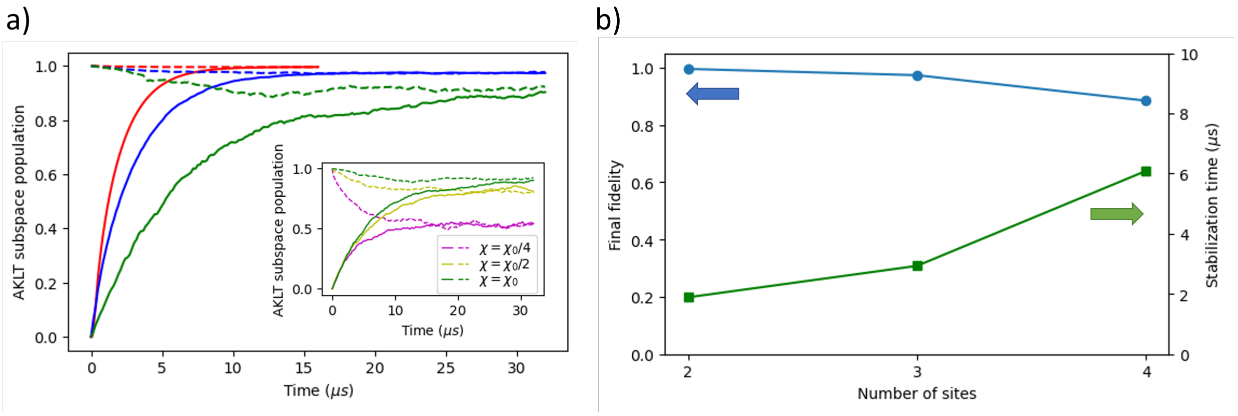

Fig. 3.10: Performance of the autonomous feedback protocol with the qutrit chain scaling up. (a) Starting from the qutrits ground state $|g \dots g\rangle$ (solid colored lines) and starting within the AKLT subspace (dashed colored lines), we simulate the time evolution of the OBC AKLT subspace population under the driven dissipative protocol with $N_{\text{sites}} = 2$ (red), $N_{\text{sites}} = 3$ (blue) and $N_{\text{sites}} = 4$ (green) for comparison. Inset: The four qutrit time evolution under the stabilizing protocol in terms of the system population in the AKLT subspace, with the cavity shift scaling as χ_0, $\chi_0/2$ and $\chi_0/4$. (b) Extracted fitting parameters as the final fidelity and the convergence time. The blue dots represent the varied final fidelity with systems of two, three and four qutrits (left axis), and the green dots represent the convergence time for the protocol (right axis).

larger chains. Analyzing the simulation results, we now extract the protocol's performance as fitted parameters from the exponential function. The stabilization time, as well as final fidelity, are calculated according to Section 3.3.3.2 and presented in Figure 3.10, evaluating the effectiveness of the scaled protocol.

3.4.2 Fidelity of the AKLT subspace

3.4.2.1 Finite ratio between cavity shift and cavity linewidth

In the two-qubit autonomous feedback protocol introduced in Section 3.3.3.1, as is shown in Fig. 3.7 (a), when $\chi \gg \kappa$, the density of states corresponding to $|ge\rangle$ and $|eg\rangle$ is highly suppressed at the applied cavity drive frequencies. However, if χ/κ is finite, as is expected in any reasonable experimental realization, a difference in dispersive shifts ($\chi_{\mathrm{A}} \neq \chi_{\mathrm{B}}$) results in different amplitudes in the tails of the Lorentzian cavity spectrum lineshapes. This difference distinguishes the $|ge\rangle$ and $|eg\rangle$ states, corresponding to a measurement of the qubits in those bases. This residual measurement therefore dephases the $|\phi_{-}\rangle$ state, mixing the state populations of the stabilized state $|\phi_{-}\rangle$ and the eliminated state $|\phi_{+}\rangle$, and thus reducing the fidelity of the autonomous feedback scheme. Considering the scaling between the rate of this residual measurement and the stabilizing rate to the target Bell state, such a reduction in fidelity can be significant for a large discrepancy between χ_{A} and χ_{B}. Hence, for optimal operation, the two-qubit scheme requires $\chi_{\mathrm{A}} \simeq \chi_{\mathrm{B}}$, as this can be experimentally achieved with frequency tunable qubits.

However, when it comes to the two-qutrit protocol introduced in Section 3.3.3.2, where the stabilized subspace is four-dimensional, such discrepancies in the cavity spectrum shifted by the stabilized states are unavoidable, even with full tunabilities on the device parameters. Thus, as is discussed above, the overlaps between the peaks in Fig. 3.7 (c) can cause redundant measurements, compromising the fidelity of the target state. Actually, finite χ/κ becomes one of the main limiting factors for the final fidelity when we consider ideal relaxation and dephasing time of single qutrits. For the N qutrit protocol performance shown in

Fig. 3.10, the decrease in final fidelity due to the finite value of χ/κ is explored in the inset of Fig. 3.10(a). Here we plot the AKLT state population starting from the AKLT state or the ground state with cavity shifts χ given as χ_0, $\chi_0/2$ and $\chi_0/4$. With the cavity linewidth κ kept unchanged, smaller χ brings much more dephasing out of the AKLT subspace and hinders more on the final fidelity of the protocol. On the contrary, increasing χ/κ reduces such effect brought by redundant measurement via smaller overlaps between peaks of the shifted cavity spectrum. However, reasonable values of χ/κ can not be infinitely large in experiment realizations. One limitation is set on χ by the dispersive condition. In the dispersive limit, the ratio between the coupling strength and the detuning, g/Δ should be small enough, while we wish to achieve high value of $\chi = g^2/\Delta$. This indicates a requirement for large value of the coupling strength, which is finitely achievable and may evoke complicated nonlinear terms. The other limitation is set on κ. Since the cavity linewidth κ decides the rate of evacuating and ramping of the cavity photon population, the converging time of the protocol is proportional to κ. Thus, increasing the value of χ/κ by reducing κ will increase the protocol converging time, giving less fidelity in the presence of local noise.

Hence, here we have more detailed analysis of the redundant measurement caused by finite χ/κ. In the strong dispersive limit, we have the relation $\chi \gg \kappa$ for the cavity-qutrit coupling parameters. The cavity resonance amplitude, $T = 1/(1+x^2)$, is of a Lorentzian spectral line shape, which is presented in Fig. 3.7 (a) as well as in Fig. 3.7 (c). Here $x = 2(\omega - \omega_r)/\kappa$ and ω_r is the cavity resonance frequency. Thus, as we probe the system at one of the peaks, there is a high ratio between the resonance amplitudes for probed and unprobed states. However, with relatively long protocol time, a small resonance amplitude still causes residual measurements that distinguishes between stabilized two-qutrit states. Those small extra measurement terms induced by the probe, as introduced in Section 3.3.3.2, have a visible effect on the final fidelity of the stabilization for the manybody entangled state, as is shown in the inset of Figure 3.10(a) and Figure 3.12 (a). If we initialize the system in one of the open boundary AKLT states, and perform the “0 photon drives” as well as the

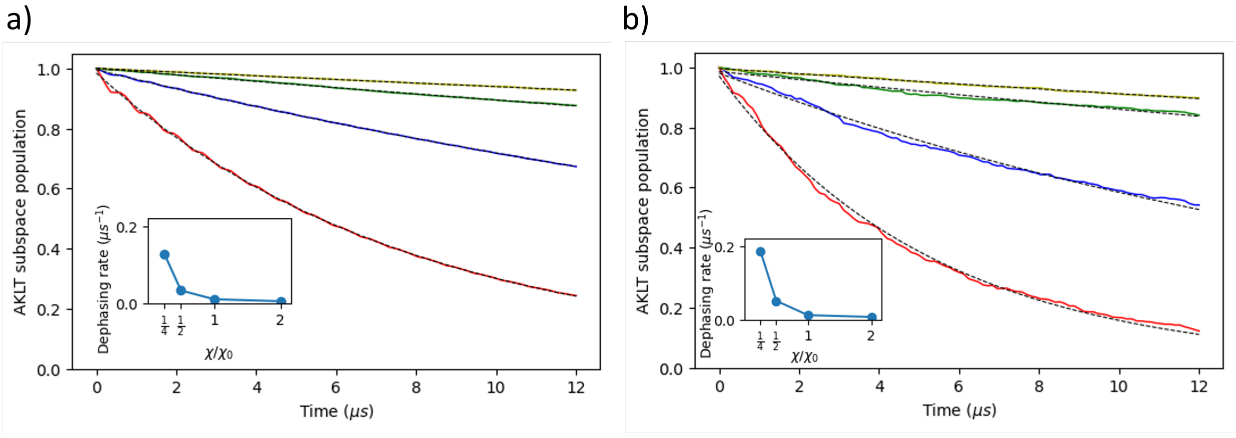

Fig. 3.11: Dephasing out of the AKLT subspace due to extra measurements caused by the cavity probes. a(b) Initialized with a three(four) qutrit AKLT state, the system dephases under the "0-photon drives" and the cavity probes, with qutrit induced cavity shift set as $\chi = \chi_0/4$ (red), $\chi = \chi_0/2$ (blue), $\chi = \chi_0$ (green) and $\chi = 2\chi_0$ (yellow). The AKLT subspace population curves are fitted with exponential functions. Insets display the extracted dephasing rate of the system versus the relative cavity shift χ/χ_0.

measurement probe, in ideal case there shouldn't be any leakage out of the AKLT subspace. However, in the existence of the redundant measurement, especially when the χ value is small, the AKLT state dephases out of the AKLT subspace with a fixed dephasing rate. Figure 3.11 shows the simulation result with qutrit number $N_{\text{site}} = 3$ and $N_{\text{site}} = 4$. The decreases in the AKLT subspace population are fitted with exponential functions $y = Ae^{-bx} + C$ for fixed C. And the extracted dephasing rates b are plotted in the insets of Figure 3.11, showing that the decay rate grows significantly as χ is decreased.

There are two possible routes to mitigate this effect within expeirmentally achievable conditions. One is working in the so-called straddling regime for transmon circuits[3], where large χ may be achieved with limited value of coupling strength. The other is the "partial measurement filter" introduced in chapter 4, which changes the shapes of resonance peaks in the cavity spectrum. On current platforms, we can expect efficient stabilization as long as the residual measurement induced dephasing is reduced to some negligible level compared to the intrinsic dephasing and relaxation of the superconducting qutrits.

3.4.2.2 Parameter mismatch between designing and fabrication

Then, for the case of a four qutrit chain with three cavities described in Section **??**, we use the pseudo-random number generator in Python to generate deviations of 10% to the standard expected device parameters, as is shown in the third to fifth lines of Table 3.1. Notice that the deviations for each pair of χ^i_{gf} and $\chi'^{\,i}_{gf}$ are always assigned with the same random number. For the case of 20%, 30% and 40% mismatch, we enlarge the parameter deviations generated for the 10% case proportionally based on the ideal "target" device parameters.

In Fig. 3.11b we display simulation results where the neighboring qutrits and cavities have mismatched parameters. With an overall control of the the Josephson inducductance, we can assume that perfect matching between χ^i_{gf} and $\chi'^{\,i}_{gf}$ can be achieved for each cavity i and its two coupled qutrits i and $i+1$, via flux tuning on the qutrits. Other parameters, including the qutrit-cavity interaction term and the cavity linewidth, are mismatched. These parameters are given in lines 3-5 of Table 3.1. For larger mismatches displayed in Fig. 3.11b, the deviations are simply scaled accordingly.

3.4.2.3 Limited relaxation and dephasing time of single qutrit

From the results displayed in Fig. 3.10(a) we can extract the final fidelity and stabilization time for different size chains, which we display in Fig. 3.10(b) and Fig. 3.11(a). We note that the final fidelity decreases with size of the chain, and the stabilization time increases.

In actual experiments, the qutrits are not perfectly realizable as in the model simulated above. For example, there is limited control precision over the qutrit-cavity coupling parameters. In the above simulations, we assume that the cavity frequency shifts induced by qutrits are approximately equivalent, with discrepancies smaller than 5 percent. This relation requires equally spaced cavity frequency shifts from qutrit states $|g\rangle$, $|e\rangle$ and $|f\rangle$, as well as equal cavity-qutrit interaction terms among different qutrits. Such an assumption for the sake of simplicity, but are difficult to meet in experiments.

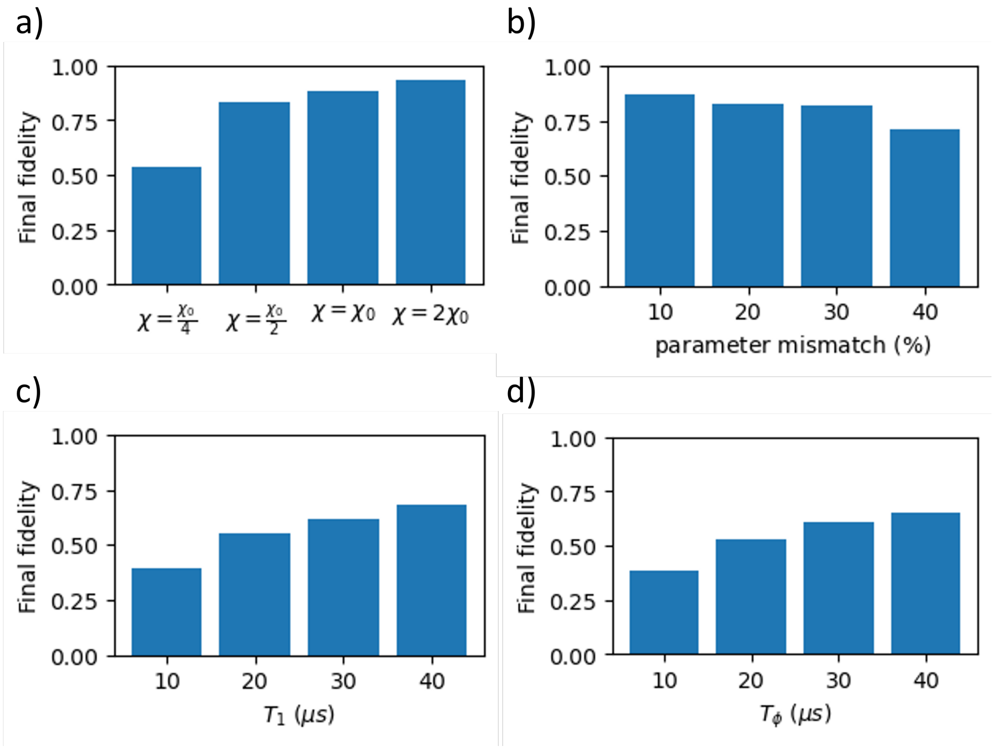

Fig. 3.12: Fidelity in the four-qutrit AKLT subspace estimated under experimental imperfections. (a) The impact of finite χ compared to κ. (b) Running the protocol with mismatched device parameters. (c,d) Evaluating the protocol fidelity under the dissipation channel with finite qutrit T_1/T_ϕ between adjacent levels.

In the experimental realization with transmon qubits [50] matching between the cavity shift of qubit A and B, $\chi_{\mathrm{A}} = \chi_{\mathrm{B}}$, was achieved by tuning the qubit frequencies, where $\chi_{\mathrm{A(B)}} \propto g^2_{\mathrm{A(B)}}/(\omega_{\mathrm{A(B)}} - \omega_r)$ with g noting the coupling strength. However, for the current protocol involving qutrits, matching all the dispersive shifts by simple frequency tuning of the qutrit levels is not possible. A remnant mismatch between dispersive shifts leads to extra dephasing induced by residual measurements, which can nevertheless be eliminated by a higher ratio of χ/κ, as is described in Appendix A. Figure 3.11 (b) shows the protocol fidelity on a four-qutrit chain with mismatched qutrit-cavity coupling parameters to varied degrees, for which the choice of device parameters are introduced in Appendix B. The final fidelity of the protocol decreases slowly from $\sim 85\%$ to $\sim 70\%$ with larger parameter mismatches from 10% to 40%, indicating a relatively small impact on the protocol performance.

The other aspect of imperfect qutrits considers their intrinsic relaxation and dephasing. In previous numerical simulations, we set the qutrit T_1 and T_2 at an optimistically high level ($T_1 = T_2 = 500\ \mu$s) for isolating the protocol performance from the effects brought up by extra environmental coupling. However, in realistic setups, the relaxation towards the ground state of each single qutrit, as well as the decoherence between qutrit levels, will drive the manybody system out of the AKLT subspace, impairing the effectiveness of the protocol. Nevertheless, we find that the driven dissipative protocol is still able to stabilize the system coherence far beyond the single qutrit coherence time, showing its robustness. As is shown in Fig. 3.11 (c/d), the final fidelity in the AKLT susbpace is extracted for finite values of T_1 and T_ϕ between adjacent qutrit levels. With T_1 or T_ϕ solely set to a finite value from 10 μs to 40 μs, the protocol final fidelity increase from $\sim 40\%$ to $\sim 70\%$. Compared to the $3^4 = 81$ dimensions of the four-qutrit Hilbert space, this result further confirms the ability of a driven-dissipative method to keep manybody coherent states far beyond their relaxation or dephasing time.

3.5 Designed experimental setups

We finalize our chip design as an extended scheme of Fig. 3.2 (c), as is shown in Fig. 3.13 (a). We propose an experimental design that can be realized with state of the art fabrication capabilities, as a proof of principle of our scheme, which is shown in Fig. 3.13 (b). Each qutrit is attached to a flux line and a control line, where the qutrit frequencies can be tuned and the qutrit rotations can be applied. For the microwave cavity coupled to each adjacent pair of qutrits, there is a drive line to apply probes to the shared cavity. The shared cavities can also be utilized for state readout to perform quantum state tomography for the verification of the AKLT state stabilization.

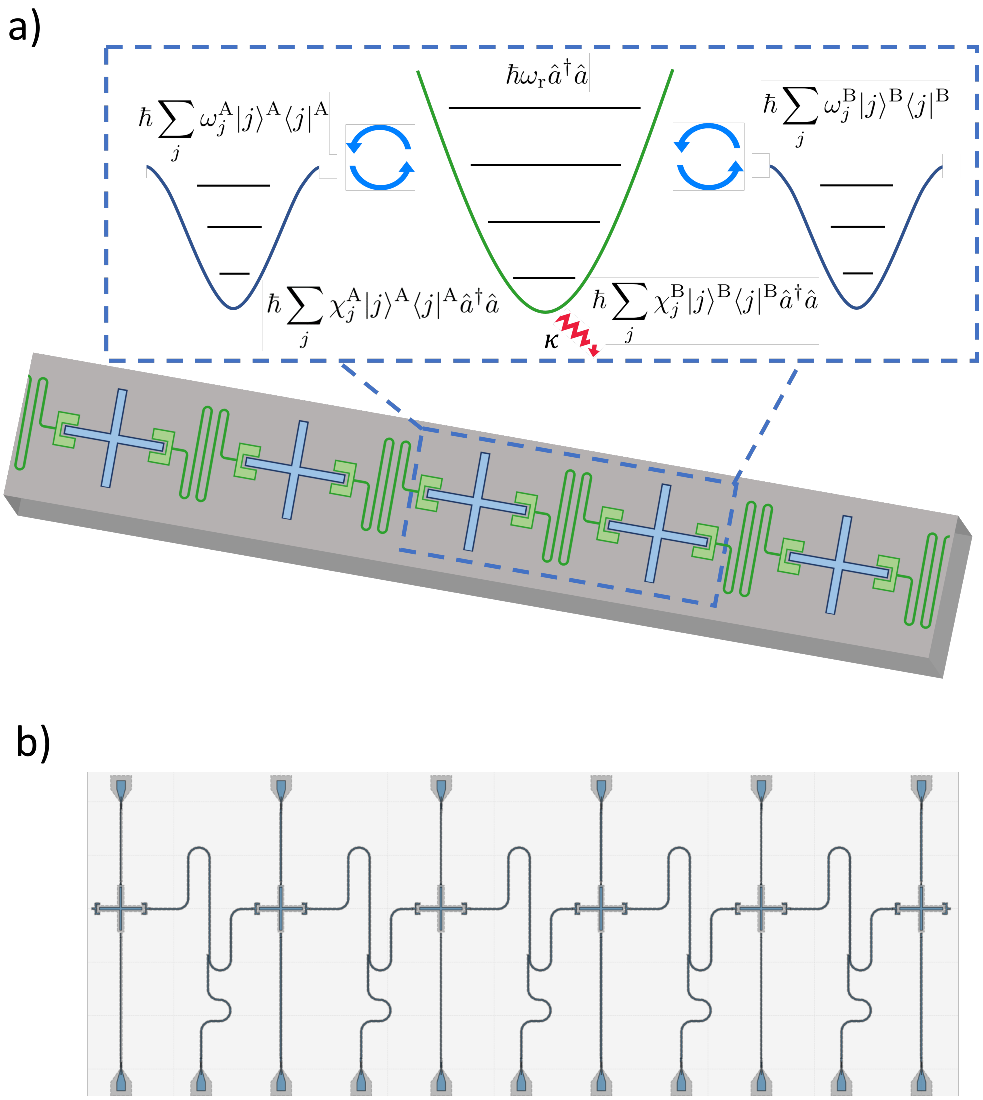

Fig. 3.13: Designed experimental layout (a) Sketch of the proposed one-dimensional superconducting transmon array, with shared resonators between nearest neighbors. Using this platform we present a protocol for the dissipative preparation and stabilization of the system in the AKLT subspace. (b) A chip design by Qiskit metal, with a flux line and a control line for each tunable transmon qutrit, and a readout lline for each linear cavity.

Chapter 4

Toolbox for dissipative quantum protocols

4.1 Setbacks of the partial measurement

In both of the above protocols, we have partial measurements, where we distinguish one system state over the others through dispersive coupling to a linear cavity. However, inherited from the two qubit measurement, this method may still cause intrinsic imperfections from unwanted measurements between the states that are not supposed to be distinguished. For example, in the experiment introduced in Chap. 3, for a qutrit dispersively coupled to a cavity, the measurement induced dephasing between state $|e\rangle$ and $|f\rangle$ is desirable, while the dephasing between $|g\rangle$ and $|e\rangle$ is to be avoided. Similarly, in the protocol introduced in Chap. 4, the two-qutrit states $|gg\rangle$ and $|ff\rangle$ are to be measured, while the residual measurements between other states hinder the scalability of the protocol. Such effects can generally be eliminated by increasing the ratio between the cavity shift χ and the cavity linewidth κ. However, increasing χ requires larger coupling coefficient g or lower detuning between the cavity and the qutrits, which may invalidate the dispersive limit. Also, decreasing κ makes the readout process slower or results in less efficient autonomous feedback protocols. Thus, within the theory and simulation of the dispersive limit, we try to design a "filter" for partial measurement that only allows one state to be distinguished from the others, but filters out the unwanted measurement and corresponding dephasing between all other states.

4.2 Classical picture of a bandpass Purcell filter

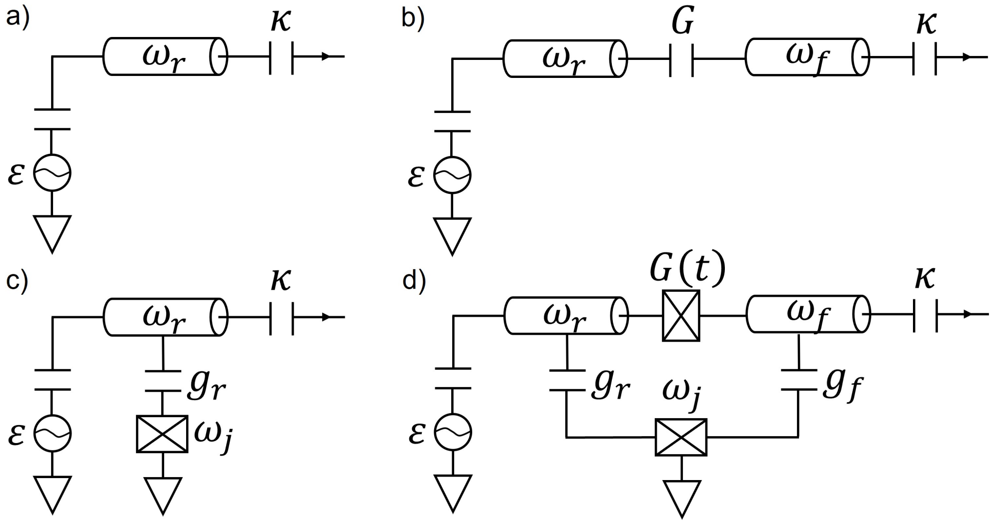

Fig. 4.1: Diagram of the circuit. (a) A standard resonance cavity (b) Two identical cavities with capacitive (or inductive couplings), with drive applied to the "resonance cavity" and coupling to the enviroment given in the "filter cavity". (c) A standard resonance cavity dispersively coupled to a qutrit for readout. (d) The resonance cavity and the filter cavity couples to the qutrit dispersively at the same time. The readout is only obtained at the output port of the filter cavity.

As introduced in Chap. 2 and Chap. 3, the partial measurement over one system state takes place when the cavity spectrum peak corresponding to that state is probed. As the condition required for this measurement process, the cavity frequency shift χ induced by qudit states have to be much larger than the cavity linewidth κ. In this case, the cavity photon population for the rest of the Hilbert space becomes correspondingly small with the cavity transmission $T \propto \kappa^2/\chi^2$ and thus indistinguishable in the limit $\chi/\kappa \to \infty$. However, as is discussed in Chap. 3, when the protocol involves long time continuous measurement for the autonomous feedback, those small residual measurements are theoretically expected to come into effect, and will have an obvious impact on the final fidelity of the protocol. Thus, what we want is elimination of the Lorentzian spectrum tails at the measurement probe frequency for the states that are not supposed to be measured.

Here we consider, semiclassically, the bandpass Purcell filter design in previous work [69], which is shown in figure 4.1. With figure 4.1 (a), we know that the cavity evolves as

$$\dot{\alpha} = -i\Delta_{rd}\alpha - i\varepsilon - \frac{\kappa}{2}\alpha.$$

Here Δ_{rd} is the detuning between the drive and the cavity frequency. Then for the the design in Fig. 4.1 (b), with the resonance cavity and filter cavity inductively coupled, the cavity evolves as

$$\beta = \frac{-iG^*}{\kappa/2 + i\Delta_{fd}}\alpha,$$

and

$$\dot{\alpha} = -i(\Delta_{rd} + \delta)\alpha - i\varepsilon - \frac{\kappa_{\text{eff}}}{2}\alpha,$$

$$\kappa_{\text{eff}} = \frac{4|G|^2}{\kappa}\frac{1}{1 + (2\Delta_{fd}/\kappa)^2},$$

$$\delta = -\frac{\Delta_{fd}}{\kappa}\kappa_{\text{eff}}.$$

Here $\Delta_{rd(fd)}$ is the detuning between the drive and the resonance (filter) cavity frequency. We assume that $\omega_r \sim \omega_f$. For this resonance cavity, we examine its behaviour when the drive frequency is far away from both the resonance cavity frequency and the filter cavity frequency, $\Delta_{fd/rd} \gg \kappa$. Since κ_{eff} and $\delta\omega$ goes to zero with larger Δ_{rd} and Δ_{fd}, the static $\alpha = -i\epsilon_r/(i(\Delta_{rd} + \delta\omega_r) + \kappa_{\text{eff}}/2)$. It has $|\alpha|^2 \propto 1/\Delta_{rd}^2$. So, the filter cavity has $|\beta|^2 \propto 1/\Delta_{fd}^2\Delta_{rd}^2$. Since information is only read out through the filter cavity, the dephasing goes into the same trend, eliminating this Lorentzian tail to the square of its original ratio. Meanwhile, when the drive is on resonance, such as $\Delta_{rd} = \Delta_{rf} = 0$, the cavity's amplitude is still good for making readout. This behaviour and its comparison to a standard resonance frequency is shown in Fig. 4.2.

To point out, when the cavity frequency is shifted away by the qutrit, the filter frequency

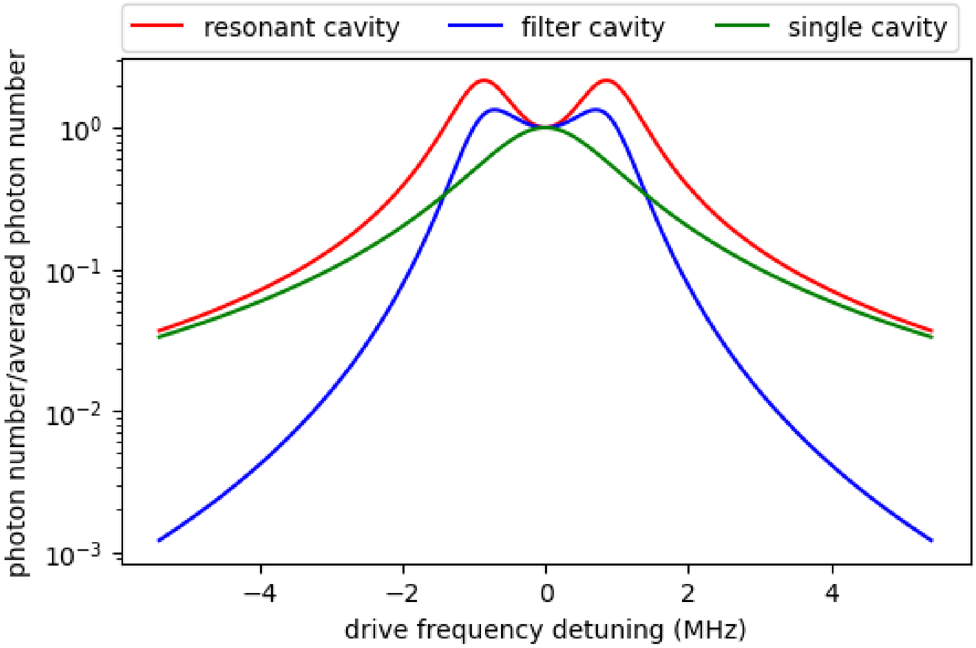

Fig. 4.2: Cavity transmission. The cavity transmission spectrum of the cavity design in Fig. 4.1. The green line is the normal cavity design in a). The red and blue lines are the resonance amplitude for the resonance cavity (ω_r) and filter cavity (ω_f). We can observe that, with good correspondence to the semi-classical predictions, ω_r has the same Lorentzian tail as the normal cavity, but in ω_f, such tail behaviour is high suppressed. This is what we want since the readout amplitude is just proportional to the photon number in the filter cavity.

should also be shifted away. Or else, no elimination will be achieved. For this reason, in our design we connnect the qutrit to both the resonance and the filter cavities. Let's assume the cavity shift from state $|g\rangle$ to state $|e\rangle$ is χ, then as $\chi \gg \kappa$, we have the cavity amplitude $\propto 1/\chi^4$ rather than $\propto 1/\chi^2$. Likely, a normal $\lambda/4$ purcell filter eliminate the cavity transmission at a certain fixed frequency, no matter how the cavity resonance frequency shifts. That means, if we design the $\lambda/4$ purcell filter for a dip in the transmission line for state other than $|gg\rangle$ and $|ff\rangle$, such a dip will interfere with the cavity resonance peak, making the measurement probe invalid. Thus, a shift in the working frequency of the Purcell filter will be also required.

4.3 Dispersive limit of a cavity-qutrit-cavity system

Here we apply a full quantum analysis of the system consisting two cavities and a qutrit, within the dispersive limit. Let's assume ω_r and ω_f as the resonant frequencies for the resonance resonator and the filter resonator. They are both dispersively coupled to a qutrit with energy levels $\hbar\omega_i$, separately with strength g_r and g_f. After rotating wave approximation, the system Hamiltonian will be,

$$\begin{aligned}
&\hat{H} = \hat{H}_0 + \hat{V},\\
&\hat{H}_0 = \hbar\sum_j \omega_j |j\rangle\langle j| + \hbar\omega_r \hat{a}^\dagger \hat{a} + \hbar\omega_f \hat{b}^\dagger \hat{b},\\
&\hat{V} = \hbar\sum_i g^r_{j,j+1}(|j\rangle\langle j+1|\hat{a}^\dagger + |j+1\rangle\langle j|\hat{a}) + \hbar\sum_i g^f_{j,j+1}(|j\rangle\langle j+1|\hat{b}^\dagger + |j+1\rangle\langle j|\hat{b}).
\end{aligned} \tag{4.1}$$

Assuming that both ω_r and ω_f are largely detuned from $\omega_{i,i+1} = \omega_{i+1} - \omega_i$ compared to the coupling strength $g^r_{j,j+1}$ and $g^f_{j,j+1}$, we are able to perform Schrieffer-Wolff transformation $H_{\text{eff}} = e^{-S} H e^{S}$ with

$$\hat{S} = \sum_i \lambda^r_i (|i+1\rangle\langle i|\hat{a} - |i\rangle\langle i+1|\hat{a}^\dagger) + \sum_i \lambda^f_i (|i+1\rangle\langle i|\hat{b} - |i\rangle\langle i+1|\hat{b}^\dagger). \tag{4.2}$$

Since we have

$$\begin{aligned}
[\hat{S}, \hat{H}_0] = \hbar\sum_i &\lambda^r_i(-\omega_{i+1} + \omega_i + \omega_r)(|i+1\rangle\langle i|\hat{a} + |i\rangle\langle i+1|\hat{a}^\dagger),\\
+\hbar\sum_i &\lambda^f_i(-\omega_{i+1} + \omega_i + \omega_f)(|i+1\rangle\langle i|\hat{b} + |i\rangle\langle i+1|\hat{b}^\dagger),
\end{aligned} \tag{4.3}$$

where $\lambda_r = g_r/(\omega_c - \omega_r)$ and $\lambda_f = g_f/(\omega_c - \omega_f)$, we can see that $[S, H_0] + V = 0$. From the relation $H_{\text{eff}} = H_0 + V + [S, H_0] + [S, V] + \frac{1}{2}[S, [S, H_0]] + \frac{1}{2}[S, [S, V]] + ...$, we get the final

Hamiltonian $H_{\text{eff}} = H_0 + \frac{1}{2}[S, V] + O(\lambda^2)$. From Equation 1.23 and the relations

$$\begin{aligned}
&[|i+1\rangle\langle i|\hat{a}, |j+1\rangle\langle j|\hat{b}] = \delta_{i,j+1}|i+1\rangle\langle i-1|\hat{a}\hat{b} - \delta_{i+1,j}|i+2\rangle\langle i|\hat{a}\hat{b}, \text{ and} \\
&[|i+1\rangle\langle i|\hat{a}, |j\rangle\langle j+1|\hat{b}^\dagger] = \delta_{i,j}|i+1\rangle\langle i+1|\hat{a}\hat{b}^\dagger - \delta_{i,j}|i\rangle\langle i|\hat{a}\hat{b}^\dagger,
\end{aligned} \tag{4.4}$$

we thus have

$$\begin{aligned}
[\hat{S}, \hat{V}] = \hbar\sum_i(\lambda^r_{i+1}g_{i,i+1} - \lambda^r_i g_{i+1,i+2})(|i+2\rangle\langle i|\hat{a}\hat{a} + |i\rangle\langle i+2|\hat{a}^\dagger\hat{a}^\dagger) \\
+2\hbar\sum_i \chi^r_{i,i+1}|i+1\rangle\langle i+1| + 2\hbar\sum_{i=1}^{\infty}(\chi^r_{i-1,i} - \chi^r_{i,i+1})|i\rangle\langle i|\hat{a}^\dagger\hat{a} - 2\hbar\chi^r_{0,1}|0\rangle\langle 0|\hat{a}^\dagger\hat{a} \\
+\hbar\sum_i(\lambda^f_{i+1}g_{i,i+1} - \lambda^f_i g_{i+1,i+2})(|i+2\rangle\langle i|\hat{b}\hat{b} + |i\rangle\langle i+2|\hat{b}^\dagger\hat{b}^\dagger) \\
+2\hbar\sum_i \chi^f_{i,i+1}|i+1\rangle\langle i+1| + 2\hbar\sum_{i=1}^{\infty}(\chi^f_{i-1,i} - \chi^f_{i,i+1})|i\rangle\langle i|\hat{b}^\dagger\hat{b} - 2\hbar\chi^f_{0,1}|0\rangle\langle 0|\hat{b}^\dagger\hat{b} \\
+\hbar\sum_i(\lambda^r_{i+1}g^f_{i,i+1} - \lambda^r_i g^f_{i+1,i+2})(|i+2\rangle\langle i|\hat{a}\hat{b} + |i\rangle\langle i+2|\hat{a}^\dagger\hat{b}^\dagger) \\
+\hbar\sum_{i=1}^{\infty}(\lambda^r_{i-1}g^f_{i-1,i} - \lambda^r_i g^f_{i,i+1})|i\rangle\langle i|(\hat{a}\hat{b}^\dagger + \hat{a}^\dagger\hat{b}) - \hbar\lambda^r_0 g^f_{0,1}|0\rangle\langle 0|(\hat{a}\hat{b}^\dagger + \hat{a}^\dagger\hat{b}) \\
+\hbar\sum_i(\lambda^f_{i+1}g^r_{i,i+1} - \lambda^f_i g^r_{i+1,i+2})(|i+2\rangle\langle i|\hat{a}\hat{b} + |i\rangle\langle i+2|\hat{a}^\dagger\hat{b}^\dagger) \\
+\hbar\sum_{i=1}^{\infty}(\lambda^f_{i-1}g^r_{i-1,i} - \lambda^f_i g^r_{i,i+1})|i\rangle\langle i|(\hat{a}\hat{b}^\dagger + \hat{a}^\dagger\hat{b}) - \hbar\lambda^f_0 g^r_{0,1}|0\rangle\langle 0|(\hat{a}\hat{b}^\dagger + \hat{a}^\dagger\hat{b}).
\end{aligned} \tag{4.5}$$

With the two-photon transition terms small and negligible as stated previously [3], we can write the final effective Hamiltonian as

$$\begin{aligned}
H_{\text{eff}} = \hbar\sum_j \omega_j|j\rangle\langle j| + \hbar\omega_r\hat{a}^\dagger\hat{a} + \hbar\omega_f\hat{b}^\dagger\hat{b} + \hbar\sum_i \chi^r_{i,i+1}|i+1\rangle\langle i+1| + \hbar\sum_i \chi^f_{i,i+1}|i+1\rangle\langle i+1| \\
+ \hbar\sum_{i=1}^{\infty}(\chi^r_{i-1,i} - \chi^r_{i,i+1})|i\rangle\langle i|\hat{a}^\dagger\hat{a} - \hbar\chi^r_{0,1}|0\rangle\langle 0|\hat{a}^\dagger\hat{a} + \hbar\sum_{i=1}^{\infty}(\chi^f_{i-1,i} - \chi^f_{i,i+1})|i\rangle\langle i|\hat{b}^\dagger\hat{b} - \hbar\chi^f_{0,1}|0\rangle\langle 0|\hat{b}^\dagger\hat{b} \\
+ \hbar\sum_{i=1}^{\infty}(G_{i-1,i} - G_{i,i+1})|i\rangle\langle i|(\hat{a}\hat{b}^\dagger + \hat{a}^\dagger\hat{b}) - \hbar G_{0,1}|0\rangle\langle 0|(\hat{a}\hat{b}^\dagger + \hat{a}^\dagger\hat{b}).
\end{aligned} \tag{4.6}$$

Here $\chi_{i,i+1}^{r(f)}$ is defined as $\lambda_i^{r(f)} g_{i,i+1}^{r(f)}$ which is ${g_{i,i+1}^{r(f)}}^2/(\omega_{i,i+1}-\omega_{r(f)})$, and

$$G_{i,i+1} = \frac{\lambda_i^r g_{i,i+1}^f + \lambda_i^f g_{i,i+1}^r}{2} = \frac{g_{i,i+1}^r g_{i,i+1}^f}{2}\left(\frac{1}{\omega_{i,i+1}-\omega_r} + \frac{1}{\omega_{i,i+1}-\omega_f}\right).$$

4.4 The tunable coupler design

Direct realization of the circuit with equal ω_r and ω_f faces difficulties from two reasons. First, possible difficulties may appear in fabricating two fixed linear cavities with equal resonance frequencies within certain desired accuracy. Second, with approximated frequencies for the two cavities, the virtual exchange interaction mediated by the common qutrit that they are dispersively coupled to dominants the coupling between them, making the scale of the coupling strength uncontrollable. For those two reasons, we come to the design with a parametrically tunable coupler, which is realized as the design in previous works [52, 43, 70]. Here, ω_r and ω_f are off-resonant with a relatively large detuning in between compared to the coupling strength mediated by the qutrit and other parts of the circuit. The resonance cavity and the filter cavity are coupled with a tunable coupler with coupling strength parametrically tuned by a frequency ω_t, causing an additional coupling strength $G(t) = 2G_d\cos(\omega_t t) + G_s$. With rotating wave approximation, $G(t)(\hat{a}+\hat{a}^\dagger)(\hat{b}+\hat{b}^\dagger)$ is only preserved as $G(t)(\hat{a}\hat{b}^\dagger + \hat{a}^\dagger\hat{b})$, then the system Hamiltonian becomes,

$$\begin{aligned} H(t) = {} & \hbar\sum_j \tilde{\omega}_j |j\rangle\langle j| + \hbar\tilde{\omega}_r \hat{a}^\dagger\hat{a} + \hbar\tilde{\omega}_f \hat{b}^\dagger\hat{b} + \hbar\sum_{i=1}^{\infty}\chi_i^r |i\rangle\langle i|\hat{a}^\dagger\hat{a} + \hbar\sum_{i=1}^{\infty}\chi_i^f |i\rangle\langle i|\hat{b}^\dagger\hat{b} \\ & + \hbar\sum_i G_i |i\rangle\langle i|(\hat{a}\hat{b}^\dagger + \hat{a}^\dagger\hat{b}) + \hbar(G_d e^{i\omega_t t} + G_d e^{-i\omega_t t} + G_s)(\hat{a}\hat{b}^\dagger + \hat{a}^\dagger\hat{b}). \end{aligned} \tag{4.7}$$

Here the coefficients are defined as, $\tilde{\omega}_0 = \omega_0$, $\tilde{\omega}_i = \omega_i + \chi_{i,i+1}^r + \chi_{i,i+1}^f (i \geq 1)$, $\tilde{\omega}_{r(f)} = \omega_{r(f)} - \chi_{0,1}^{r(f)}$, $\chi_i^{r(f)} = \chi_{i-1,i}^{r(f)} - \chi_{i,i+1}^{r(f)} + \chi_{0,1}^{r(f)}$, $G_0 = -G_{0,1}$, and $G_i = G_{i-1,i} - G_{i,i+1}$. Going to a rotating frame by performing the unitary transformation,

$$\hat{U}(t) = \exp\left\{ -i(\sum_j \tilde{\omega}_j |j\rangle\langle j| + \tilde{\omega}_r \hat{a}^\dagger \hat{a} + \tilde{\omega}_f \hat{b}^\dagger \hat{b})t \right\},$$

the Hamiltonian becomes,

$$\begin{aligned} \hat{H}' = \hat{U}^\dagger \hat{H} \hat{U} - i\hbar \hat{U}^\dagger \partial_t \hat{U} &= \hbar \sum_{i=1}^{\infty} \chi_i^r |i\rangle\langle i| \hat{a}^\dagger \hat{a} + \hbar \sum_{i=1}^{\infty} \chi_i^f |i\rangle\langle i| \hat{b}^\dagger \hat{b} \\ &+ \hbar \sum_i (G_i + G_s) |i\rangle\langle i| (e^{i(-\omega_r+\omega_f)t} \hat{a}\hat{b}^\dagger + e^{i(\omega_r-\omega_f)t} \hat{a}^\dagger \hat{b}) \\ &+ \hbar (G_d e^{i\omega_t t} + G_d e^{-i\omega_t t})(e^{i(-\omega_r+\omega_f)t} \hat{a}\hat{b}^\dagger + e^{i(\omega_r-\omega_f)t} \hat{a}^\dagger \hat{b}). \end{aligned} \tag{4.8}$$

Choosing the right parameter $\omega_t = \omega_r - \omega_f$, and keeping only the co-rotating terms as was done in previous works [52, 65], we obtain

$$\hat{H}' = \hbar \sum_{i=1}^{\infty} \chi_i^r |i\rangle\langle i| \hat{a}^\dagger \hat{a} + \hbar \sum_{i=1}^{\infty} \chi_i^f |i\rangle\langle i| \hat{b}^\dagger \hat{b} + \hbar G_d (\hat{a}\hat{b}^\dagger + \hat{a}^\dagger \hat{b}), \tag{4.9}$$

which gives the Hamiltonian that we designed for.

4.5 Numerical simulation results

To verify the system behaviour, we use Qutip to simulate the master equation,

$$\frac{d}{dt}\rho(t) = -\frac{i}{\hbar}[H, \rho(t)] + \kappa \mathbf{D}[\hat{b}]\rho(t),$$

where

$$\mathbf{D}[\hat{O}]\rho = \hat{O}\rho\hat{O}^\dagger - \frac{1}{2}\hat{O}^\dagger\hat{O}\rho - \frac{1}{2}\rho\hat{O}^\dagger\hat{O}.$$

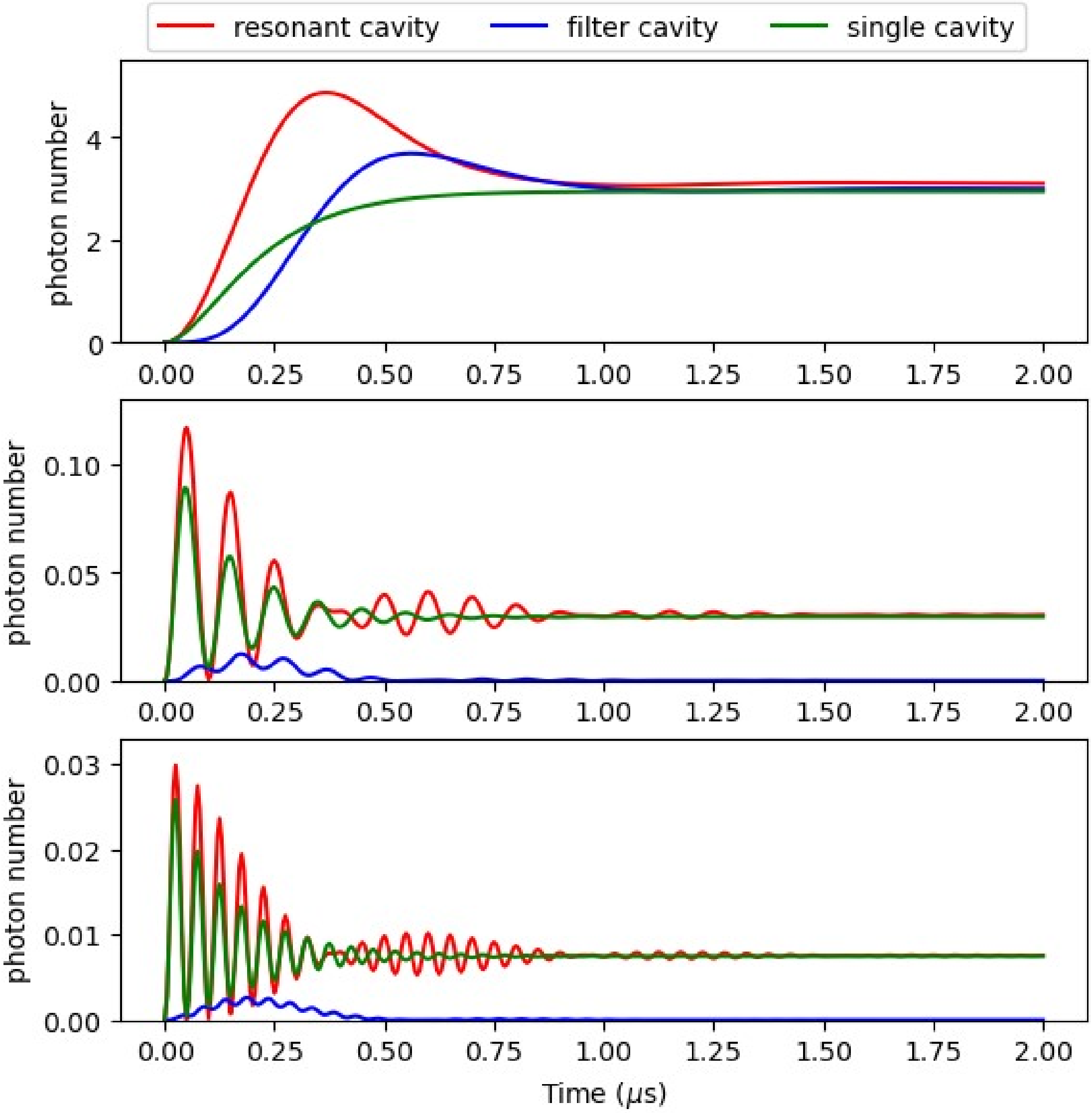

Fig. 4.3: Cavity photon population. Upper/middle/lower: The cavity photon population when the qutrit is prepared in state $|g/e/f\rangle$ and the cavity is probed at the cavity resonance frequency of state $|g\rangle$. Red and blue: the photon number of the resonance cavity and the filter cavity as designed in Fig. 4.1 b and d. Green: the photon number of the single cavity as designed in Fig. 4.1 a and c

For the unitary part of the evolution restricted to the first three energy levels for the qutrit, the Hamiltonian is,

$$\begin{aligned} &H = H_{\text{undriven}} + H_{\text{drive}},\ H_{\text{drive}} = \hbar\epsilon(\hat{a}^\dagger + \hat{a}), \\ &H_{\text{undriven}} = \hbar(\chi_1^r|1\rangle\langle 1| + \chi_2^r|2\rangle\langle 2|)\hat{a}^\dagger\hat{a} + \hbar(\chi_1^f|1\rangle\langle 1| + \chi_2^f|2\rangle\langle 2|)\hat{b}^\dagger\hat{b} + \hbar G_d(\hat{a}\hat{b}^\dagger + \hat{a}^\dagger\hat{b}). \end{aligned} \tag{4.10}$$

The system was driven through the weakly coupled input port in the resonance cavity, and dissipates through the strongly coupled output port in the filter cavity. Qutrit relaxation and dissipation, as well as the photon leakage out of the resonance cavity, are not taken into consideration at this step. Solving this master equation with the master equation solver module in Qutip [12, 13], we track the system behaviours and compared them with the standard readout model. The simulated averaged photon number is in Fig. 4.3. We can see that compared to both the photon population of the resonance cavity and the design in Fig. 4.1 (a)'s cavity, the averaged photon number of the filter cavity is largely suppressed for states $|e\rangle$ and $|f\rangle$, but not for state $|g\rangle$, which is of our desires. This result in similar dephasing rate of the $|g\rangle$ state, but the off-diagonal term between $|e\rangle$ and $|f\rangle$ is preserved, just as shown in Fig. 4.4. Taking the setup with one qutrit as an example here, our target is to measure state $|g\rangle$ with minor disturbance to the coherence between state $|e\rangle$ and $|f\rangle$. This requires enough dephasing to the term $Tr(|g\rangle\langle e|\rho)$ and eliminated dephasing to the term $Tr(|e\rangle\langle f|\rho)$, where ρ is the system density matrix.

We then try the design to be connected to two qutrits in the same way as shown in Fig. 4.1 d, and run the stabilizing protocol on the designed setup. In Fig. 4.5 a and c, we see that the protocol still stabilize the system from state $|gg\rangle$ to the $S_{total} \in \{0, 1\}$ subspace. But if we initialize the system in the $S_{total} \in \{0, 1\}$ subspace, then run the protocol, we get the coherence term between those four states preserved much more than usual, with comparison between Fig. 4.5 c and d.

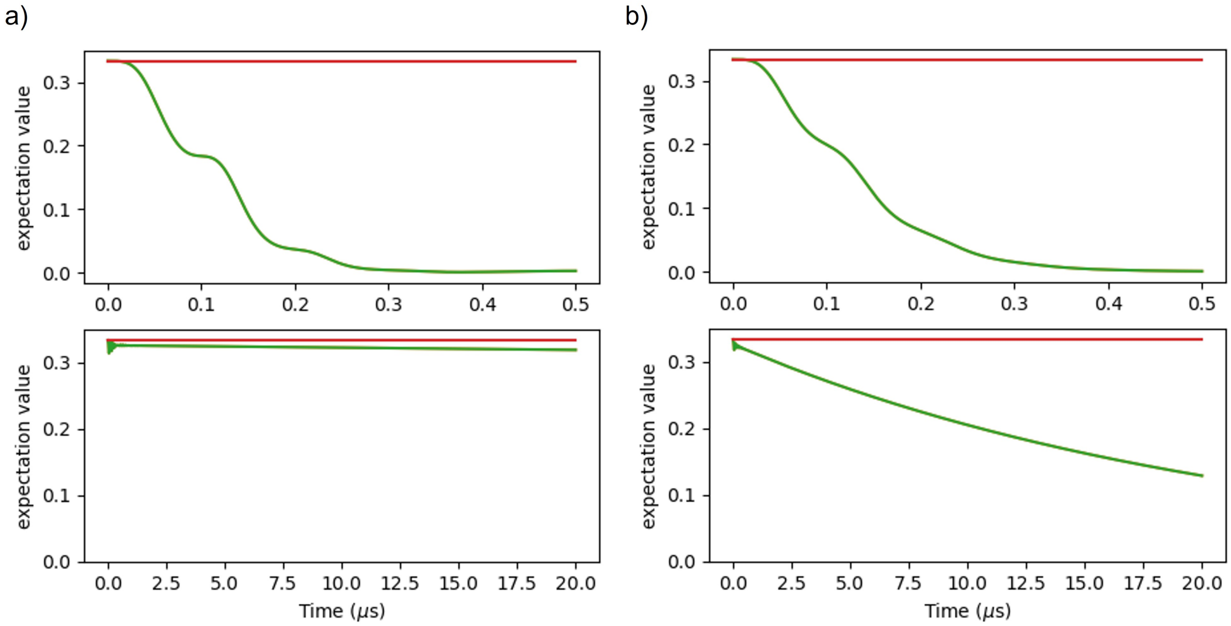

Fig. 4.4: Elimination of extra dephasing in a qutrit readout process. (a) With the design in Fig. 4.1 (d), the system is prepared in $\frac{\sqrt{3}}{3}|g\rangle + \frac{\sqrt{3}}{3}|e\rangle + \frac{\sqrt{3}}{3}|f\rangle$, and probed at the cavity resonance frequency of state $|g\rangle$: Upper: The dephasing between state $|g\rangle$ and state $|e\rangle$ when we have the $\chi = 5\kappa$. Red and blue: the population of state $|g\rangle$ and state $|e\rangle$, green: the absolute value of the cross term between state $|g\rangle$ and state $|e\rangle$. Lower: The dephasing between state $|e\rangle$ and state $|f\rangle$ when we have the $\chi = 5\kappa$. Red and blue: the population of state $|e\rangle$ and state $|f\rangle$, green: the absolute value of the cross term between state $|e\rangle$ and state $|f\rangle$. Compared with (b), we can see that the elimination of the extra measurement induced dephasing is quite huge. (b) With the design in Fig. 4.1 (c), same contents are shown as in (a). Although the cavity photon population for $|e\rangle$ is 100 times less than $|g\rangle$, over the time period of 20 μs the measurement induced dephasing between state $|e\rangle$ and state $|f\rangle$ is still quite concerning.

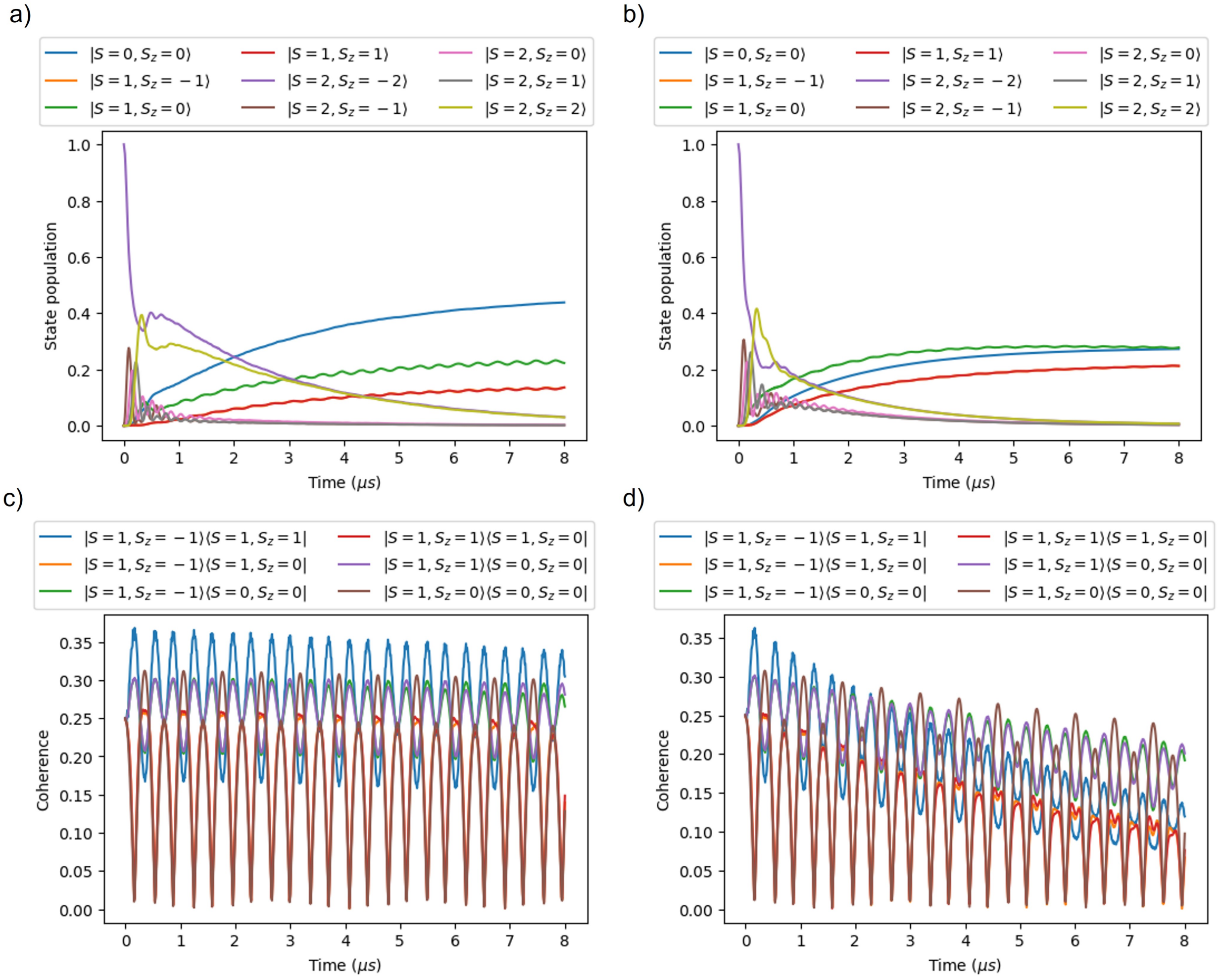

Fig. 4.5: Performance of the protocol. (a) The two-qutrit protocol connected to the cavity design in Fig. 4.1 (b) and d still can stabilize the target subspace. (b) The dephasing among the four protected states is also protected. (c) The two-qutrit protocol connected to the cavity design in Fig. 4.1 (a) and (c) stabilize the target subspace. (d) The dephasing among the four states within the target subspace is quite high accumulated through the stabilizing time for several μs.

4.6 Possible applications and limitations

Applications of this design may go beyond the current AKLT protocol, e.g. if we want such always-on measurements involving several peaks in the cavity spectrum in QEC.

However, in actual experiment involving long-time continuous measurement and sometimes followed by autonomous feedback, when going to several tens of microseconds, the main limitations will be that the non-demolition feature of the measurement is not strict, which causes the qutrit energy to decay. If we do a full Hamiltonian simulation of the dispersive coupled qutrit-cavity system, we can see that energy exchange becomes much more obvious than the residual measurement between the states that are not supposed to be measured. Within the validation of the dispersive limit, simulation shows that this method will have obvious improvements over the normal measurement in eliminating unwanted measurements. But simulation also shows that this improvement is only significant when $\chi \gg \kappa$, where the residual measurement accumulates into effect in about several tens of microseconds. In such time scale, the main factor that hinders the measurement will be its imperfect nondemolition feature caused by higher order nonlinear terms in the dispersive approximation, where the cavity and the qutrits are having actual energy exchanges. Therefore, applying this method may not significantly eliminate the imperfect aspects of the measurement pulse utilized in the protocol introduced in Chap. 5 for actual experiment considerations.

Chapter 5

Discrete time crystalline order with dissipation

In this chapter, we propose experimental implementation of dissipative discrete time crystal on superconducting circuit platform. Potential methods to realize the quantum Rabi model in strong coupling regime are introduced and simulated. Then, such physical realizations are generalized to protocols involving the proposed experimental observation for novel manybody phenomena.

5.1 Time crystalline order

Time crystalline order relates to broken time translational symmetry. The attempts in implementing broken continuous time translational symmetry in thermal equilibrium turned out not possible. However, broken discrete time translational symmetry are observed in quite several platforms. Such discrete time crystalline order shows subharmonic oscillations undergoing periodic driving, and becomes robust against fluctuations in driving parameters. By now, most observation of the discrete time crystalline order are for isolated manybody systems, but dissipative systems can also show such order. Here we review related previous work on this topic and propose an implementation with superconducting transmon qubits.

5.2 Discrete time crystalline order in a dissipative system

Dissipative time crystalline order is proposed [71] and experimentally realized [72] in non-linear optical systems, as well as in the open quantum Dicke model [73]. The latter is proposed [74] and evaluated [75] theoretically and observed with BEC system of ^{87}Rb atoms experimentally [76]. The unitary part of system evolution is

$$\mathrm{H}(t) = \omega_c \hat{a}^\dagger \hat{a} + \omega_0 \hat{J}_z + \frac{2\lambda(t)}{\sqrt{N}}(\hat{a} + \hat{a}^\dagger)\hat{J}_x,$$

where $\hat{a}^\dagger$ and $\hat{a}$ are the creation and annihilation operators of the linear cavity, and ω_c is the cavity resonance frequency. $\hat{J}_z$ and $\hat{J}_x$ are the z and x components of the collective spin consisting of N two-level particles, and $\lambda(t)$ is the time dependent coupling strength. The system is subjected to dissipation of the cavity photons,

$$\frac{d}{dt}\rho(t) = -\frac{i}{\hbar}[H, \rho(t)] + \kappa \mathbf{D}[\hat{a}]\rho(t),$$

with,

$$\mathbf{D}[\hat{O}]\rho = \hat{O}\rho\hat{O}^\dagger - \frac{1}{2}\hat{O}^\dagger\hat{O}\rho - \frac{1}{2}\rho\hat{O}^\dagger\hat{O}.$$

The dissipative time crystalline order is provided by symmetry breaking when the coupling strength is above the critical value $\lambda_c = \frac{1}{2}\sqrt{\frac{\omega_0}{\omega}\left(\omega^2 + \frac{\kappa^2}{4}\right)}$, which gives two steady states with different symmetries [77]. Provided with the parity operator during one period, the subharmonic oscillation between the two steady state can happen in half frequency of the original drive, which reveals a discrete time crystalline order. For example, this behaviour emerges if we assign the time-dependent coupling strength as,

$$\lambda(t) = \begin{cases} \lambda & 0 \leq t < \frac{T}{2} \\ 0 & \frac{T}{2} \leq t < T \end{cases}, \tag{5.1}$$

which is simulated in previous theoretical work [74].

This time crystalline behaviour can be observed in the thermodynamic limit, where N approaches infinity. In deep quantum regime, nevertheless, the system shows a transient time cystalline behaviour, even with an extremely limited qubit number of N=2. Below we design several experimental protocols for observing this few-qubit behaviour.

5.3 Realization of the quantum Rabi model in strong coupling regime

5.3.1 Parametric modulated tunable coupler

The quantum Rabi model describes the system for a transmon qubit and cavity before rotating wave approximation,

$$\hat{\mathrm{H}} = \hbar\omega_r \hat{a}\hat{a}^\dagger + \hbar\frac{\omega_q}{2}\hat{\sigma}_z + \hbar g(\hat{a} + \hat{a}^\dagger)\hat{\sigma}_x.$$

For a static value of the coupling strength g, with $\omega_r + \omega_q \gg |\omega_r - \omega_q|$ and $\omega_r, \omega_q \gg g$, the counter-rotating term will be dropped since it is fast rotating. As we go to the rotating frame for both the cavity and the qubit at ω^0, the Hamiltonian becomes

$$\hat{\mathrm{H}}_{\mathrm{eff}} = \hbar\Delta_r \hat{a}\hat{a}^\dagger + \hbar\frac{\Delta_q}{2}\hat{\sigma}_z + \hbar g(\hat{a}\hat{\sigma}_+ + \hat{a}^\dagger\hat{\sigma}_-).$$

Here $\Delta_r = \omega_r - \omega^0$, $\Delta_q = \omega_q - \omega^0$.

For a parametrically modulated value of the coupling strength as $g(t) = g_+ \cos(\omega_q^0 + \omega_r^0) + g_- \cos(\omega_q^0 - \omega_r^0)$, as we go to the rotating frame for the qubit at frequency ω_q^0 and for the cavity at frequency ω_r^0, the Hamiltonian becomes

$$\begin{aligned}
\hat{\mathrm{H}} &= \hbar\Delta_r \hat{a}\hat{a}^\dagger + \hbar\frac{\Delta_q}{2}\hat{\sigma}_z + \hbar g(t)(e^{-i\omega_r^0 t}\hat{a} + e^{i\omega_r^0 t}\hat{a}^\dagger)(e^{-i\omega_q^0 t}\hat{\sigma}_- + e^{i\omega_q^0 t}\hat{\sigma}_+) \\
&= \hbar\Delta_r \hat{a}\hat{a}^\dagger + \hbar\frac{\Delta_q}{2}\hat{\sigma}_z + \hbar g_+(\hat{a}\hat{\sigma}_- + e^{2i\omega_q^0 t}\hat{a}\hat{\sigma}_+ + e^{2i\omega_r^0 t}\hat{a}^\dagger\hat{\sigma}_- + e^{2i(\omega_r^0+\omega_q^0)t}\hat{a}^\dagger\hat{\sigma}_+) \\
&+ \hbar g_+(e^{-2i(\omega_r^0+\omega_q^0)t}\hat{a}\hat{\sigma}_- + e^{-2i\omega_r^0 t}\hat{a}\hat{\sigma}_+ + e^{-2i\omega_q^0 t}\hat{a}^\dagger\hat{\sigma}_- + \hat{a}^\dagger\hat{\sigma}_+) \\
&+ \hbar g_-(e^{-2i\omega_r^0 t}\hat{a}\hat{\sigma}_- + e^{2i(\omega_q^0-\omega_r^0)t}\hat{a}\hat{\sigma}_+ + \hat{a}^\dagger\hat{\sigma}_- + e^{2i\omega_q^0 t}\hat{a}^\dagger\hat{\sigma}_+) \\
&+ \hbar g_-(e^{-2i\omega_q^0 t}\hat{a}\hat{\sigma}_- + \hat{a}\hat{\sigma}_+ + e^{2i(\omega_r^0-\omega_q^0)t}\hat{a}^\dagger\hat{\sigma}_- + e^{2i\omega_r^0 t}\hat{a}^\dagger\hat{\sigma}_+)
\end{aligned} \tag{5.2}$$

In the regime of our interest, $\Delta_r, \Delta_q \sim g$ and $|\omega_q - \omega_r| \gg g$, we can drop the counter rotating terms and gain the effective Hamiltonian

$$\hat{\mathrm{H}}'_{\text{eff}} = \hbar\Delta_r \hat{a}\hat{a}^\dagger + \hbar\frac{\Delta_q}{2}\hat{\sigma}_z + \hbar g_+(\hat{a}\hat{\sigma}_- + \hat{a}^\dagger\hat{\sigma}_+) + \hbar g_-(\hat{a}^\dagger\hat{\sigma}_- + \hat{a}\hat{\sigma}_+) \tag{5.3}$$

When choosing $g_- = g_+ = g$, we have the quantum Rabi model. This extended range of ratio between the mode frequencies and the coupling strengths give us the strong coupling regime, thus accesses to several possible realizations of certain manybody models.

5.3.2 Parametric modulated tunable qubit

The above realization could be further simplified, where we modulate the frequency of a tunable qubit and couple the qubit directly to the cavity instead. The model to achieve parametric coupling by modulated qubit frequency is analysed [78, 79] and realized [80, 81, 82] in previous works. As is shown previously in Section 1.2, with a tunable transmon qubit, the effective Josephson energy, E_J, is modified via applying different flux bias, Φ. With the qubit frequency being $\omega_q \propto \sqrt{E_J E_C}$, and the coupling strength between the qubit and a linear cavity being $g \propto \sqrt[4]{E_J/E_C}$, we treat the small modulations in E_J as expansions in ω_q

and a fixed value in g for the leading corrections. The system Hamiltonian can be written as,

$$\mathrm{H} = \hbar\omega_r \hat{a}^\dagger \hat{a} + \hbar\omega_q(t)\frac{\hat{\sigma}_z}{2} + \hbar g(\hat{a} + \hat{a}^\dagger)\hat{\sigma}_x. \tag{5.4}$$

In previous works aiming at achieving parametric couplings between the qubit and the cavity, the modulation of the qubit frequency is set to

$$\omega_q(t) = \bar{\omega}_q + \frac{\epsilon_-}{2}\cos\omega_- t, \tag{5.5}$$

where ω_- is chosen to be $\omega_r - \bar{\omega}_q$. In that case, after dropping the counter rotating terms in the Hamiltonian since g is much smaller than the frequency difference ω_-, we have the effective Hamiltonian $H' \propto g(\hat{a}^\dagger\hat{\sigma}_- + \hat{a}\hat{\sigma}_+)$ due to the sideband of the modulated qubit frequency. In this work, instead, we aim at achieving the effective strong coupling between the qubit and the cavity, so we have

$$\omega_q(t) = \bar{\omega}_q + \frac{\epsilon_-}{2}\cos\omega_- t + \frac{\epsilon_+}{2}\cos\omega_+ t. \tag{5.6}$$

This could be done by applying the flux bias around the sweet spot,

$$\Phi(t) = \bar{\Phi} + \tilde{\Phi}_- \cos\omega_- t + \tilde{\Phi}_+ \cos\omega_+ t. \tag{5.7}$$

We go to a rotating frame by performing the unitary transformation,

$$\hat{U}(t) = \exp\left\{-i(\Delta_q t + \frac{\epsilon_-}{2\omega_-}\sin\omega_- t + \frac{\epsilon_+}{2\omega_+}\sin\omega_+ t)\frac{\hat{\sigma}_z}{2} - i\Delta_r \hat{a}^\dagger \hat{a} t\right\}. \tag{5.8}$$

Here we notice that from the commutation relation, $[\hat{\sigma}_-, \hat{\sigma}_z] = 2\hat{\sigma}_-$, $[\hat{\sigma}_+, \hat{\sigma}_z] = -2\hat{\sigma}_+$,we obtain that $\hat{\sigma}_-\hat{\sigma}_z^n = (\hat{\sigma}_z + 2)^n\hat{\sigma}_-$, $\hat{\sigma}_+\hat{\sigma}_z^n = (\hat{\sigma}_z - 2)^n\hat{\sigma}_+$. Similarly, from $[\hat{a}, \hat{a}^\dagger\hat{a}] = \hat{a}$, $[\hat{a}^\dagger, \hat{a}^\dagger\hat{a}] = -\hat{a}^\dagger$, we have $\hat{a}(\hat{a}^\dagger\hat{a})^n = (\hat{a}^\dagger\hat{a} + 1)^n\hat{a}$, $\hat{a}^\dagger(\hat{a}^\dagger\hat{a})^n = (\hat{a}^\dagger\hat{a} - 1)^n\hat{a}^\dagger$. We also have the definition of the Bessel function, obtaining that $e^{iy\sin x} = \sum_{n\in\mathbb{Z}} \mathrm{J}_n(y)e^{inx}$. Then the effective Hamiltonian becomes,

$$\begin{aligned}
\hat{H}_{\text{eff}} &= \hat{U}^\dagger \hat{H} \hat{U} - i\hbar \hat{U}^\dagger \partial_t \hat{U} = \hat{U}^\dagger \hat{U}(\hbar\omega_r \hat{a}^\dagger \hat{a} + \hbar\omega_q(t)\frac{\hat{\sigma}_z}{2}) + \hat{U}^\dagger g(\hat{a} + \hat{a}^\dagger)\hat{\sigma}_x \hat{U} \\
&- i\hbar \hat{U}^\dagger \hat{U}(-i)[(\Delta_q + \frac{\epsilon_-}{2}\cos\omega_- t + \frac{\epsilon_+}{2}\cos\omega_+ t)\frac{\hat{\sigma}_z}{2} + \Delta_r \hat{a}^\dagger \hat{a}] \\
&= \hat{U}^\dagger g(\hat{a} + \hat{a}^\dagger)(\hat{\sigma}_- + \hat{\sigma}_+)\hat{U} + \hbar(\omega_r - \Delta_r)\hat{a}^\dagger \hat{a} + \hbar(\bar{\omega}_q - \Delta_q)\frac{\hat{\sigma}_z}{2} \\
&= g(e^{-i\Delta_r t}\hat{a} + h.c.)(e^{-i(\Delta_q t + \frac{\epsilon_-}{2\omega_-}\sin\omega_- t + \frac{\epsilon_+}{2\omega_+}\sin\omega_+ t)}\hat{\sigma}_- + h.c.) + \hbar\omega_r' \hat{a}^\dagger \hat{a} + \hbar\omega_q' \frac{\hat{\sigma}_z}{2} \\
&= g(e^{-i\Delta_r t}\hat{a} + h.c.)(e^{-i\Delta_q t}\left[\sum_{n\in\mathbb{Z}} \mathrm{J}_n\left(\frac{\epsilon_-}{2\omega_-}\right)e^{-in\omega_- t}\right]\left[\sum_{m\in\mathbb{Z}} \mathrm{J}_m\left(\frac{\epsilon_+}{2\omega_+}\right)e^{-im\omega_+ t}\right]\hat{\sigma}_- \qquad (5.9) \\
&+ h.c.) + \hbar\omega_r' \hat{a}^\dagger \hat{a} + \hbar\omega_q' \frac{\hat{\sigma}_z}{2} \\
&= g\sum_{\substack{n\in\mathbb{Z}\\ m\in\mathbb{Z}}} \mathrm{J}_n\left(\frac{\epsilon_-}{2\omega_-}\right)\mathrm{J}_m\left(\frac{\epsilon_+}{2\omega_+}\right)e^{-i(\Delta_r+\Delta_q)t - in\omega_- t - im\omega_+ t}\hat{a}\hat{\sigma}_- + h.c. \\
&+ g\sum_{\substack{n\in\mathbb{Z}\\ m\in\mathbb{Z}}} \mathrm{J}_n\left(\frac{\epsilon_-}{2\omega_-}\right)\mathrm{J}_m\left(\frac{\epsilon_+}{2\omega_+}\right)e^{-i(\Delta_r-\Delta_q)t + in\omega_- t + im\omega_+ t}\hat{a}\hat{\sigma}_+ + h.c. + \hbar\omega_r' \hat{a}^\dagger \hat{a} + \hbar\omega_q' \frac{\hat{\sigma}_z}{2}.
\end{aligned}$$

Here we take the values $\bar{\omega}_q - \Delta_q = \omega_q'$, $\omega_r - \Delta_r = \omega_r'$. We also choose the modulation frequencies as $\omega_- = \Delta_r - \Delta_q$ and $\omega_+ = \Delta_r + \Delta_q$. For the Bessel function with $0 < x < 1$, the absolute value of $\mathrm{J}_n(x)$ will drop quickly for $n \geq 2$, leaving the lower order values to be dominating. Excluding the case when $n\omega_- + (m \pm 1)\omega_+ \to 0$ or $(n \pm 1)\omega_- + m\omega_+ \to 0$, we are able to drop the counter rotating terms and arrive at the final effective Hamiltonian

$$\begin{aligned}
\hat{H}_{\text{eff}} &= g\mathrm{J}_0\left(\frac{\epsilon_-}{2\omega_-}\right)\mathrm{J}_{-1}\left(\frac{\epsilon_+}{2\omega_+}\right)\hat{a}\hat{\sigma}_- + g\mathrm{J}_1\left(\frac{\epsilon_-}{2\omega_-}\right)\mathrm{J}_0\left(\frac{\epsilon_+}{2\omega_+}\right)\hat{a}\hat{\sigma}_+ \\
&+ g\mathrm{J}_0\left(\frac{\epsilon_-}{2\omega_-}\right)\mathrm{J}_{-1}\left(\frac{\epsilon_+}{2\omega_+}\right)\hat{a}^\dagger\hat{\sigma}_+ + g\mathrm{J}_1\left(\frac{\epsilon_-}{2\omega_-}\right)\mathrm{J}_0\left(\frac{\epsilon_+}{2\omega_+}\right)\hat{a}^\dagger\hat{\sigma}_- + \hbar\omega_r' \hat{a}^\dagger \hat{a} + \hbar\omega_q' \frac{\hat{\sigma}_z}{2} \qquad (5.10) \\
&= g\mathrm{J}_0(\alpha)\mathrm{J}_1(\alpha)\hat{\sigma}_x(\hat{a} + \hat{a}^\dagger) + \hbar\omega_r' \hat{a}^\dagger \hat{a} + \hbar\omega_q' \frac{\hat{\sigma}_z}{2},
\end{aligned}$$

with $\alpha = \epsilon_-/2\omega_- = -\epsilon_+/2\omega_+$. The largest value of $\mathrm{J}_0(\alpha)\mathrm{J}_1(\alpha)$ is around $\alpha = 1.08$ with the value 0.339. With such freedom of parameter choice, we can simulate any ratio between the coupling strength and the atom energy frequencies by shifting the modulation frequency.

Chapter 6

Conclusion

In this dissertation, we have presented a comprehensive exploration of quantum information processing via dissipation engineering in the superconducting circuit platform. Our investigation has shed light on the potential of dissipation as a novel and powerful tool for manipulating and processing quantum information.

Throughout this work, we have examined various aspects of dissipation engineering, starting with an introduction to the Josephson junction as a fundamental component in superconducting circuits. This foundational knowledge laid the groundwork for our subsequent discussions on the superconducting Transmon circuit and its interaction with the microwave cavity.

In Chapter 2, we delved into the intricate concept of the geometric phase and its accumulation under adiabatic evolution. We investigated measurement-induced geometric phase transitions and devised different protocols for measuring the decoherence-induced geometric phase. Our comprehensive simulation and experimental results have demonstrated the potential for achieving precise control and manipulation of quantum states to realize dissipation-based geometric phase measurements.

Additionally, in Chapter 3, we explored state stabilization by dissipation. The study of many-body states, specifically the AKLT state, provided valuable insights into the use of dissipation as a means of stabilizing and engineering complex quantum states. By examining the performance of various stabilization protocols, we have demonstrated that dissipation can effectively prepare and stabilize a topologically nontrivial many-body state.

In conclusion, the findings presented in this dissertation demonstrate the integration of dissipation engineering into the superconducting circuit platform, which offers new possibilities for the realization of robust and fault-tolerant quantum information processing schemes. By leveraging dissipation, we can achieve better control, measurement, and stabilization of quantum states, thereby overcoming challenges posed by decoherence. The findings presented herein provide a solid foundation for future research in this rapidly evolving field.

Bibliography

[1] B.D. Josephson. Possible new effects in superconductive tunnelling. *Physics Letters*, 1:251–253, 7 1962.

[2] A. Smerzi, S. Fantoni, S. Giovanazzi, and S. R. Shenoy. Quantum coherent atomic tunneling between two trapped bose-einstein condensates. *Physical Review Letters*, 79:4950–4953, 12 1997.

[3] Jens Koch, Terri M. Yu, Jay Gambetta, A. A. Houck, D. I. Schuster, J. Majer, Alexandre Blais, M. H. Devoret, S. M. Girvin, and R. J. Schoelkopf. Charge-insensitive qubit design derived from the cooper pair box. *Physical Review A*, 76:042319, 10 2007.

[4] M. H. Devoret, A. Wallraff, and J. M. Martinis. Superconducting qubits: A short review. 11 2004.

[5] M. D. Hutchings, J. B. Hertzberg, Y. Liu, N. T. Bronn, G. A. Keefe, Markus Brink, Jerry M. Chow, and B. L. T. Plourde. Tunable superconducting qubits with flux-independent coherence. *Physical Review Applied*, 8:044003, 10 2017.

[6] Alexandre Blais, Ren-Shou Huang, Andreas Wallraff, S. M. Girvin, and R. J. Schoelkopf. Cavity quantum electrodynamics for superconducting electrical circuits: An architecture for quantum computation. *Physical Review A*, 69:062320, 6 2004.

[7] A. Wallraff, D. I. Schuster, A. Blais, L. Frunzio, R.-S. Huang, J. Majer, S. Kumar, S. M. Girvin, and R. J. Schoelkopf. Strong coupling of a single photon to a superconducting qubit using circuit quantum electrodynamics. *Nature*, 431:162–167, 9 2004.

[8] G. Ithier, E. Collin, P. Joyez, P. J. Meeson, D. Vion, D. Esteve, F. Chiarello, A. Shnirman, Y. Makhlin, J. Schriefl, and G. Scheon. Decoherence in a superconducting quantum bit circuit. *Physical Review B*, 72:134519, 10 2005.

[9] G Lindblad. Mathematical physics on the generators of quantum dynamical semigroups, 1976.

[10] Alexander Shnirman, Yuriy Makhlin, Yuriy Makhlin, Gerd Sch?n, and Gerd Sch?n. Noise and decoherence in quantum two-level systems. *Physica Scripta*, T102:147, 2002.

[11] Yuriy Makhlin and Alexander Shnirman. Dephasing of solid-state qubits at optimal points. *Physical Review Letters*, 92:178301, 4 2004.

[12] J.R. Johansson, P.D. Nation, and Franco Nori. Qutip: An open-source python framework for the dynamics of open quantum systems. *Computer Physics Communications*, 183:1760–1772, 8 2012.

[13] J.R. Johansson, P.D. Nation, and Franco Nori. Qutip 2: A python framework for the dynamics of open quantum systems. *Computer Physics Communications*, 184:1234–1240, 4 2013.

[14] Huo Chen and Daniel A. Lidar. Hamiltonian open quantum system toolkit. *Communications Physics*, 5:112, 5 2022.

[15] Jay Gambetta, Alexandre Blais, D. I. Schuster, A. Wallraff, L. Frunzio, J. Majer, M. H. Devoret, S. M. Girvin, and R. J. Schoelkopf. Qubit-photon interactions in a cavity: Measurement-induced dephasing and number splitting. *Physical Review A*, 74:042318, 10 2006.

[16] M. V. Berry. Quantal phase factors accompanying adiabatic changes. *Proceedings of the Royal Society of London. A. Mathematical and Physical Sciences*, 392:45–57, 3 1984.

[17] S. Pancharatnam. Generalized theory of interference, and its applications. *Proceedings of the Indian Academy of Sciences - Section A*, 44:247–262, 11 1956.

[18] Joseph Samuel and Rajendra Bhandari. General setting for berry's phase. *Physical Review Letters*, 60:2339–2342, 6 1988.

[19] Valentin Gebhart, Kyrylo Snizhko, Thomas Wellens, Andreas Buchleitner, Alessandro Romito, and Yuval Gefen. Topological transition in measurement-induced geometric phases. *Proceedings of the National Academy of Sciences*, 117:5706–5713, 3 2020.

[20] M. Hatridge, S. Shankar, M. Mirrahimi, F. Schackert, K. Geerlings, T. Brecht, K. M. Sliwa, B. Abdo, L. Frunzio, S. M. Girvin, R. J. Schoelkopf, and M. H. Devoret. Quantum back-action of an individual variable-strength measurement. *Science*, 339:178–181, 1 2013.

[21] Yunzhao Wang, Kyrylo Snizhko, Alessandro Romito, Yuval Gefen, and Kater Murch. Observing a topological transition in weak-measurement-induced geometric phases. *Physical Review Research*, 4:023179, 6 2022.

[22] Kyrylo Snizhko, Parveen Kumar, Nihal Rao, and Yuval Gefen. Weak-measurement-induced asymmetric dephasing: Manifestation of intrinsic measurement chirality. *Physical Review Letters*, 127:170401, 10 2021.

[23] Kyrylo Snizhko, Nihal Rao, Parveen Kumar, and Yuval Gefen. Weak-measurement-induced phases and dephasing: Broken symmetry of the geometric phase. *Physical Review Research*, 3:043045, 10 2021.

[24] Hanhee Paik, D. I. Schuster, Lev S. Bishop, G. Kirchmair, G. Catelani, A. P. Sears, B. R. Johnson, M. J. Reagor, L. Frunzio, L. I. Glazman, S. M. Girvin, M. H. Devoret, and R. J. Schoelkopf. Observation of high coherence in josephson junction qubits measured in a three-dimensional circuit qed architecture. *Physical Review Letters*, 107:240501, 12 2011.

[25] M. D. Reed, L. DiCarlo, B. R. Johnson, L. Sun, D. I. Schuster, L. Frunzio, and R. J. Schoelkopf. High-fidelity readout in circuit quantum electrodynamics using the jaynes-cummings nonlinearity. *Physical Review Letters*, 105:173601, 10 2010.

[26] Frank Verstraete, Michael M. Wolf, and J. Ignacio Cirac. Quantum computation and quantum-state engineering driven by dissipation. *Nature Physics*, 5:633–636, 9 2009.

[27] Patrick M. Harrington, Erich J. Mueller, and Kater W. Murch. Engineered dissipation for quantum information science. *Nature Reviews Physics*, 4(10):660–671, August 2022.

[28] Anton Mazurenko, Christie S. Chiu, Geoffrey Ji, Maxwell F. Parsons, MÃ¡rton KanÃ¡sz-Nagy, Richard Schmidt, Fabian Grusdt, Eugene Demler, Daniel Greif, and Markus Greiner. A cold-atom fermiâhubbard antiferromagnet. *Nature*, 545:462–466, 5 2017.

[29] Edward Farhi, Jeffrey Goldstone, Sam Gutmann, Joshua Lapan, Andrew Lundgren, and Daniel Preda. A quantum adiabatic evolution algorithm applied to random instances of an np-complete problem. *Science*, 292:472–475, 4 2001.

[30] Tadashi Kadowaki and Hidetoshi Nishimori. Quantum annealing in the transverse ising model. *Physical Review E*, 58:5355–5363, 11 1998.

[31] B. Kraus, H. P. BÃ¼chler, S. Diehl, A. Kantian, A. Micheli, and P. Zoller. Preparation of entangled states by quantum markov processes. *Physical Review A*, 78:042307, 10 2008.

[32] Ian Affleck, Tom Kennedy, Elliott H. Lieb, and Hal Tasaki. Rigorous results on valence-bond ground states in antiferromagnets. *Physical Review Letters*, 59:799–802, 8 1987.

[33] D. Gross and J. Eisert. Novel schemes for measurement-based quantum computation. *Physical Review Letters*, 98:220503, 5 2007.

[34] Gavin K. Brennen and Akimasa Miyake. Measurement-based quantum computer in the

gapped ground state of a two-body hamiltonian. *Physical Review Letters*, 101:010502, 7 2008.

[35] D. Perez-Garcia, F. Verstraete, M.M. Wolf, and J.I. Cirac. Matrix product state representations. *Quantum Information and Computation*, 7:401–430, 7 2007.

[36] Rainer Kaltenbaek, Jonathan Lavoie, Bei Zeng, Stephen D. Bartlett, and Kevin J. Resch. Optical one-way quantum computing with a simulated valence-bond solid. *Nature Physics*, 6:850–854, 11 2010.

[37] Tianqi Chen, Ruizhe Shen, Ching Hua Lee, and Bo Yang. High-fidelity realization of the aklt state on a nisq-era quantum processor. 10 2022.

[38] C. SchÃ¶n, E. Solano, F. Verstraete, J. I. Cirac, and M. M. Wolf. Sequential generation of entangled multiqubit states. *Physical Review Letters*, 95:110503, 9 2005.

[39] Kevin C. Smith, Eleanor Crane, Nathan Wiebe, and S. M. Girvin. Deterministic constant-depth preparation of the aklt state on a quantum processor using fusion measurements. 10 2022.

[40] Vaibhav Sharma and Erich J. Mueller. Driven-dissipative control of cold atoms in tilted optical lattices. *Physical Review A*, 103:043322, 4 2021.

[41] Leo Zhou, Soonwon Choi, and Mikhail D. Lukin. Symmetry-protected dissipative preparation of matrix product states. *Physical Review A*, 104:032418, 9 2021.

[42] K. W. Murch, U. Vool, D. Zhou, S. J. Weber, S. M. Girvin, and I. Siddiqi. Cavity-assisted quantum bath engineering. *Physical Review Letters*, 109(18), October 2012.

[43] Yao Lu, S. Chakram, N. Leung, N. Earnest, R.âK. Naik, Ziwen Huang, Peter Groszkowski, Eliot Kapit, Jens Koch, and David I. Schuster. Universal stabilization of a parametrically coupled qubit. *Physical Review Letters*, 119:150502, 10 2017.

[44] A. Grimm, N. E. Frattini, S. Puri, S. O. Mundhada, S. Touzard, M. Mirrahimi, S. M. Girvin, S. Shankar, and M. H. Devoret. Stabilization and operation of a kerr-cat qubit. *Nature*, 584:205–209, 8 2020.

[45] Z. Leghtas, S. Touzard, I. M. Pop, A. Kou, B. Vlastakis, A. Petrenko, K. M. Sliwa, A. Narla, S. Shankar, M. J. Hatridge, M. Reagor, L. Frunzio, R. J. Schoelkopf, M. Mirrahimi, and M. H. Devoret. Confining the state of light to a quantum manifold by engineered two-photon loss. *Science*, 347:853–857, 2 2015.

[46] Sergio O. Valenzuela, William D. Oliver, David M. Berns, Karl K. Berggren, Leonid S. Levitov, and Terry P. Orlando. Microwave-induced cooling of a superconducting qubit. *Science*, 314:1589–1592, 12 2006.

[47] P. Magnard, P. Kurpiers, B. Royer, T. Walter, J.-C. Besse, S. Gasparinetti, M. Pechal, J. Heinsoo, S. Storz, A. Blais, and A. Wallraff. Fast and unconditional all-microwave reset of a superconducting qubit. *Physical Review Letters*, 121:060502, 8 2018.

[48] E.âT. Holland, B. Vlastakis, R.âW. Heeres, M.âJ. Reagor, U. Vool, Z. Leghtas, L. Frunzio, G. Kirchmair, M.âH. Devoret, M. Mirrahimi, and R.âJ. Schoelkopf. Single-photon-resolved cross-kerr interaction for autonomous stabilization of photon-number states. *Physical Review Letters*, 115:180501, 10 2015.

[49] K. Geerlings, Z. Leghtas, I. M. Pop, S. Shankar, L. Frunzio, R. J. Schoelkopf, M. Mirrahimi, and M. H. Devoret. Demonstrating a driven reset protocol for a superconducting qubit. *Physical Review Letters*, 110:120501, 3 2013.

[50] S. Shankar, M. Hatridge, Z. Leghtas, K. M. Sliwa, A. Narla, U. Vool, S. M. Girvin, L. Frunzio, M. Mirrahimi, and M. H. Devoret. Autonomously stabilized entanglement between two superconducting quantum bits. *Nature*, 504:419–422, 12 2013.

[51] M.âE. Kimchi-Schwartz, L. Martin, E. Flurin, C. Aron, M. Kulkarni, H.âE. Tureci,

and I. Siddiqi. Stabilizing entanglement via symmetry-selective bath engineering in superconducting qubits. *Physical Review Letters*, 116:240503, 6 2016.

[52] T. Brown, E. Doucet, D. Riste, G. Ribeill, K. Cicak, J. Aumentado, R. Simmonds, L. Govia, A. Kamal, and L. Ranzani. Trade off-free entanglement stabilization in a superconducting qutrit-qubit system. *Nature Communications*, 13:3994, 7 2022.

[53] Ruichao Ma, Brendan Saxberg, Clai Owens, Nelson Leung, Yao Lu, Jonathan Simon, and David I. Schuster. A dissipatively stabilized mott insulator of photons. *Nature*, 566:51–57, 2 2019.

[54] M. S. Blok, V. V. Ramasesh, T. Schuster, K. O'Brien, J. M. Kreikebaum, D. Dahlen, A. Morvan, B. Yoshida, N. Y. Yao, and I. Siddiqi. Quantum information scrambling on a superconducting qutrit processor. *Phys. Rev. X*, 11:021010, Apr 2021.

[55] Sthitadhi Roy, J. T. Chalker, I. V. Gornyi, and Yuval Gefen. Measurement-induced steering of quantum systems. *Physical Review Research*, 2, 9 2020.

[56] F D M Haldane. Continuum dynamics of the 1-d heisenberg antiferromagnet: Identification with the 0(3) nonlinear sigma model, 1983.

[57] I Affleck. Quantum spin chains and the haldane gap. *Journal of Physics: Condensed Matter*, 1:3047–3072, 5 1989.

[58] Tzu-Chieh Wei, Robert Raussendorf, and Ian Affleck. Some aspects of affleck-kennedy-lieb-tasaki models: tensor network, physical properties, spectral gap, deformation, and quantum computation. 1 2022.

[59] Xiao-Gang Wen. <i>colloquium</i> : Zoo of quantum-topological phases of matter. *Reviews of Modern Physics*, 89:041004, 12 2017.

[60] Xie Chen, Zheng-Cheng Gu, and Xiao-Gang Wen. Classification of gapped symmetric phases in one-dimensional spin systems. *Physical Review B*, 83:035107, 1 2011.

[61] David T. Stephen, Dong-Sheng Wang, Abhishodh Prakash, Tzu-Chieh Wei, and Robert Raussendorf. Computational power of symmetry-protected topological phases. *Physical Review Letters*, 119:010504, 7 2017.

[62] Marcel den Nijs and Koos Rommelse. Preroughening transitions in crystal surfaces and valence-bond phases in quantum spin chains. *Physical Review B*, 40:4709–4734, 9 1989.

[63] Frank Pollmann, Ari M. Turner, Erez Berg, and Masaki Oshikawa. Entanglement spectrum of a topological phase in one dimension. *Physical Review B*, 81:064439, 2 2010.

[64] Frank Pollmann, Erez Berg, Ari M. Turner, and Masaki Oshikawa. Symmetry protection of topological phases in one-dimensional quantum spin systems. *Physical Review B*, 85:075125, 2 2012.

[65] E. Doucet, F. Reiter, L. Ranzani, and A. Kamal. High fidelity dissipation engineering using parametric interactions. *Physical Review Research*, 2:023370, 6 2020.

[66] Z. Leghtas, U. Vool, S. Shankar, M. Hatridge, S. M. Girvin, M. H. Devoret, and M. Mirrahimi. Stabilizing a bell state of two superconducting qubits by dissipation engineering. *Physical Review A*, 88:023849, 8 2013.

[67] Alexandre Blais, Jay Gambetta, A. Wallraff, D. I. Schuster, S. M. Girvin, M. H. Devoret, and R. J. Schoelkopf. Quantum-information processing with circuit quantum electrodynamics. *Physical Review A*, 75:032329, 3 2007.

[68] Yunzhao Wang, Kyrylo Snizhko, Alessandro Romito, Yuval Gefen, and Kater Murch. Dissipative preparation and stabilization of many-body quantum states in a superconducting qutrit array. 3 2023.

[69] Eyob A. Sete, John M. Martinis, and Alexander N. Korotkov. Quantum theory of a bandpass purcell filter for qubit readout. *Physical Review A*, 92:012325, 7 2015.

[70] A. J. Sirois, M. A. Castellanos-Beltran, M. P. DeFeo, L. Ranzani, F. Lecocq, R. W. Simmonds, J. D. Teufel, and J. Aumentado. Coherent-state storage and retrieval between superconducting cavities using parametric frequency conversion. *Applied Physics Letters*, 106:172603, 4 2015.

[71] Kilian Seibold, Riccardo Rota, and Vincenzo Savona. Dissipative time crystal in an asymmetric nonlinear photonic dimer. *Physical Review A*, 101:033839, 3 2020.

[72] Hossein Taheri, Andrey B. Matsko, Lute Maleki, and Krzysztof Sacha. All-optical dissipative discrete time crystals. *Nature Communications*, 13:848, 2 2022.

[73] Clive Emary and Tobias Brandes. Chaos and the quantum phase transition in the dicke model. *Physical Review E*, 67:066203, 6 2003.

[74] Zongping Gong, Ryusuke Hamazaki, and Masahito Ueda. Discrete time-crystalline order in cavity and circuit qed systems. 8 2017.

[75] Bihui Zhu, Jamir Marino, Norman Y Yao, Mikhail D Lukin, and Eugene A Demler. Dicke time crystals in driven-dissipative quantum many-body systems. *New Journal of Physics*, 21:073028, 7 2019.

[76] Hans KeÃler, Phatthamon Kongkhambut, Christoph Georges, Ludwig Mathey, Jayson G. Cosme, and Andreas Hemmerich. Observation of a dissipative time crystal. *Physical Review Letters*, 127:043602, 7 2021.

[77] K. Baumann, R. Mottl, F. Brennecke, and T. Esslinger. Exploring symmetry breaking at the dicke quantum phase transition. *Physical Review Letters*, 107:140402, 9 2011.

[78] FÃ©lix Beaudoin, Marcus P. da Silva, Zachary Dutton, and Alexandre Blais. First-order sidebands in circuit qed using qubit frequency modulation. *Physical Review A*, 86:022305, 8 2012.

[79] Nicolas Didier, Eyob A. Sete, Marcus P. da Silva, and Chad Rigetti. Analytical modeling of parametrically modulated transmon qubits. *Physical Review A*, 97:022330, 2 2018.

[80] J. D. Strand, Matthew Ware, FÃ©lix Beaudoin, T. A. Ohki, B. R. Johnson, Alexandre Blais, and B. L. T. Plourde. First-order sideband transitions with flux-driven asymmetric transmon qubits. *Physical Review B*, 87:220505, 6 2013.

[81] R. K. Naik, N. Leung, S. Chakram, Peter Groszkowski, Y. Lu, N. Earnest, D. C. McKay, Jens Koch, and D. I. Schuster. Random access quantum information processors using multimode circuit quantum electrodynamics. *Nature Communications*, 8:1904, 12 2017.

[82] S. A. Caldwell, N. Didier, C. A. Ryan, E. A. Sete, A. Hudson, P. Karalekas, R. Manenti, M. P. da Silva, R. Sinclair, E. Acala, N. Alidoust, J. Angeles, A. Bestwick, M. Block, B. Bloom, A. Bradley, C. Bui, L. Capelluto, R. Chilcott, J. Cordova, G. Crossman, M. Curtis, S. Deshpande, T. El Bouayadi, D. Girshovich, S. Hong, K. Kuang, M. Lenihan, T. Manning, A. Marchenkov, J. Marshall, R. Maydra, Y. Mohan, W. OâBrien, C. Osborn, J. Otterbach, A. Papageorge, J.-P. Paquette, M. Pelstring, A. Polloreno, G. Prawiroatmodjo, V. Rawat, M. Reagor, R. Renzas, N. Rubin, D. Russell, M. Rust, D. Scarabelli, M. Scheer, M. Selvanayagam, R. Smith, A. Staley, M. Suska, N. Tezak, D. C. Thompson, T.-W. To, M. Vahidpour, N. Vodrahalli, T. Whyland, K. Yadav, W. Zeng, and C. Rigetti. Parametrically activated entangling gates using transmon qubits. *Physical Review Applied*, 10:034050, 9 2018.